공학박사 학위논문

Microstructural effect on high-temperature oxidation behavior and its related electrochemical properties of heat-resistant alloys

고온 산화 거동과 이와 관련된 전기화학적 물성에
영향을 미치는 내열강의 미세조직 효과

2023 년 2 월

서울대학교 대학원

재료공학부

고 윤 석

Microstructural effect on high-temperature oxidation behavior and its related electrochemical properties of heat-resistant alloys

고온 산화 거동과 이와 관련된 전기화학적 물성에

영향을 미치는 내열강의 미세조직 효과

지도 교수 한 홍 남

이 논문을 공학박사 학위논문으로 제출함
2023년   2월

서울대학교 대학원
재료공학부
고 윤 석

고윤석의 공학박사 학위논문을 인준함
2022년   11월

위 원 장 _____ 이경우 _____ (인)

부위원장 _____ 한홍남 _____ (인)

위   원 _____ 김동익 _____ (인)

위   원 _____ 정인호 _____ (인)

위   원 _____ 허윤욱 _____ (인)

Abstract

Microstructural effect on high-temperature oxidation behavior and its related electrochemical properties of heat-resistant alloys

Ko Yoon Seok

Department of Materials Science and Engineering

Soeul National University

Considering the heat transfer of a Carnot engine, the operating temperature of heat engines has been increased to improve efficiency. This indicates that the heat-resistant alloys are exposed to a higher temperature. Therefore, high-temperature properties like oxidation resistance become more critical in heat-resistant alloys. If the oxidation resistance of alloys is insufficient at a given operation condition, not only the spallation or metal consumption but also the degradation of mechanical properties like creep or fatigue can occur. Also, in non-Carnot-limited fields like SOFC (Solid Oxide Fuel Cell), the electrochemical properties of oxides formed on the heat-resistant alloys have been an essential factor in controlling the electrical performance and the life span of the SOFC stacks.

To control the above properties, we should understand the oxidation behavior of heat-resistant alloys. The oxidation phenomenon is just the

reaction between the alloy and oxidized species. However, the complex composition and the microstructure of heat-resistant alloys and the various operating conditions make us more difficult to understand the oxidation behavior of alloys. The grain size effect on the oxidation behavior, for example, can be applied oppositely depending on the composition of the alloy. Therefore, it is important to determine the critical microstructural effect on the oxidation behavior of heat-resistant alloys.

The author attempted to investigate the two key factors -the alloy grain boundary effect and the alloy/oxide interface effect –independently in each section. In the first part, the effect of the grain boundaries of the alloys was investigated using a microstructure-controlled nickel-based superalloy. The specimens were oxidized at 760 °C in O_2+100 ppm SO_2, and the small-grained specimen showed a lower weight gain after the 100h oxidation test. From the cross-sectional analysis, Cr depletion during the oxidation test was suppressed only in the small-grained specimen because of the highest fraction of alloy grain boundaries. Sufficient Cr diffusion to metal/oxide interface along the alloy grain boundary was available in a small-grained specimen. If the Cr supply to the metal/oxide interface was not enough compared to the growth rate of Cr oxides, the Cr contents at the metal/oxide interface began to decrease. The titanium began to diffuse out to the oxide scale. Ti oxides began to cover the surface of the oxide scale and accelerated the growth rate of Cr oxides. This degraded the oxidation resistance of alloys except for the small-grained specimen.

In the second section, the author focused on the alloy/oxide interface using lanthanum-controlled ferritic stainless steels. The specimens were oxidized at 800 °C in air condition and then the ASR (Area Specific Resistance) of each specimen was measured. The La addition accelerated the oxidation rate, especially the growth of the Cr_2O_3 scale. The severe inward growth of oxides began to occur as the La content of the alloy increased. Interestingly, the electrical performance of oxides formed on the higher La-added

specimens was better despite the thick oxide scale. Various techniques using SEM, TEM, EXAFS, and TKD revealed that not the resistivity of oxide itself but the alloy/oxide interface controlled the electrochemical property of ferritic stainless steels. The La addition promoted the inward oxidation, and the oxide/metal interface began wavier. The tortuous interface acted as the mechanical keying of the oxides, which can improve the adhesion between the alloy and the oxide scale. Therefore, interfacial change due to the La addition can prevent the degradation of ASR property from weak adhesion of the oxide scale.

Table of Contents

List of Tables

List of Figures

Chapter 1. Introduction

1.1. Metallurgical approach for power generation applications

1.1.1 Nickel-based superalloys for thermal power plant

To increase efficiency and reduce the emission of CO_2, many countries (Europe, Japan, China, and India) have tried to increase the operating temperature of power plants above 700 °C [1-5]. These are advanced ultra-supercritical (A-USC) power plants, and the net plant efficiency of A-USC was estimated at more than 42% [6]. Even in the USA, the target temperature of the US Department of Energy and Ohio Coal Development office for A-USC power plants was 760 °C. Therefore, the materials, especially nickel-based superalloys, have been developed for power plants' heater and reheater parts since 2002 [7].

  Another research trend of thermal powerplants is the development of oxy-fuel combustion conditions. The air separation unit (ASU) extracts the N_2 from the air, and nearly pure oxygen is supplied to the boiler system. It can suppress the formation of NOx, which is a cause of fine dust conditions in thermal powerplant. The recycled flue gas (RFG) units, designed to reduce oxygen consumption, circulate the flue gas containing high CO_2 (65~85%) to the boiler system. In the end, the CO_2 processing unit (CPU) captures and stores the CO_2 to reduce the emission of greenhouse gas. The simplified schematic diagram is illustrated in Figure 1.1 [8].
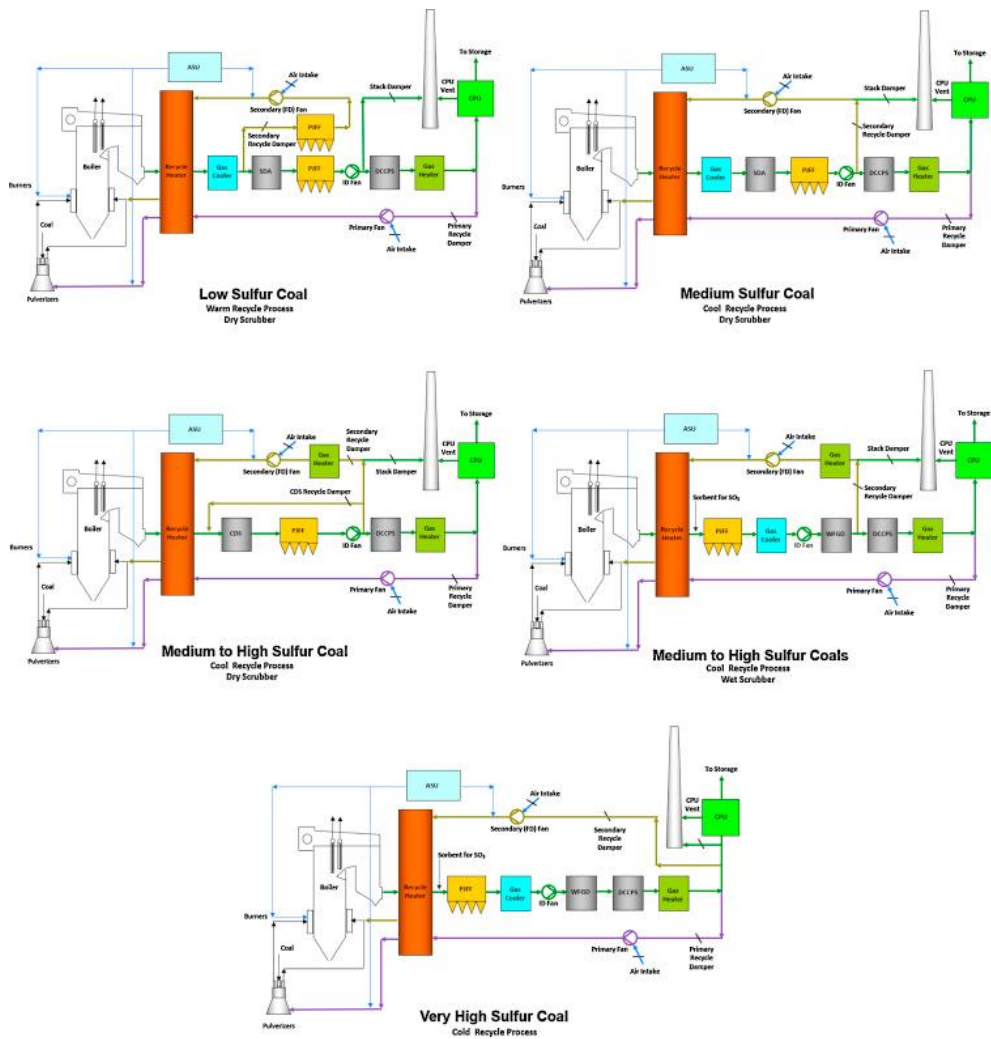
Figure 1.1 Simplified schematic diagram of oxy-fuel combustion system[8]

The higher operating temperature and the higher concentration of oxidants like O_2 or CO_2 in thermal powerplants require heat-resistant steel to have better high-temperature properties.

The creep, the most important mechanical property of a thermal power plant, should be considered at elevated temperatures above 760 °C. It was well known that the creep strength of Nickel-based superalloys was much higher than that of conventional Fe-based alloys. In Figure 1.2 [9], only nickel-based superalloys can achieve the minimum desired strength after 100,000 hours of rupture test. In nickel-based superalloys, Molybdenum and Cobalt were added for the solid solution strengthening, and Aluminum and Titanium were added for precipitation hardening [10]. Especially gamma prime phase hardening is the principal strengthening mechanism of nickel-based superalloys. Many researchers reported that the fraction of the gamma prime phase mainly controls the creep property of nickel-based superalloys [11, 12]. The author focused on the commercial Haynes282 alloy in this study because of its superior creep property.
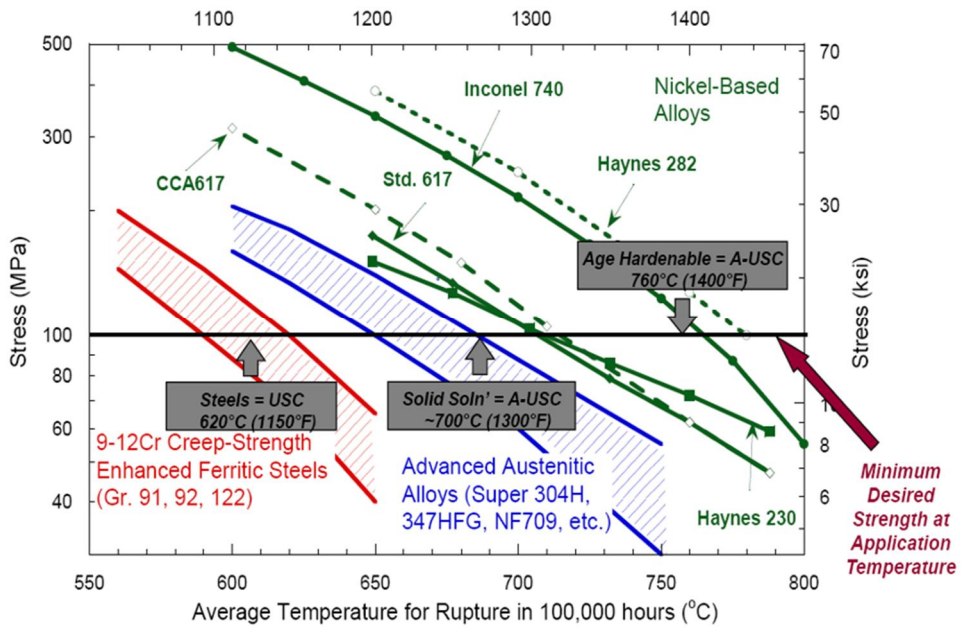
Figure 1.2 Creep properties of heat-resistant alloys [9]

Unlike the mechanical properties, the oxidation behavior of nickel-based superalloys was not much-focused because of their excellent oxidation resistance. However, as mentioned above, the heat-resistant alloys begin to be exposed to more severe oxidation conditions with the development of thermal powerplant systems. Therefore, improving the oxidation resistance has been an important issue for material development.

If the material can not have sufficient oxidation resistance, spallation and metal consumption can be the problems. However, this can also degrade mechanical properties like creep [13] or fatigue [14]. In Figure 1.3, the formation of the gamma prime depletion zone in the oxide/metal interface was illustrated due to the formation of Ti oxides on the surface. The degradation of creep property can be observed in the creep results above in Figure 1.3.

The conventional approach to improving the oxidation resistance of nickel-based superalloys was to control the composition of alloys. Chromium is an important alloying element for oxidation resistance because the stable and slow-growing Cr oxides can protect the alloys even at high temperatures. Therefore, optimum Cr content in nickel-based superalloys was already investigated [15]. However, the complex requirements for high-temperature properties limit the dramatic compositional change of commercial alloys only for oxidation resistance.
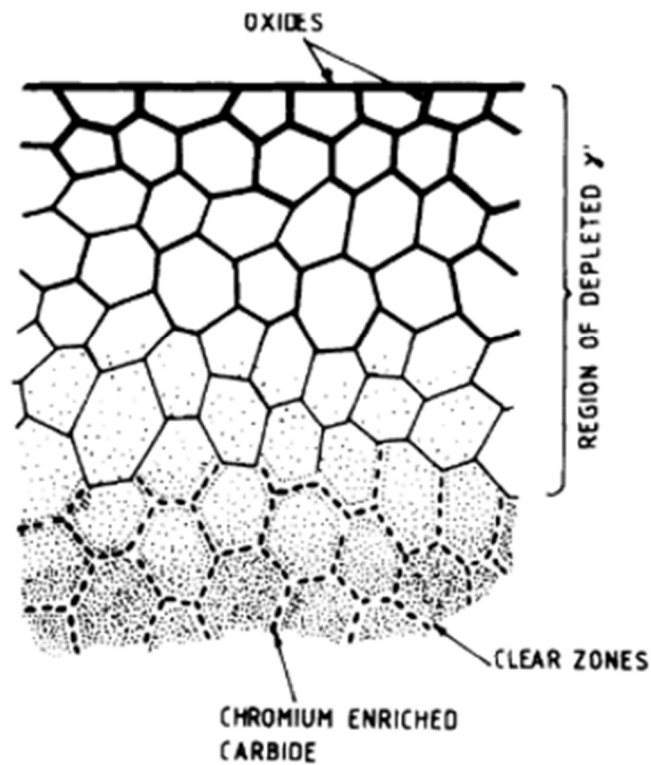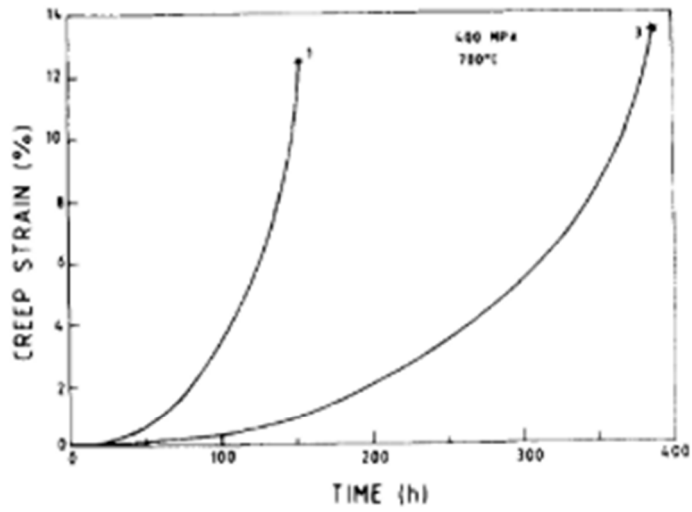
Figure 1.3 Degradation of Creep property due to the formation of gamma prime depletion zone during oxidation [13]

Therefore, the author aims to control the oxidation behavior of nickel-based superalloys by modifying the microstructure. Reducing the grain size can be an alternative concept to control the oxidation behavior of nickel-based superalloys. However, this concept was only investigated in stainless steel [16, 17]. In addition, this study investigated the oxidation behavior of alloys under oxy-fuel combustion conditions. Considering that the oxidation research about Haynes282 was only conducted under air or steam conditions [18, 19], this study seems valuable to demonstrate the microstructure effect and the oxy-combustion effect on the oxidation behavior of Haynes282.

1.1.2 Metallic interconnects for Solid Oxide Fuel Cells

The fuel cell generates electricity via electrochemical processes using fuel gas (hydrogens, carbon monoxide, etc.). Many researchers have developed fuel cell technologies because of their high efficiency and clean by-products. For example, the Solid Oxide Fuel Cell (SOFC) was one of the promising fuel cell types because of its highest efficiency. However, the highest operating temperature in the range of 800~1000 °C has always been a problem for SOFC.

To generate enough electrical power, SOFCs should be stacked, and interconnect materials were required to separate each fuel cell. The ceramics were widely used in the initial SOFCs system because of their superior oxidation resistance and thermal stability. However, the expensive raw materials and the high cost of fabrication was the main problem of stacked SOFCs [20].

Thanks to the successful development of electrolyte materials compared to the traditional yttria-stabilized zirconia (YSZ), the operating temperature of SOFC decreased to below 800 °C [21]. For the last two decades, it has enabled heat-resistant alloys as metallic interconnects [22]. Fe-based stainless steels were one of the promising candidates due to their low material cost, superior formability, the good electrical conductivity of raw materials. Especially ferritic stainless steel is currently considered because of the thermal expansion coefficient (CTE, 11-13 x 10^{-6} K^{-1}) close to the other cell

components $(11.9 \times 10^{-6}K^{-1})$[23].

However, the good electrical conductivity of ferritic stainless steel is not a profit for the metallic interconnects because the oxides such as Cr_2O_3 cover the entire alloy surface during the SOFC operation. Therefore, these oxide layers can act as additional resistance and derive power loss. The power loss due to the oxidation of metallic interconnects was reported to be above 70 % of total SOFC power loss [24]. Therefore, it is important to investigate the oxidation behavior and its related electrochemical properties.

The area-specific resistance typically evaluates the electrochemical properties of metallic interconnects. This property is proportional to the thickness of the oxide scale and the resistivity of each oxide. This indicates that the power loss of metallic interconnects can be reduced by controlling the oxidation behavior of alloys.

A dramatic change in oxidation behavior has been reported in only a small addition of reactive elements (La, Ce, Y, etc.) in ferritic stainless steels [25]. The segregation of reactive elements at grain boundaries is considered to retard the cationic diffusion and promote the anionic diffusion through the oxide scale [25-28], as illustrated in Figure 1.4. Therefore, severe inward oxidation was promoted and can enhance the oxide scale's adhesion.

RE-rich oxide particles

RE ions diffuse
out along scale
grain boundaries

Alloy

RE-rich oxide particles
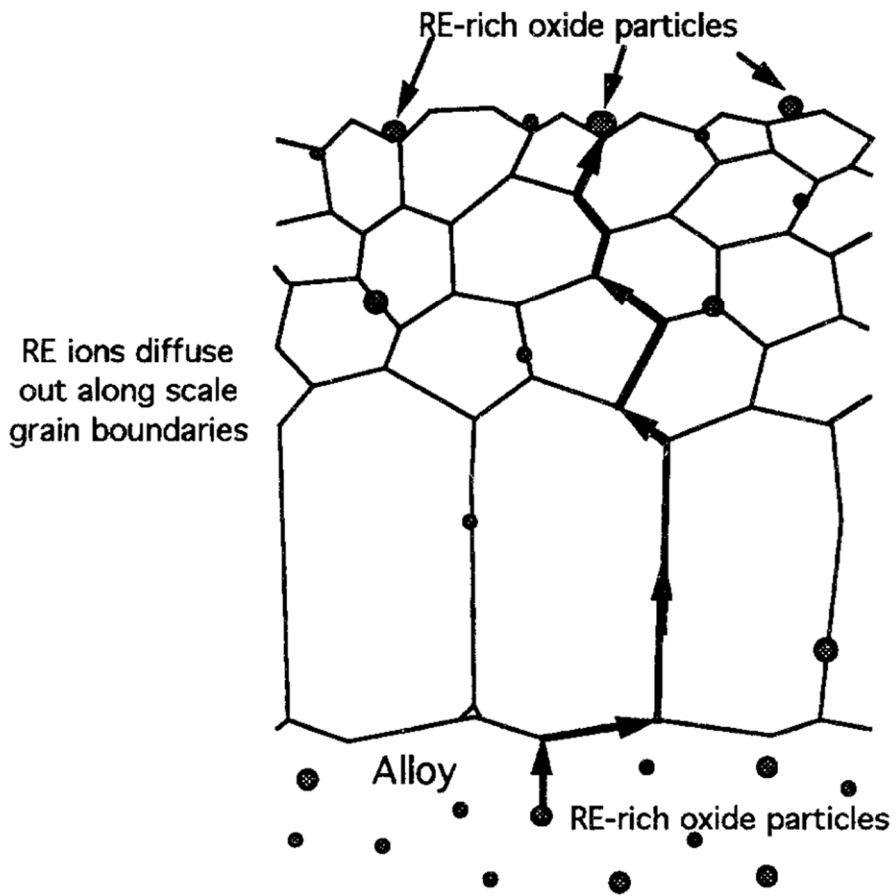
Figure 1.4 Schematic diagram of outward diffusion of reactive element

and the segregation at oxide grain boundaries [28]

The famous commercial alloys such as Crofer 22APU or Crofer 22H also include Lanthanum below 0.1 wt.% to improve the oxidation resistance [29, 30]. Interestingly, the La addition above 0.1 wt.% seems to accelerate the oxidation kinetics of Swaminathan's works [31, 32] but still exhibits a lower area-specific resistance despite the thick oxide scale [33]. To the author's best knowledge, these confronting effects of La addition have not been explained yet. The conventional 'in-situ' measurements can make this difficult because the 'in-situ' results can not give us the direct relation between oxidation kinetics and area-specific resistance. When the metallic interconnects are exposed to high temperatures for a long time, the oxide scale grows, and the area-specific resistance should increase. However, various 'in situ' results exhibit a decrease in the ASR trend, as shown in Figure 1.5[33-36]. The conductive paste (Pt or Au) for the electrical contact between oxides and electrodes is considered to affect the 'in-situ' measurements [37]. Recently, the linear correlation between weight gain and ASR property was achieved using 'ex-situ' measurements [38]. Therefore, this study aims to demonstrate the quantitative relation between oxidation behavior and ASR property of La-added alloys using 'ex-situ' measurements. As stated, the author focuses on changing the metal/oxide interface as the La contents increase.
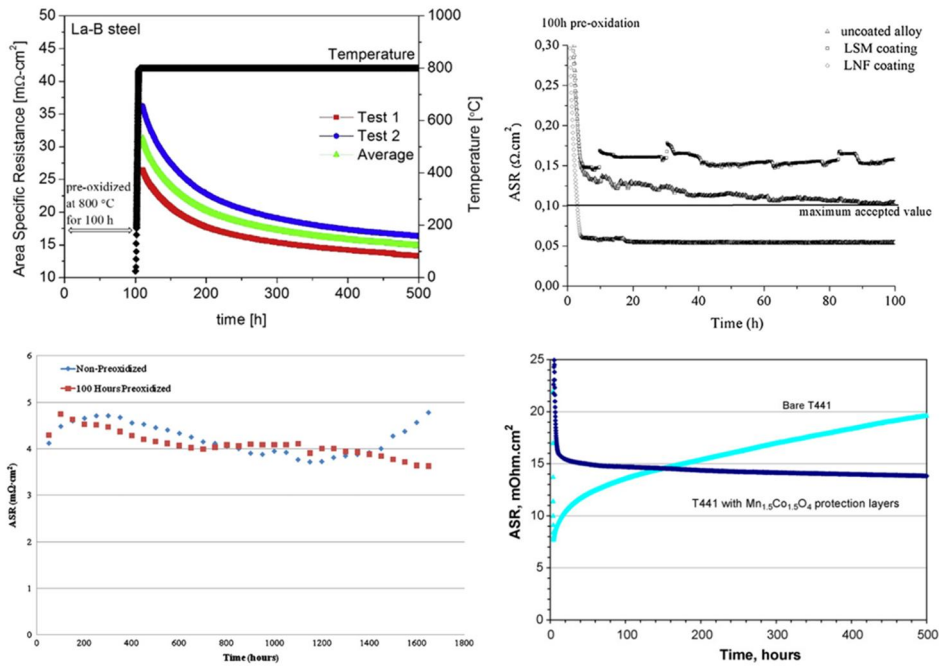
Figure 1.5 ASR decrease trend of 'in-situ' measurements [33-36]

Chapter 2. Theoretical background

2.1. Mechanism of high-temperature oxidation

The oxidation reaction can be simply expressed as shown below

$$\frac{x}{y}M(s) + \frac{1}{2}O_2(g) \rightarrow \frac{1}{y}M_xO_y(s) \quad (2.1)$$
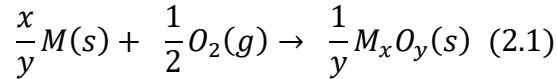
It is the simple reaction between one metal and one oxidant. We can macroscopically estimate the oxidation kinetics by the weight gain values during the oxidation test. Assuming that the weight loss due to the spallation or the volatilization is negligible, the observed weight change, ΔW, corresponds to an oxidation reaction varying with specimen surface area A. Where n_i is the number of moles of the indicated species, and the oxygen atomic weight is set to 16, we can derive equation (2.2) that

$$\frac{-2dn_{O_2}}{A} = \frac{1}{16}\frac{\Delta W}{A} = \frac{ydn_{M_xO_y}}{A} = \frac{-ydn_M}{xA} \quad (2.2)$$

Therefore, considering the molecular weight of oxide (MW_{oxide}) and density of oxide (ρ_{oxide}), we can directly calculate the thickness of the oxide layer from the weight gain result as shown below

$$X = \frac{MW_{oxide}}{16\rho_{oxide}y}\frac{\Delta W}{A} \quad (2.3)$$

Equation 2.3 give us a relatively simple and economical technique to estimate the oxidation kinetics. Only the measurement of simple weight change over time allows us to observe the growth rate of the oxide layer. We can estimate the rate constant of indexed kinetic k_i from the change of growth rates over time. Since the rate constant can be mainly affected by the slowest step of oxygen or metal transfer, we should understand the reactions and transport process of growing oxide scale as illustrated in Figure 2.1.

In detail, we can subdivide the oxidation process into several steps

1) Mass transfer of oxidant from the gas phase to scale-gas interface

2) Absorption and Incorporation of oxygen

3) Transport of metal or oxygen through oxide scale

4) Incorporation of metal into oxide scale

5) Mass transfer of metal from the alloy to the alloy-scale interface

Even in the same oxidation system, gas partial pressure of oxygen (pO_2) or the temperature can strongly affect the dominant step during the oxidation process. This indicates that the various factors involved an oxidation process, including gas-phase mass transfer, solid-state mass transfer, diffusion in the oxide and alloy, and interface reaction.
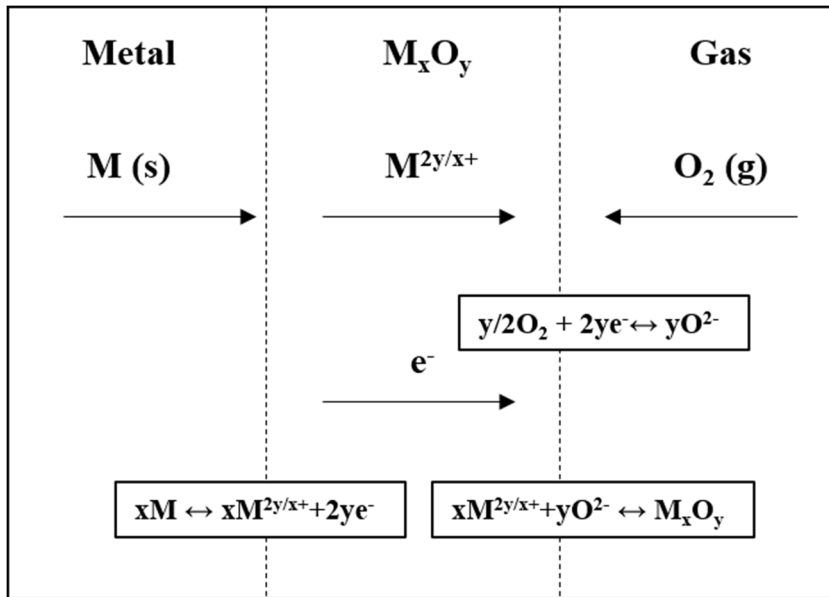
Figure. 2.1 Schematic diagram of several steps for the oxidation process

First, if we assume that the growth rate can be constant during the oxidation test, as shown in equation 2.4

$$\frac{dX}{dt} = k_{linear} \quad (2.4)$$

The k_i indicates the rate constant of indexed kinetic, and the linear oxide growth was observed in this case. In this case, diffusion in the growing oxide scale seems not to contribute to rate control because the thickness of the oxide scale increases over time. It indicates that the diffusion in the oxide scale is very fast or that the oxide scale is too thin to consider the diffusion step. Therefore, this oxidation behavior can be observed at the very initial stage of the oxidation process (very thin oxide scale). The transfer of oxygen step or the absorption of oxygen step should also be considered to understand linear kinetics.

This oxidation kinetics can be observed even in the porous oxide scale. If the pore is large compared to the mean free path of gas molecules, the oxidant can bypass the oxide scale and directly meet the metal surface. The formation of porous oxides on the metal surface is often interpreted as the volume mismatch between metal and alloy. It is stated in terms of the "Pilling-Bedworth ratio."

$$\frac{Voxide}{xVm} < 1 \quad (2.5)$$

Suppose the "Pilling-Bedworth ratio" is smaller than 1, as shown in equation 2.5. In that case, porous oxide can be formed, which can explain the oxidation behavior of Magnesium [39].

In the case of compact scale, second, the growth rate can exhibit parabolic kinetics. The diffusion of species in the oxide scale seems to control the oxidation rate, and the parabolic constant k_p can be derived as

$$\frac{dx}{dt} = \frac{k_p}{X} \quad (2.6)$$

$$X^2 = 2k_p t \quad (2.7)$$

where $X = 0$ at $t = 0$.

$$J = -D\frac{\partial C}{\partial X} \quad (2.8)$$

Fick's first law in equation 2.8 can be applied, assuming that the local equilibrium is established at each interface, as shown in Figure.2.2. This assumption fixed the interface compositions of C1 and C2.

As the thickness of the oxide scale increases, the concentration gradient becomes lower, and we can get parabolic weight gain results. If the rate constant from weight gain results is defined as k_w

$$\left(\frac{\Delta W}{A}\right)^2 = 2k_w t \quad (2.9)$$

We can derive the relation between kp and kw

$$k_p = \left(\frac{Voxide}{16y}\right)^2 k_w \quad (2.10)$$
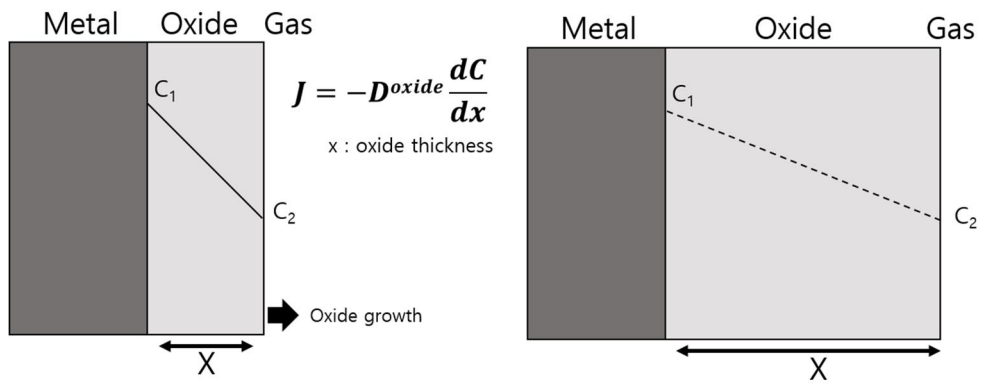
Figure. 2.2 Schematic diagram of mass transport during parabolic

kinetics

The parabolic kinetic is important because this can provide the theoretical basis for understanding the oxidation behavior of heat-resistant alloys. The most famous theory related to parabolic kinetic is the "Wagner theory." Even though the requirements of various ideal assumptions, this theory has been widely applied to interpret the oxidation behavior of heat-resistant alloys.

According to Young [40], the Wagner theory can be applied only in the compact and perfectly adherent scale. As mentioned above, the porous oxide scale can exhibit linear oxidation kinetic. Also, the diffusion of species in the oxide scale is slow enough to control the overall oxidation rate. The local equilibrium at each interface (metal/oxide and oxide/gas) should already be established because of the faster reaction rate at the interface. Furthermore, a relatively low density of grain boundaries and dislocation is required to consider the lattice diffusion of the oxide scale. The last assumption is difficult to apply to the oxidation behavior of heat-resistant steels, and this effect will be dealt with in the next section.

2.2. Microstructure effects

As stated above, Wagner's theory can be applied to the lattice diffusion of the oxide scale. This assumption can be successful in a system containing a large concentration of lattice defects. However, sometimes, the measured oxidation rate can be much higher than the expected oxidation rate. In the actual case, oxide scales consist of several ten-nanometer-sized grains, and a significant fraction of grain boundaries can exist in the oxide scale, as shown in figure2.3. The disordered structure of grain boundaries can decrease the activation energy for diffusion species and accelerate the diffusion kinetics. Another possibility is that the segregation of species to grain boundaries can affect oxidation kinetics. These grain boundary effects can be defined as the effective diffusion coefficient as

$$D_{eff} = D_L(1 - f) + D_{GB}f \quad (2.11)$$

Where f is the fraction of grain boundaries and Di is the self-diffusion coefficient for the indexed sites.
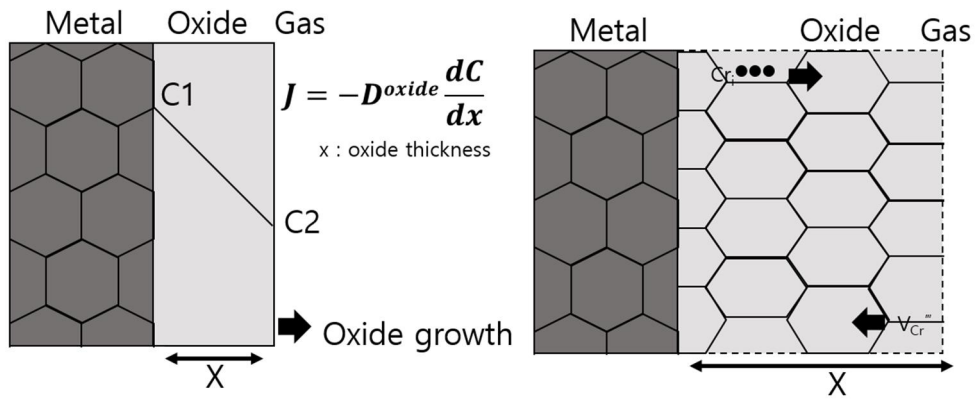
Figure 2.3 Schematic diagram of mass transport involving microstructure

Not only the oxide but also the microstructure of the alloy can affect the oxidation kinetics. Bulk or lattice diffusion can affect the oxidation kinetic, but this effect often is underestimated at intermediate temperatures. Generally, the alloy grain boundaries can be favored as the nucleation site of oxides, and fast alloy diffusion can control the oxidation kinetics. Therefore, selective oxidation of Cr was easily observed in Cr-containing steels. The surface treatment, such as machining, grinding, and shot peening, can also affect the oxidation kinetics because of the high density of dislocations and grain boundaries from surface recrystallized specimens. These subsurface defects can affect the transient stage of oxidation, and the change of the initial microstructure of oxides can control the longer time of oxidation behavior.

Chapter 3. Effect of alloy grain boundary fraction on the oxidation behavior on the oxidation behavior of Nickel-based superalloy

3.1. Material and Method

Sample preparation

The nominal composition of Haynes 282 is listed in Table 3.1. For investigating the microstructure effect, the 20 kg ingot was cut to 300 x 400 x 10 mm, then cold rolled up to 50% reduction and re-cut to 100 x 10 x 7 mm bars for the annealing process. The annealing was conducted at different temperatures of 900°C, 1000°C, and 1180°C for 1 hour, and then labeled based on their recrystallization condition, i.e., cold-rolled sample as 'CR,' sample at 900 °C for 1 hour as 'RX900'; 1000 °C for 1 hour as 'RX1000'; and 1180 °C for 1 hour as 'RX1180'. For measurements, the bar-type samples were recut to dimensions of 10 x 7 x 1 mm. Before the oxidation test, EBSD measurements were conducted, as shown in Fig.31. Specimens were mechanically polished using SiC papers up to 2000 grit. Then they were electropolished at 20V for 28 seconds using the electropolishing machine (LectroPol5, Struers, Denmark). A mixed solution of 100 ml of perchloric acid and 900 ml of Ethanol at -15 °C was used for the electrolyte. The EBSD measurements were conducted by the SEM (Hitachi, S-4300SE, Japan) equipped with an EBSD (e-Flash[HR], Bruker, Germany) detector. The beam condition was 20 kV accelerating voltage, 4 nA probe current, and a 15 mm working distance.
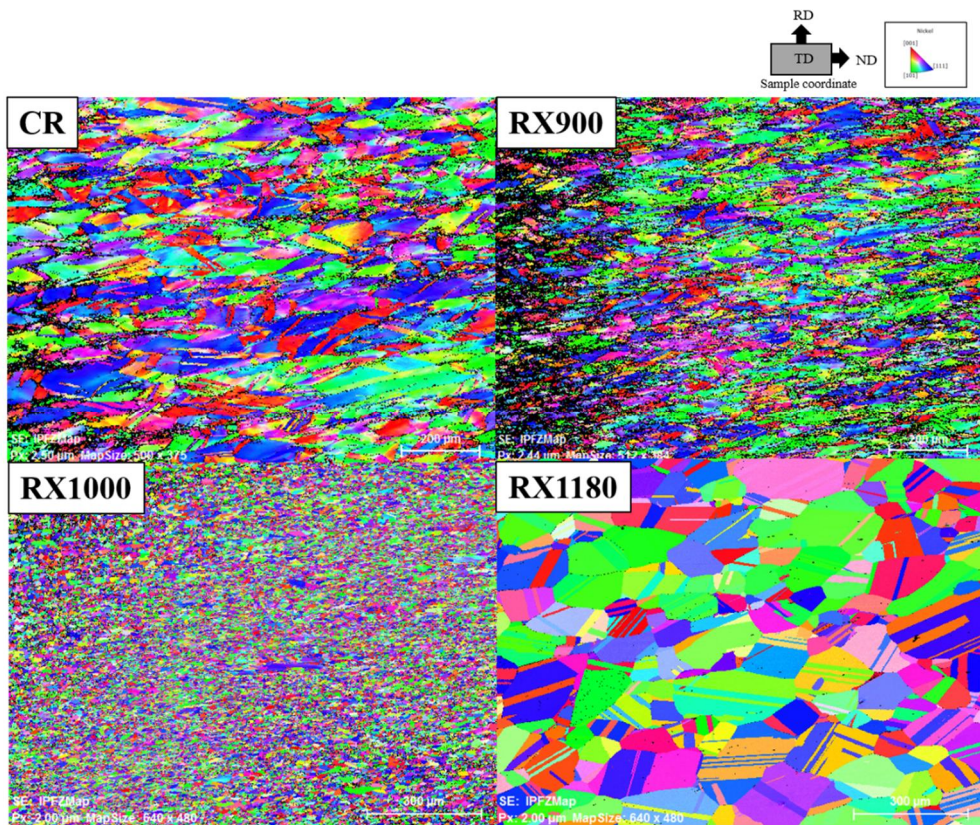
Figure 3.1 Initial microstructure of specimens after annealing process using EBSD analysis (TD plane, x100)

High-temperature oxidation test

All sides of the specimens were mechanically polished using SiC papers up to 2000 grit. The surface area of each specimen was measured using a micrometer. Then the initial weight was measured using a microbalance (MSE3.6P, Sartorius, Germany). The O_2 + 100ppm $SO_{2,a}$ mixed gas condition in 1 atm, was set to interpret the oxy-fuel combustion [41].

The schematic set-up for the experiments is illustrated in Figure 3.2. First, the pre-heated horizontal tube furnace up to 760 ˚C was prepared, and specimens in the alumina boat were inside the tube at the non-heating zone. Before the oxidation test, the tube was flushed with Ar, and then the mixed gas of O_2 + 100ppm SO_2 was introduced into the tube at 50ml/min flow. Next, the Pt catalyst was set in the tube to make an SO_2/SO_3 equilibrium [42].

Finally, specimens were moved to the heating zone and oxidized for 1h, 10h, and 100h, respectively. After the oxidation test, the weight change of specimens was measured using the microbalance. Then these values were divided by the surface area of each specimen to evaluate the oxidation resistance.
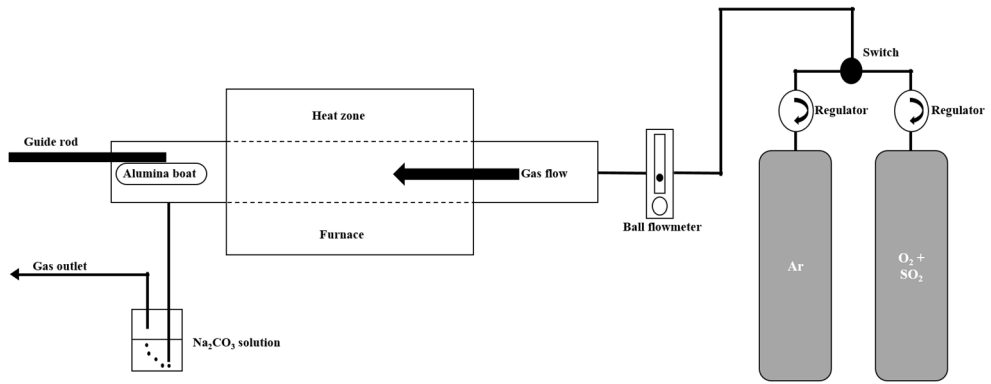
Figure 3.2 Schematic diagram for oxidation test

under the oxy-combustion condition

In addition, the same set of specimens was prepared with the same process and oxidized in a typical box furnace under air conditions. The oxygen partial pressure (pO_2) of the previous oxy-fuel condition was almost 1 bar, and the pO2 of air was almost 2br. Therefore, we can determine the effect of the increase of the oxygen partial pressure. During the oxidation test, the box furnace temperature was maintained at 760˚C ± 2˚C using a K-type thermocouple, and samples in the alumina boat were inserted into the box furnace. For comparison, the specimens in the air condition were oxidized for up to 500 hours.

Oxides characterization

XRD analysis

XRD analysis (D8 advance, Bruker, Germany) with Cu target ($\lambda = 0.154$ nm) was conducted to characterize the oxides formed on the surface. The 2θ angular range was set from 15 ° to 80 ° with a step size of 0.02 °. The scan rate of 2 seconds per point, the sample loading stage was rotated to 30 rpm, and the slit size was maintained at 1 mm. The phase analysis was performed using X'Pert High Score Plus software (PANalytical, Nederland) with the JCPDS database was used for the phase analysis. These obtained results were cross-checked with TEM results.

Morphological & compositional analysis on the surface

SEM equipped with the EDS detector (XFlASH, Bruker, Germany) was used for surface analysis of oxidized specimens. SEM images with various magnifications (x100~x7000) were used to perform the morphological and composition analysis. The beam condition was set to a 20 kV accelerating voltage, a 4 nA probe current, and a 15 mm working distance. EDS results were analyzed by the Esprit software (version 1.9.4), and we can get quantified compositional mapping data (Q-map).

Oxide layer analysis from the cross-section result

The conventional EBSD technique was specialized to get the crystallographic information of the materials. However, because of the small grain size of oxides (~100 nm), the resolution limit has been a problem to be applied in the oxidation study. Fortunately, the Transmission Kikuchi Diffraction (TKD) technique with better resolution than EBSD was developed, enabling us to conduct precise cross-section analysis.

Tem lamellar was prepared from the lift-out method using a Focused ion beam (Nova 600 NanoLab, FEI, USA) system. It was thinned to below 100 nm thickness for the transmitted signals.

The SEM equipped with on-axis TKD (OPTIMUS™ TKD, Bruker, Germany) detector was used, and the beam condition was set to 30 kV to get the transmitted signal. Grain structure and grain boundaries were analyzed using Esprit software (version 2.1). An additional cross-section analysis was performed using TEM (Talos F-200X, FEI, USA) equipped with super EDS.

3.2. Results

3.2.1 Microstructure analysis of alloy

EBSD results of the initial microstructure of the specimens were shown in Figure 3.1 from the transverse direction (TD) side of the specimen. These results can be subdivided into three perspectives: dislocation density, grain size, and grain boundary length.

First, the dislocation density can be affected by the degree of recrystallization. Since these cold-rolled specimens were heat-treated at different temperatures, the degree of recrystallization was also different. In Figure 3.1, equiaxed grains were observed in RX1000 and RX1180, indicating recrystallization [43, 44]. This tendency can be observed using the kernel average misorientation (KAM) map. The KAM value was calculated by the misorientation between a center position of the kernel within the grain and the perimeter of the kernel [45]. It has been reported that the geometrically necessary dislocation (GND) density can be estimated using the KAM value as follows: [46]

$$\rho^{GND} = 2v \ / \ ub \ (3.1)$$

where ρ^{GND} is the GND density, u is the unit length, b is the magnitude of the Burgers vector, and v is the local misorientation. Because the KAM value represents the local misorientation factor (v) [46-48], we can estimate that the higher KAM value indicates a higher dislocation density.

The color code for the KAM value is represented in Figure 3.3. The red color indicates the highest KAM value, and the blue indicates the lowest KAM value. These results show that the KAM values of RX1000 and RX1180 are much lower than those of CR and RX900. This difference is because the recrystallization was almost finished in RX1000 and RX1180, and the deformed regions remained in CR and RX900.
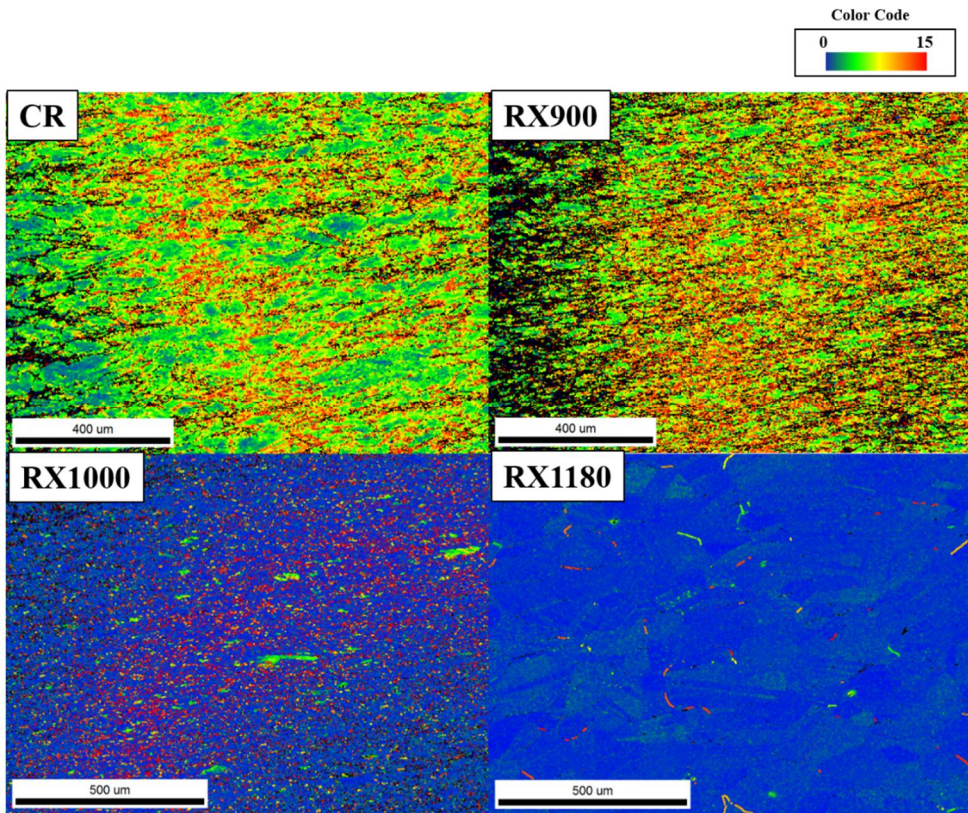
Figure 3.3 KAM result of microstructure-controlled specimens

before oxidation test

Second, the grain size of each specimen exhibits a significant difference. The independent grain was defined as the assembly of pixels that has less than 5° misorientation from adjacent pixels. Since the oxidation behavior was reported as not much affected by twin boundaries [17, 49], these boundary fractions were ignored. The grain size of each specimen before the oxidation test is listed in Table 3.1. RX1000 specimen exhibits the smallest grain size of approximately 14 μm. The grain growth seems to be dominant in RX1180, so the grain size of RX1180 is approximately 10 times larger than that of RX1000

As mentioned above, each specimen exhibited a different grain size and a degree of recrystallization. Therefore, the grain boundary length of each specimen is different, as shown in Figure 3.4. From the EBSD results at the same magnification, the lengths of the high-angle grain boundary (HAGB, above 15°) and low-angle grain boundary (LAGB, below 15°) of each specimen can be calculated. Since the arranged dislocations in grains can be measured as LAGBs, the LAGB length of CR and RX900, which had deformed regions, was much longer than those of RX1000 and RX1180. Because of the different grain sizes, RX1000, which had the smallest grain size, exhibits the longest HAGBs, but RX1180, which had the largest grain size, shows the shortest HAGBs.

Table 3.1 The average grain size of specimens using EBSD measurements

Grain size (um)	CR	RX900	RX1000	RX1180
Haynes282	63.9	38.4	14	183
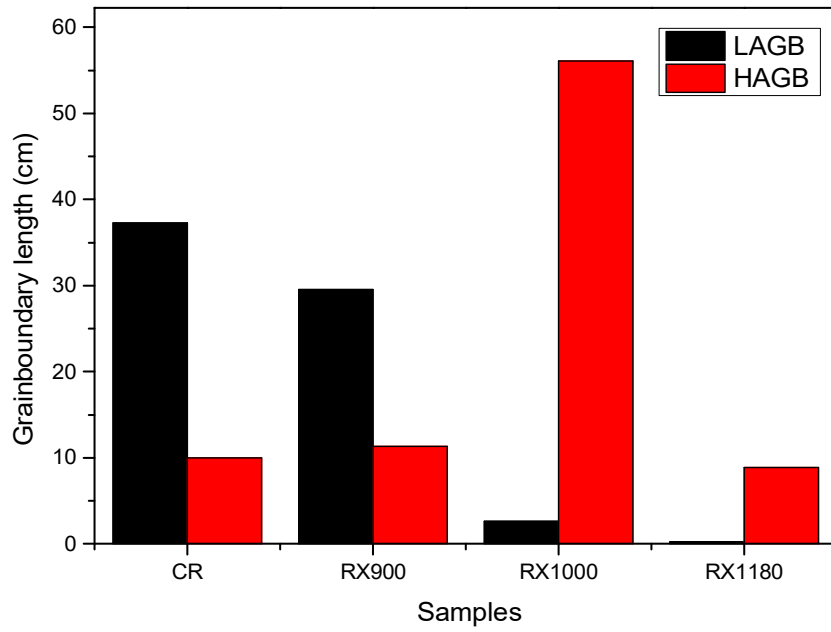
Figure 3.4. The grain boundary fraction of each specimen

3.2.2 Oxidation behavior of the microstructure-controlled alloys

As stated above, the weight gain results enable us to estimate the oxidation rate of specimens. Figure. 3.5 presented the weight gain results under O_2 + 100 ppm SO_2 condition and in air condition. The weight gain value obtained after 500h oxidation in air conditions appears very similar to the 100h oxidation result under oxy-combustion conditions. However, both weight gain curves exhibit parabolic trends, indicating that diffusion of species in the oxide scale mainly affects the oxidation kinetics. It is known that the mass gain curves follow parabolic trends. The parabolic rate constant from weight gain results was obtained below the equation for the quantitative comparison. [50]

$$\left(\frac{\Delta M}{A}\right)^2 = k_w t + c_w \quad (3.2)$$

where ΔM is the weight gain, A is the surface area, t is the oxidation time, and c_w is the integration constant. The calculated parabolic rate constants are listed in Table 3.2. The higher parabolic rate constants under oxy-fuel conditions compared to those from air conditions indicate that oxidation kinetics was accelerated under oxy-fuel conditions.
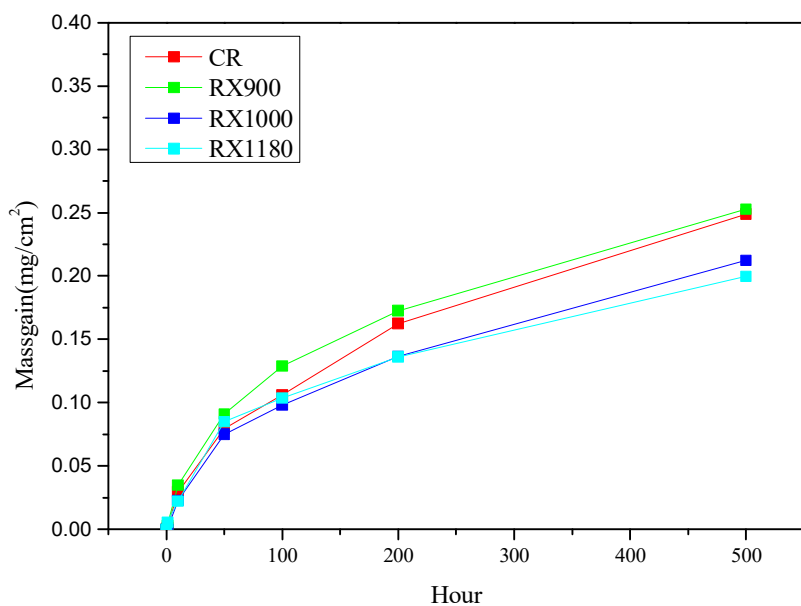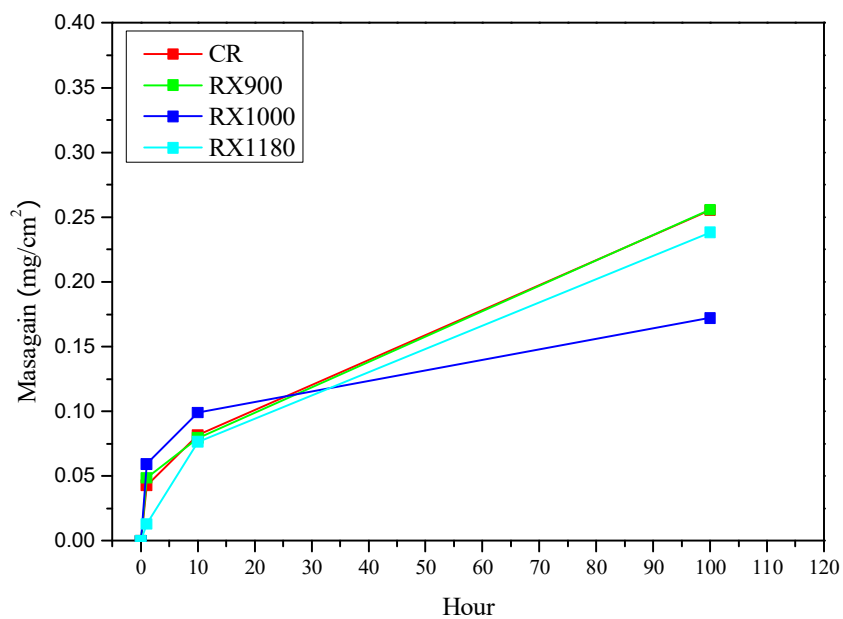
Figure 3.5 Weight gain results under oxy-combustion conditions (upper)

and in air conditions (lower)

Table 3.2 Calculated parabolic rate constants after oxidation test

k_w (mg^2/cm^{4}h)	In O$_2$ + 100ppm SO$_2$ (1h~100h)	In air (1h~500h)
CR	6.46 x 10^{-4}	1.25 x 10^{-4}
RX900	6.48 x 10^{-4}	1.27 x 10^{-4}
RX1000	2.66 x 10^{-4}	8.98 x 10^{-5}
RX1180	5.68 x 10^{-4}	7.85 x 10^{-5}

Interestingly, deformed specimens like CR and RX900 exhibit similar trends under both oxy-fuel and air conditions. These specimens always have higher mass gain values than RX1000 and RX1180. However, RX1000 exhibits the highest weight gain results at the initial stage (1~10h) but shows the lowest weight gain value after 100h under oxy-fuel conditions. Considering that the RX1000 has the smallest grain size among the specimens,   the smaller grain size seems to improve the oxidation resistance under oxy-fuel conditions. The microstructural effect on the oxidation behavior will be handled in this study.

3.2.3 Oxide characterization

Previous studies of the oxidation behavior of Haynes 282 alloys under dry air [19] and steam conditions [18] found that the external scale consisted of Cr_2O_3, nodular type TiO_2 formed on the top surface, and internal Al_2O_3 was formed. Similar oxides were observed in XRD results, as shown in Figure 3.6. The formation of the Cr_2O_3 layer was already observed at 1 h oxidation XRD results, but the TiO_2 oxides began to be detected after XRD results of 100h oxidized specimens. Considering the interaction volume of XRD measurements, the amount of TiO_2 in the early oxidation stage seems insufficient to be detected. However, corresponding SEM and TEM analysis successfully observed the existence of TiO_2 in the early oxidation stage. This finding is reasonable because of the high oxygen affinity of titanium.

Another interesting feature is that the TiO_2 peaks of CR and RX900 were relatively more distinctive than those of RX100 and RX1180. Therefore, the surface analysis was conducted, and the distribution of each oxide on the surface was evaluated.
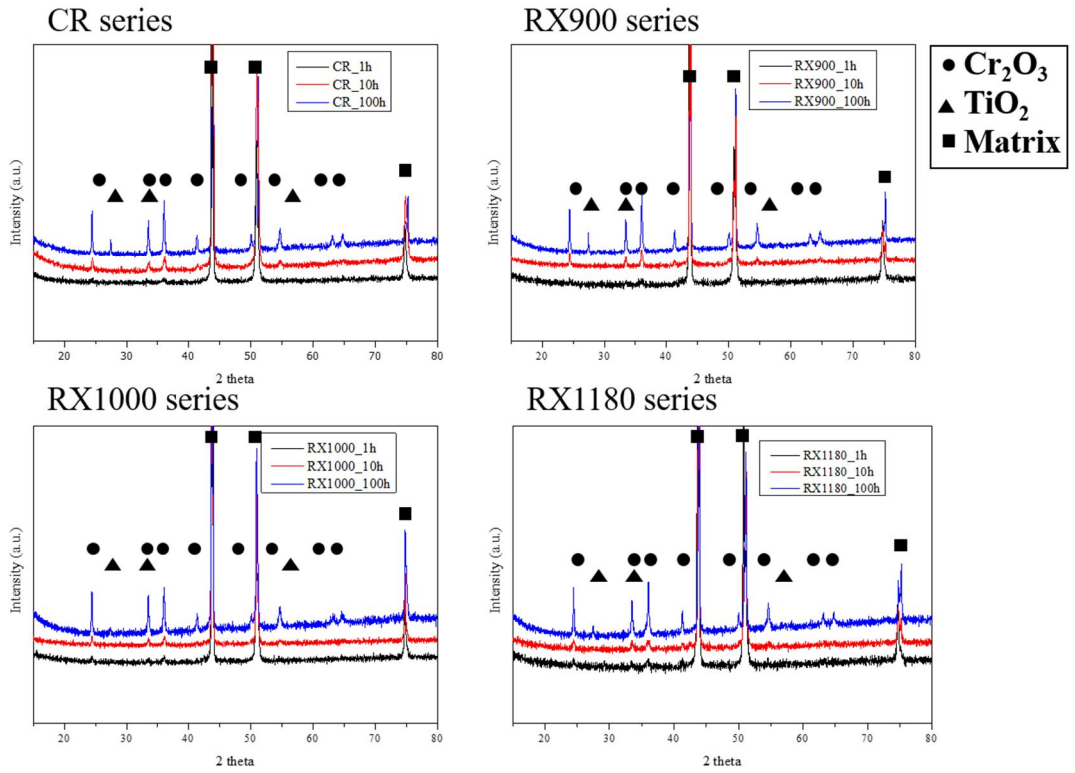
Figure 3.6 XRD results of oxidized specimens under oxy-fuel

conditions for 1h, 10h, and 100h oxidation

SEM and EDS results exhibit inhomogeneous oxidation on the surface of all specimens. The representative three regions are illustrated in Figure 3.7, obtained from the CR specimen after 100h oxidation. The first region consisted of TiO_2 particles, of which the apparent size was approximately a few microns. TiO_2 is thermodynamically more stable than Cr_2O_3, and Ti ions are rapidly diffused to form TiO_2 [40]. This phenomenon was typically observed in Ni-based superalloys [19, 51, 52]. In addition, these TiO_2 particles sometimes agglomerate during oxidation to reduce the interface energy [51].

  The second region consisted of several nodular regions. From the EDS results, only the Cr and O were detected, and no other significant elements were detected, as listed in Table 2. Considering the obvious Cr2O3 peaks from XRD results, it seems reasonable that the second region consisted of Cr_2O_3.
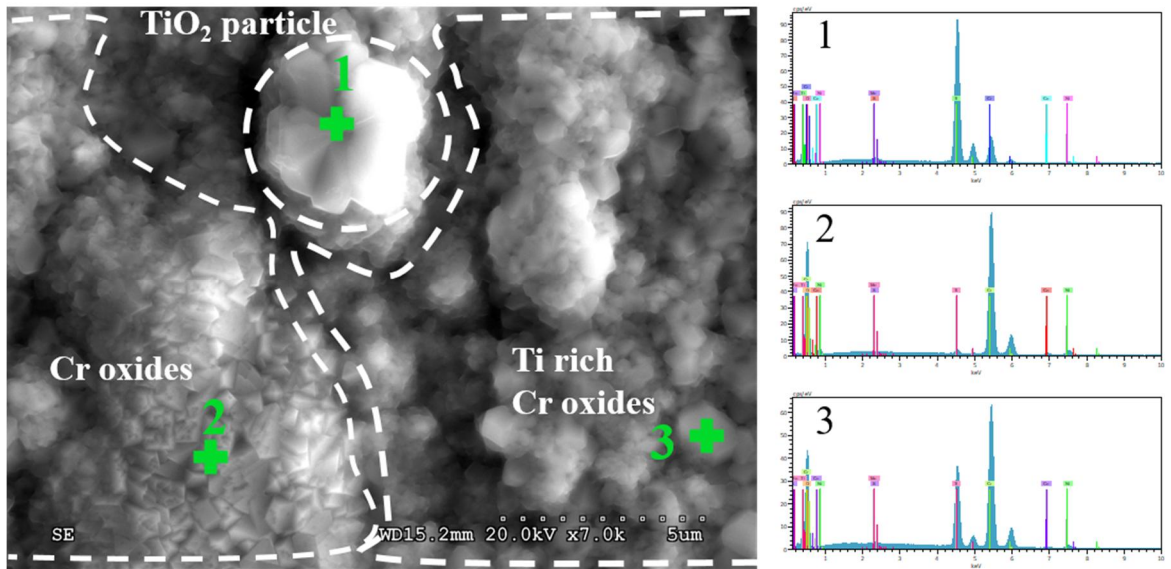
Figure 3.7 Representative SEM image of oxidized surface of CR

specimen after 100h oxidation (left) and EDS spectrum (right)

Table 3.3 Chemical composition table obtained from EDS results of Figure3.7

At.%	O	Cr	Ti	Ni	Co	S	Mo
1	66.13	6.17	26.81	0.48	0.13	0.08	0.21
2	64.1	32.53	0.76	1.87	0.66	0.01	0.08
3	67.81	21.45	9.67	0.72	0.21	0.06	0.08

Interestingly, the third region contained relatively high Ti content (below 10 at.%). For the detailed analysis, Ti-quantified EDS mappings were conducted after 100h oxidized specimens, as shown in Figure 3.8. The range of color code was set to 0~10 at.% to visualize the compositional distribution of Titanium. The red color indicates the highest value of up to 10 at.%, green indicates nearly 5~7 at.%, and blue indicates less than 3 at.%.

As stated above, the region with TiO_2 particles, the first region of Figure 3.7, presents red color. The green regions, which contain a higher Ti content than the blue regions, almost cover the oxidized surface.

However, these green regions are remarkably less in RX1000 than in other specimens. This trend seems independent of the oxidation time, as shown in Figure 3.9. Because of the low amount of Ti at 1h or 10h EDS results, the color range was reset to 0~5 at.%. It seems that surface Ti contents increased as the oxidation time increased.
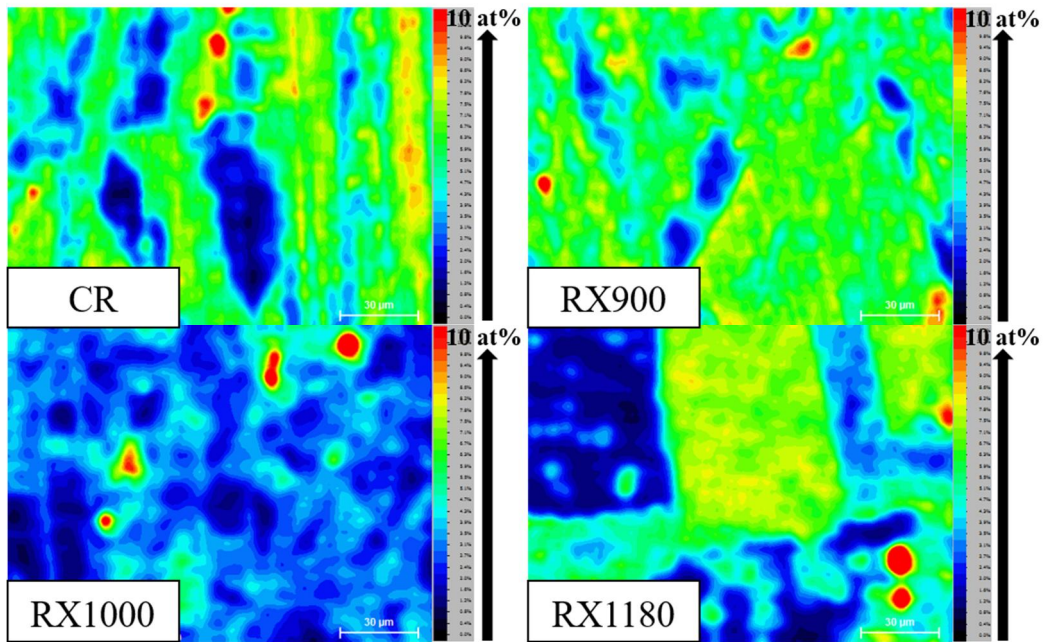
Figure 3.8 Ti quantified EDS mapping results of 100h oxidized

specimens (at.%)
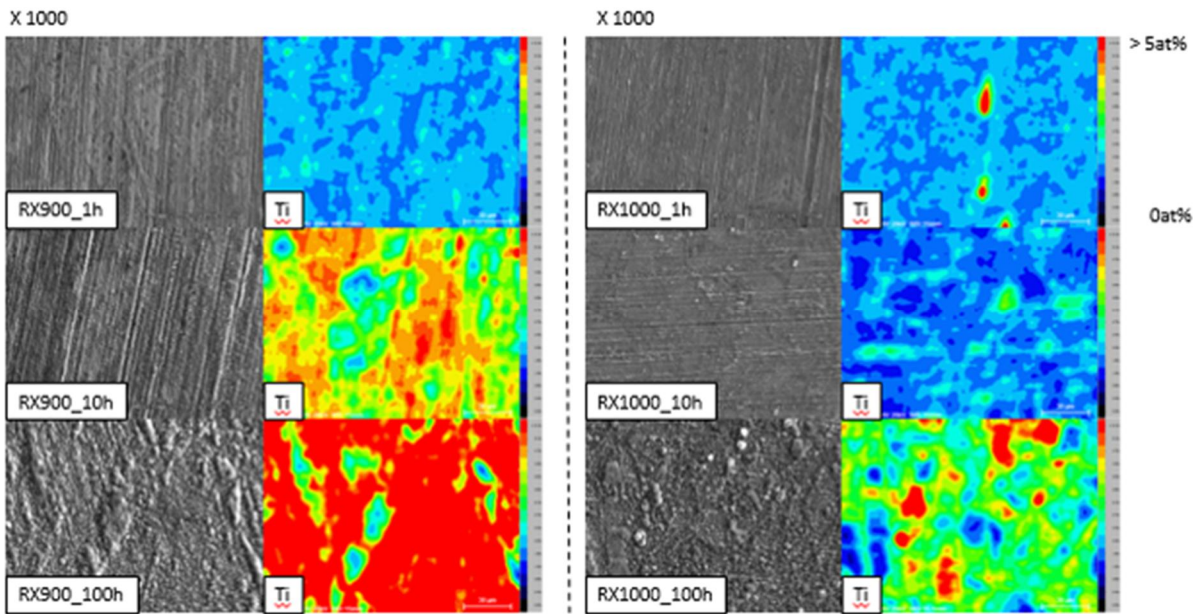
Figure 3.9 Change of Ti Surface concentration over oxidation time

Two TEM lamellar from each Ti-rich region of RX900 and RX1000 were prepared. Cross-section TEM analysis revealed that the several hundred sized TiO2 particles were formed on the Cr_2O_3 scale after 100h oxidation, as shown in Figure 3.10. This result is why the relatively high Ti region was observed on the surface.

In addition, RX1000 exhibits a different trend. The amount of TiO_2 on the surface of RX1000 was much smaller than the others. It indicates that the surface Ti concentration of RX1000 is much lower, as shown in Figures 3.8 and 3.9. Another interesting point is that the thickness of the Cr_2O_3 scale of RX1000 is much thinner than the others. As stated above, RX1000 exhibits the smallest mass gain values after the 100h oxidation test.
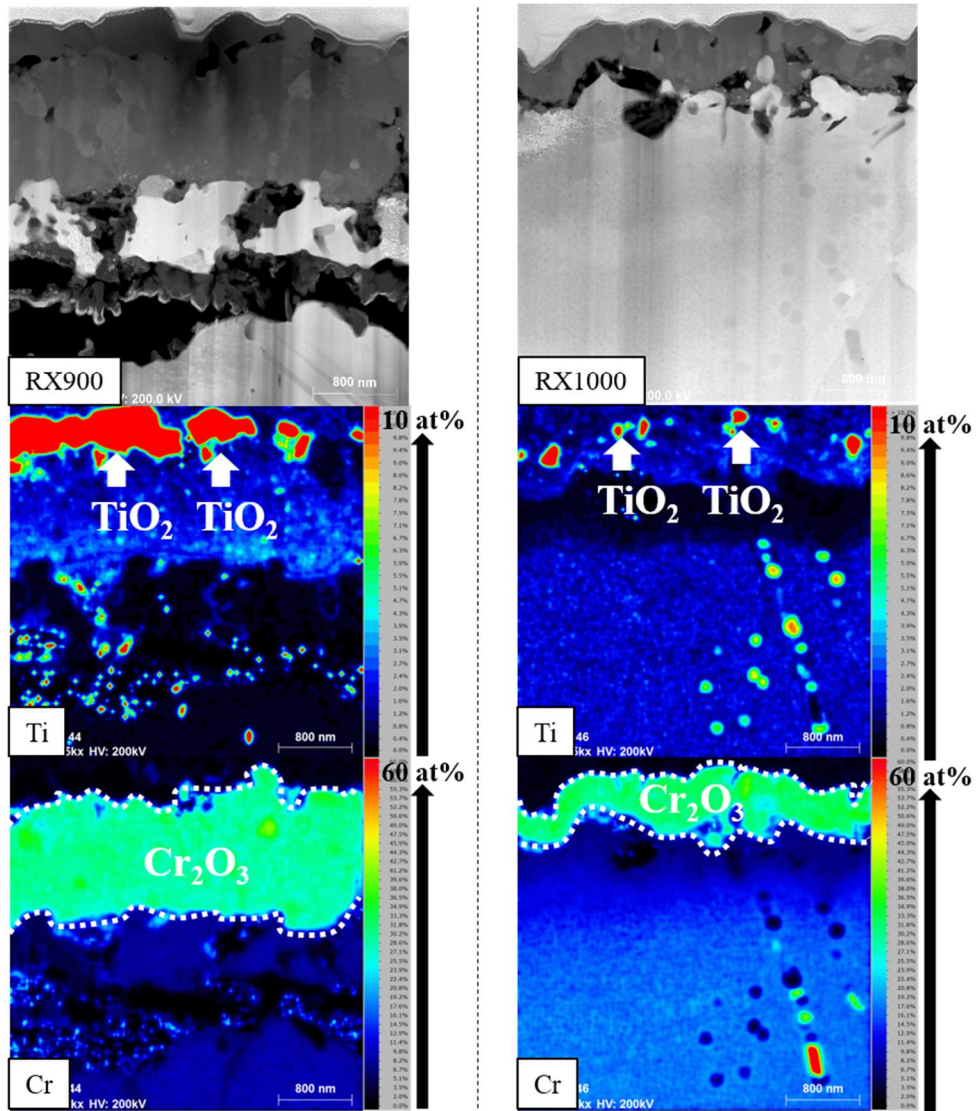
Figure 3.10 Cross-sectional TEM results of RX900 (left)

and RX1000 (right) after 100h oxidation test

3.3. Discussion

3.3.1 Effect of the alloy microstructure on the initial stage of oxidation

Many researchers have studied the effect of grain boundaries on oxidation behavior. High-angle grain boundaries can be the sites for rapidly forming a protective Cr_2O_3 scale in austenite steel. However, the $\Sigma 3$ coincidence site lattice (CSL) boundaries can not affect the oxidation behavior [16, 17]. Similar to the austenite steels, the HAGBs of Inconel 740, Ni-based superalloys, can act as a quick diffusion path for forming the Cr_2O_3 scale [52]. TiO_2 was reported to be found at the grain boundaries of Haynes 282 [19], which is similar to our results. Therefore, it seems reasonable that the fraction of high-angle grain boundaries control the initial oxidation behavior. RX1000, which has the longest HAGBs, exhibits the highest weight gain values in the initial oxidation stage, as shown in Figure 3.11
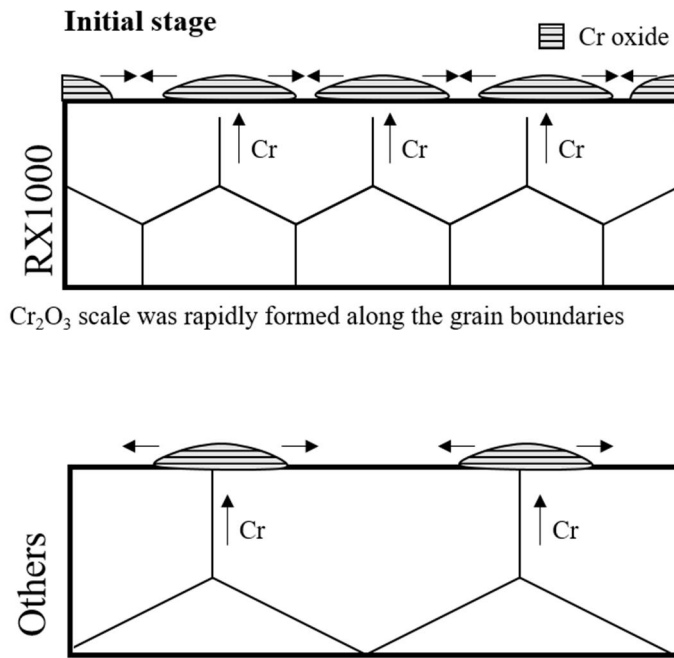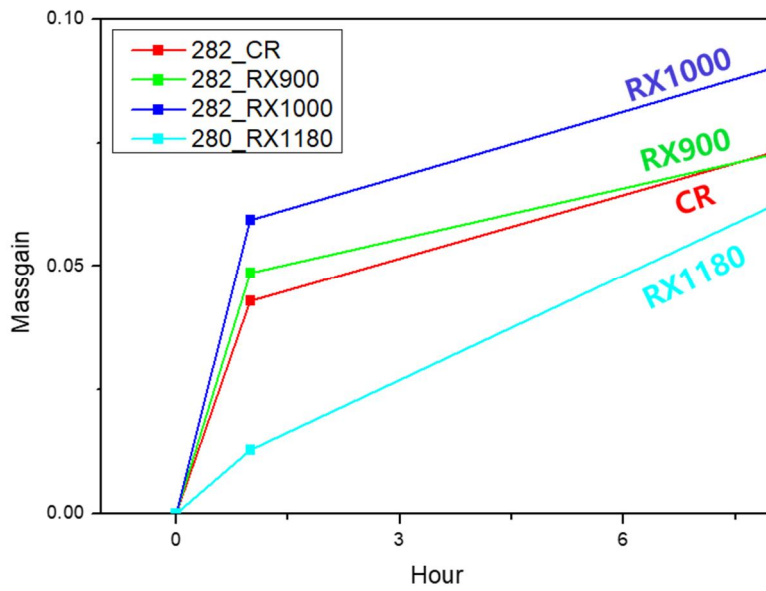
Figure 3.11 schematic diagram of the initial oxidation stage

In addition, the effect of deformed structures was also dealt with in this section. In the case of ferritic or austenitic stainless steel, surface treatment or deformed structure can promote the formation of a thin, protective Cr_2O_3 layer [53-58] and improve oxidation resistance. However, this case can only be applied when abundant dislocations act as short-circuit diffusion paths to form the Cr_2O_3 instead of forming non-protective Fe-rich oxides.

Therefore, this tendency was not observed in the case of high-chromium (~20 wt.%)-high-nickel (~30 wt.%) steels [59, 60] or nickel-based superalloys [61]. The deformed structure only accelerates the growth of the Cr_2O_3 scale, so an increase in weight gain was observed in those results. The oxidation behavior of Haynes282 also exhibits a similar trend. The remained deformed structure in CR and RX900 seems to increase the bulk diffusivity, and the higher weight grain results were obtained from both specimens compared to the RX1180.

During the oxidation test, grain refinement can be occurred, especially in the case of CR and RX900, because of the remaining deformed structure. Since recrystallization was not observed at 900 °C after 1-hour heat treatment, the much lower oxidation temperature (760 °C) seems insufficient to affect the recrystallization of 'bulk' regions.

However, surface recrystallization can occur because mechanical polishing for sample preparation can induce additional deformation in the 'surface' region. This surface recrystallization seems to be more favorable in the CR and RX900. It indicates that the newly formed grain boundaries after recrystallization can act as additional diffusion paths [54]. Even considering the above factors, the weight gain results after the 100h oxidation test can not be explained, so discussed in the following sections.

3.3.2 Effect of the gas atmosphere

Table 3.2 exhibits that the oxidation rate of oxy-fuel conditions is 3 or 5 times faster than the oxidation rate of air conditions. There are two differences between the two conditions. One difference is the existence of SO_2 gas (100 ppm), and another difference is the oxygen partial pressure (from approximately 0.2 bar to 1 bar).

The addition of SO_2 gas is due to simulating the fireside corrosion of alloys in combustion power plants. In this case, alloys can be exposed to various deposits, including alkali sulfates with an SO_2-containing atmosphere. As a result, the oxidation kinetics can be accelerated by forming fusible tri-sulfates induced by the SO_2/SO_3 atmosphere [42, 62, 63]. Moreover, sulfidation-oxidation promotes the formation of sulfides, which also degrade the oxidation resistance [64, 65].

The gas partial pressure mainly controls the above two reactions, so understanding the mixed gas equilibrium is important.

When O_2, SO_2, SO_3, and S_2 involve the reactions with Pt catalyst, possible reactions are defined as [66]:

$$SO_2 + \frac{1}{2}O_2 \rightarrow SO_3 \quad (3.3)$$

$$SO_2 \rightarrow O_2 + \frac{1}{2}S_2 \quad (3.4)$$

$$SO_3 \rightarrow \frac{1}{2}S_2 + \frac{3}{2}O_2 \quad (3.5)$$
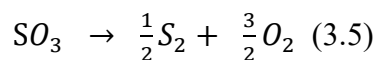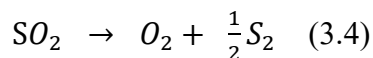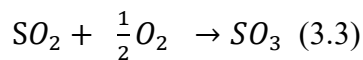
A thermodynamic calculation using the Factsage 7.2 program with the FactPS, FToxid, FTmisc, and FSstel databases estimated the partial equilibrium pressures of gases under oxy-fuel conditions and was listed in Table 3.4. This equilibrium condition was marked as red color in Figure 3.11. Figure 3.11 is the $P(O_2)$ versus $P(S_2)$ diagram, and the thermodynamically stable phases at various partial pressures are listed in Table 3.5. The equilibrium $P(S_2)$ seems to be too low ($\sim 10^{-38}$ atm) to reach $P(S_2)$ for sulfidation or sulfation, and the formation of oxides seems to be more stable than the formation of sulfides or sulfates. Since the XRD, SEM, and TEM results support the absence of sulfides or sulfates, the addition of SO_2 gas did not effectively change oxidation kinetics. From this point of view, the oxy-fuel conditions were regarded as 1atm pure O_2 conditions in the following sections.

Table 3.4 The equilibrium gas partial pressure of oxy-fuel combustion condition calculated by Factsage 7.2

O_2	SO_3	SO_2	S_2
0.9999	5.553×10^{-5}	4.446×10^{-5}	2.201×10^{-38}

Figure 3.11 Thermochemical diagram for Ni - Cr - O₂ - S₂ system at 760 °C. Remarkable phases are selected, and the entire phases are listed in Table 6. The marked point (red) indicates the equilibrium compositions of the mixed gas. The line indicates the possible reaction path with the mixed gas.

Table 3.5 Thermodynamically stable phases at 760 ˚C from Factsage calculations

Number	Phase
(1)	Metal (FCC) + Sulfide (MeS)
(2)	Metal (FCC)
(3)	Cr_2O_3 + Metal (FCC)
(4)	Oxide (Spinel) + Metal (FCC)
(5)	Oxide (Spinel) + Monoxide
(6)	Oxide (Spinel) + $NiSO_4$
(7)	Cr_2O_3 + $NiSO_4$
(8)	$Cr_2(SO_4)_3$ + $NiSO_4$

On the other hand, the increase of oxygen partial pressure seems to accelerate the oxidation kinetics. Schmucker *et al.* [67] found that oxidation rates of a Ni-30Cr alloy at high $P(O_2 \geq 0.1$ atm) were greater than those at intermediate oxygen partial pressures; additionally, Tsai *et al.* [68] reported that oxidation rates were proportional to oxygen partial pressures higher than 0.1 atm.

These tendencies can be estimated using Wager's model, which assumes that the diffusion of ions through the growing oxide scale is the rate-controlling process. However, to make a precise growth rate formula using Wagner's model, it is difficult to reflect slow-growing oxides, such as Cr_2O_3, because of their small stoichiometric deviations. Diffusion via pathways other than the oxide lattice or impurities in the oxides can be the main factor in determining oxidation kinetics [40].

Tsai et al. [69] considered the apparent countercurrent diffusion of oxygen and chromium and found that the dominant factor was apparent chromium diffusion. Therefore, excluding the effect of oxygen diffusion, the parabolic rate constant seems to be proportional to the following:

$$k_w \propto D_{Cr}^o (p_{O_2}^{ext})^{3/16} \quad (3.6)$$

where D_{Cr}^o is the apparent chromium diffusion coefficient at P(O_2 = 1 atm). However, the measured parabolic rate constants are much faster than the estimated values using equation 3.6, as listed in Table 3.6. This result indicates the additional factor affecting the oxidation kinetics, which will be considered in the next sections.

Table 3.6 Comparison between estimated and measured parabolic rate constants

k_p	CR	RX900	RX1000	RX1180
Air (Measured)	1.25×10^{-4}	1.27×10^{-4}	8.98×10^{-5}	7.85×10^{-5}
1atm (Est. from Air)	1.69×10^{-4}	1.72×10^{-4}	1.24×10^{-4}	1.06×10^{-4}
1atm (Measured)	6.46×10^{-4}	6.48×10^{-4}	2.66×10^{-4}	5.68×10^{-4}

3.3.3 Microstructure effect on the formation of the Cr-depleted zone

When oxides are continuously formed on the surface, diffusion through the oxide layer begins to control the oxidation behavior, as illustrated in Figure 3.12. For example, it has already been reported that fine-grained Cr_2O_3 thickens rapidly during oxidation [70] because the apparent chromium diffusion in oxides corresponds to the following:

$$D_{app.} = (1 - f)D_L + fD_{gb} \quad (3.7)$$

where f is the area fraction of the grain boundaries, D_L is the lattice diffusion coefficient in the oxides and D_{gb} is grain boundary diffusion in the oxides. If the average grain size of the oxides is small, the fraction of grain boundaries increases, and the apparent diffusion increases.
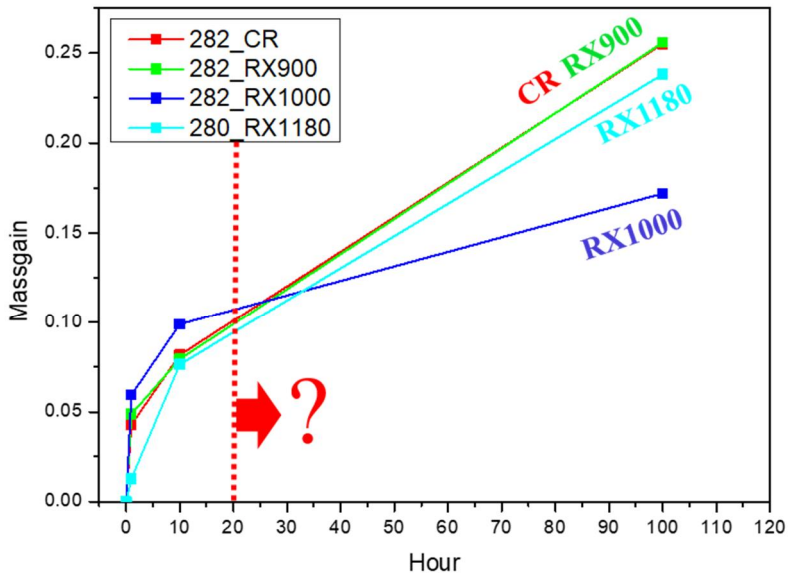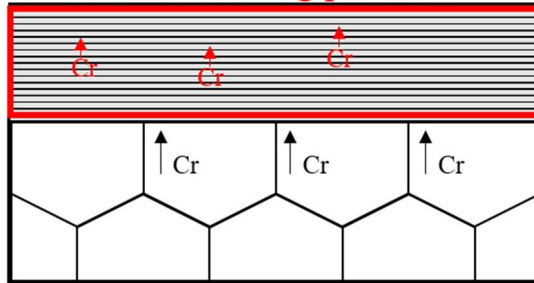
Figure 3.12 Schematic diagram of oxidation process after an initial

stage

For comparison, TKD analysis was conducted on RX900 and RX1000 after oxidation for 10 h. Notably, from the TKD results in Fig. 3.13, the average Cr_2O_3 grain sizes are not significantly different considering the deviations in the measurements. These results indicate that the fraction of oxide grain boundaries is not much affected by the microstructure of the matrix in our experiments. Furthermore, the different early-stage oxidation behaviors of RX1000 under oxy-fuel conditions are not related to the microstructure of the initially formed oxides.

Incidentally, the measured matrix grain size of RX900 is approximately 40 μm, but grains smaller than 1 μm are observed on the surface in the matrix region in Fig. 3.13. Compared to RX1000, grain refinement seems to occur actively on the surface of RX900. It means that near the 'surface' regions, the matrix grain boundary fractions of deformed specimens can be higher than those of recrystallized specimens.
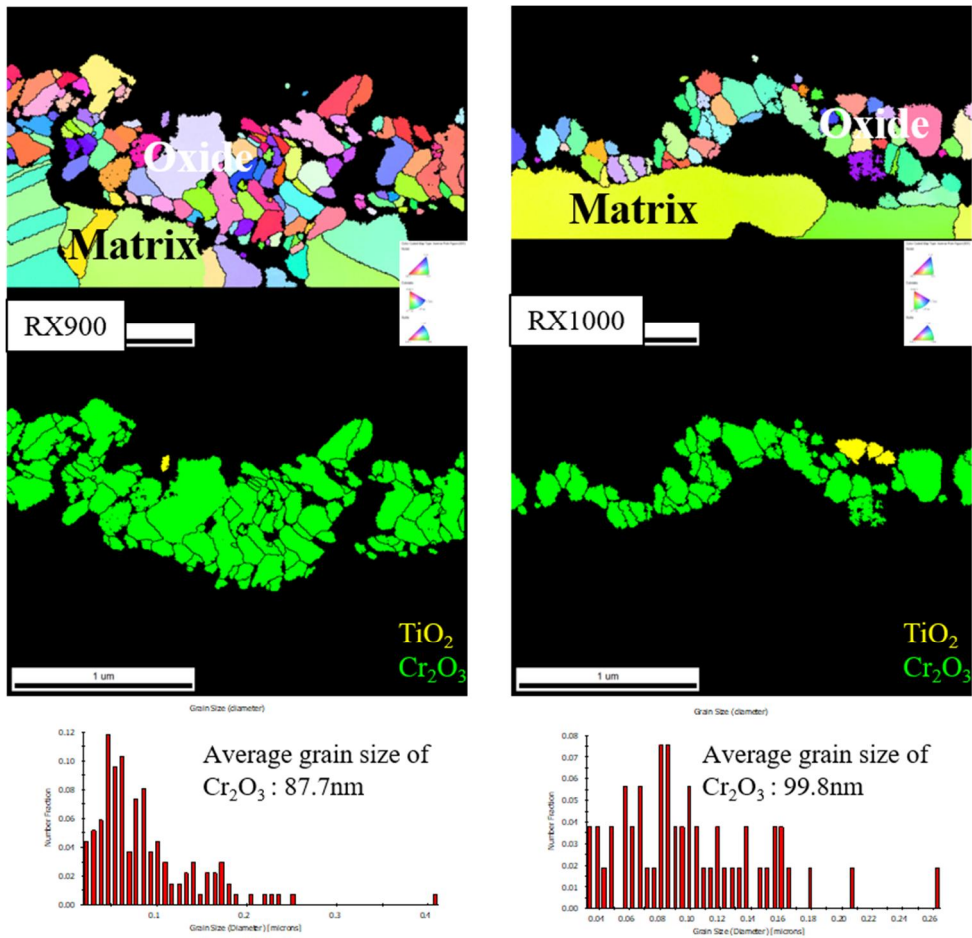
Figure 3.13 TKD results of RX900 (left) and RX1000 (right) after 10h

oxidation. Top: IPF-Z map, Middle: Phase map,

Bottom: Grain size profiles

Due to the Ni-Cr interdiffusion discussed in the previous sections, the selective oxidation of chromium is assumed to explain the oxidation behavior of Haynes 282. This reaction is maintained when the interfacial supply of chromium between the matrix and oxide affords the exclusive growth of chromia. However, the chromium concentration of the matrix near the oxide scale decreases because chromium diffusion leads to oxides forming [71]; thus, a Cr-depleted zone is formed. The EDS map in Fig. 3.14. clearly shows the formation of the Cr-depleted zone. The original chromium content in the matrix is approximately 22 at.%, but the blue regions beneath the oxide scale indicate that the chromium content in this region is only 12 at.%. If the supply of chromium is insufficient because of the Cr-depleted zone, other alloy elements can begin to oxidize instead of chromium, accelerating alloy consumption. In this case, the concentration of Cr in the alloy, N_{Cr}^o, needed to sustain external scale growth can be calculated as follows [72, 73]:

$$(N_{Cr}^o - N_{Cr}^i) = \frac{V_{alloy}}{V_{CrO_{1.5}}}\left(\frac{\pi k_p}{2\widetilde{D}_{Cr}}\right)^{\frac{1}{2}} \text{ (3.8)}$$

where V_{alloy} is the molar volume of the alloy (6.8 cm³/mol) and $V_{CrO_{1.5}}$ is the molar volume of CrO$_{1.5}$ (14.6 cm³/mol) [67]. The parabolic constant, k_p, can be estimated from k_w in Table 3.6, and the interdiffusion coefficient, $\widetilde{D}_{Cr}$, can be deduced as the tracer diffusion coefficient of Cr (5.8 x 10⁻¹⁵ cm²/s) in Ni-22Cr [74].

The Cr flux from the alloy to the alloy-oxide interface approaches the maximum value when the interfacial Cr concentration, N_{Cr}^i, becomes zero. For this reason, the minimum values of N_{Cr}^0 needed to maintain the Cr flux required for oxide growth can be calculated, and an abnormally large value is obtained, as listed in Table 3.7. These results predict that outer chromia growth should be impossible; however, the continuous growth of Cr_2O_3 can be observed in Fig. 3.10.
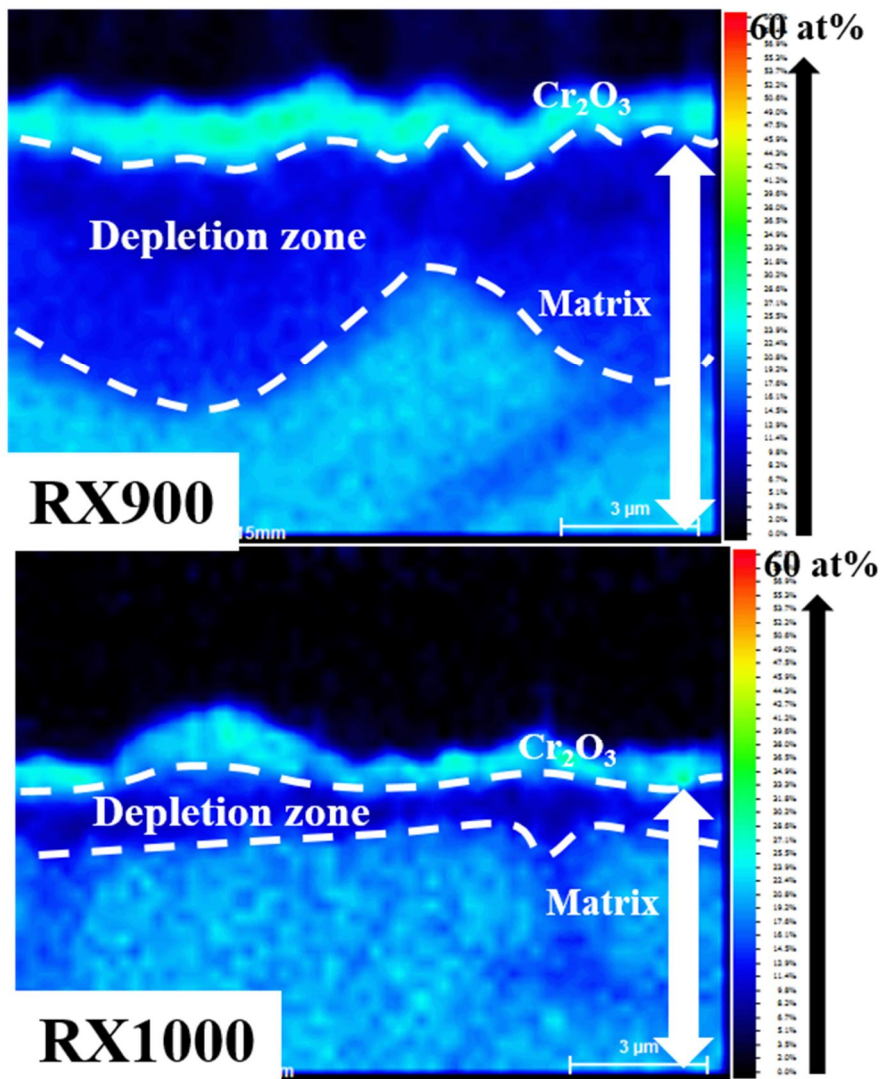
Figure 3.14 Formation of Cr depletion zone after 100h oxidation test

Note that the tracer diffusion coefficients in Ref. [74] were obtained from coarse grains of several hundred micrometers. In this fine-grained microstructure, other diffusion pathways, such as grain boundaries and dislocations, can affect the flux of chromium. Therefore, to identify the microstructural effect, the line profiles of the Cr-depleted zones from EDS mapping results were fitted as follows [72, 75]:

$$\frac{N_{Cr}-N_{Cr}^{alloy}}{N_{Cr}^{i}-N_{Cr}^{alloy}} = 1 - erf\left(\frac{x}{2\sqrt{D_{cal.}t}}\right) \quad (3.9)$$

where x is the distance from the oxide/metal interface, N_{Cr} is the measured Cr mole fraction at x, N_{Cr}^{alloy} is the bulk Cr mole fraction (0.227), N_{Cr}^{i} is the interfacial Cr mole fraction, t is the time of the oxidation test, and $D_{cal.}$ is the calculated diffusion coefficient, which is independent of the Cr concentration. Assuming that the recession rate of the oxide-metal interface on the thin oxide scale is negligible, equation (9) can be derived as the semi-infinite case of Fick's 2nd law. All the fitting results with optimum $D_{cal.}$ in Table 3.7 are well fitted, exhibiting an adjusted R square value exceeding 0.95 (Fig. 3.15).

Table 3.7 Kinetic parameters for simulating alloy diffusion and Cr depletion at 760 °C

	CR	RX900	RX1000	RX1180
k_p (cm^2/s)	6.605 x 10^{-14}	6.626 x 10^{-14}	2.721 x 10^{-14}	5.809 x 10^{-14}
$\widetilde{D}_{Cr}$ (cm^2/s) from Ref .[34	5.8 x 10^{-15}	5.8 x 10^{-15}	5.8 x 10^{-15}	5.8 x 10^{-15}
N_{Cr}^o from $\widetilde{D}_{Cr}$ of Ref. [34]	1.97	1.98	1.27	1.85
$D_{app.}$ from Ref. [58]	6.065 x 10^{-13}	6.831 x 10^{-13}	3.363 x 10^{-12}	5.359 x 10^{-13}
$D_{cal.}$ (cm^2/s) from Eq. (9)	1.988 x 10^{-13}	2.091 x 10^{-13}	3.254 x 10^{-13}	2.194 x 10^{-13}
N_{Cr}^o from $D_{cal.}$	0.34	0.33	0.17	0.30
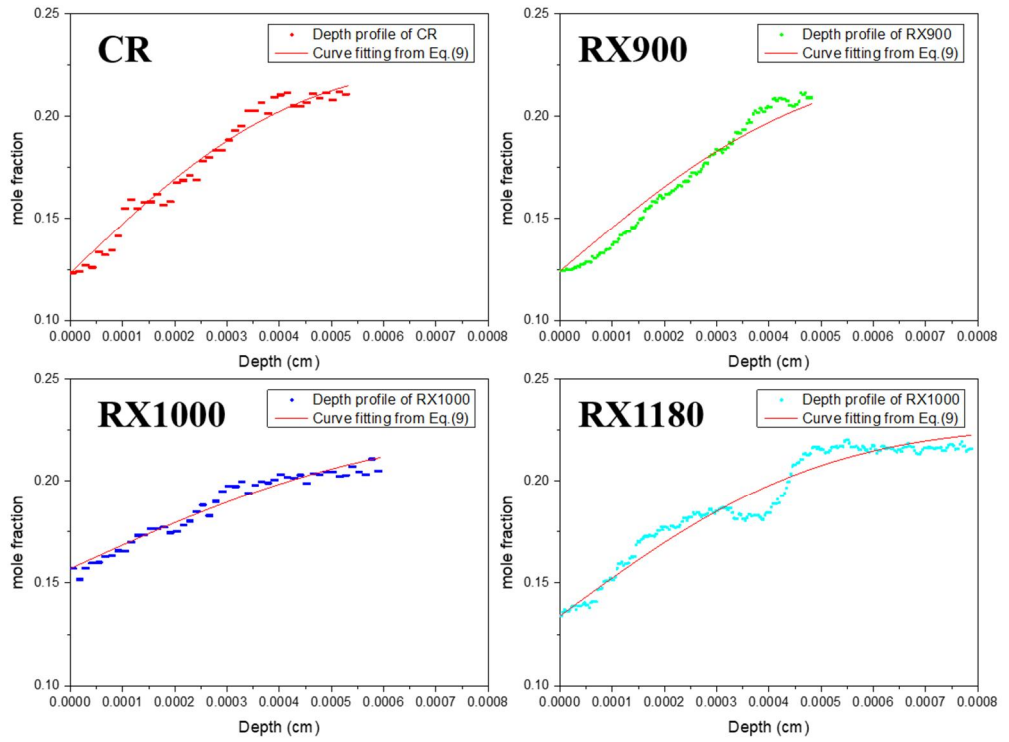
Figure 3.15 EDS depth profiles of Cr at Haynes 282 after 100 h

oxidation test (x=0 indicates the oxide/metal interface)

For comparison, the bulk and grain boundary diffusion coefficients of a Ni-

20Cr alloy [76] were applied in equation (7). The grain boundary width was set to 1 nm, the segregation factor was assumed to be 1 [77], and the EBSD results in Fig. 3 determined the HAGB fractions of each specimen. In Table 7, the $D_{cal.}$ values from equation (9) are of the same magnitude or slightly smaller than the $D_{app.}$ values derived from the diffusion data of the Ni-20Cr alloy. Compared to the alloy system of the Ni-20Cr model alloy, the complex alloy system of Haynes 282 hinders grain boundary diffusion due to the presence of elements such as carbon [78].

Noticeably, the $D_{cal.}$ values of all specimens are 2 orders of magnitude higher than $\widetilde{D}_{Cr}$ from Ref. [56]. It indicates that grain boundary diffusion is an important Cr source for the metal/oxide interface under our experimental conditions. Therefore, RX1000, which has the highest HAGB fraction, shows the highest $D_{cal.}$ value. This result is evidenced by both the Cr EDS mapping and XRD results. In Fig. 3.14, the Cr-depleted zone of RX1000 is much less than that of the other specimens after 100 h of oxidation. A different trend in the XRD peak shifts of RX1000 is observed in Fig.3.16. For other specimens, all the peaks shift to the right after the oxidation test under oxy-fuel conditions; however, no peak shift is observed for RX1000. In the XRD results, the peak positions depend on the lattice parameters, and the lattice parameters of the matrix decrease as the chromium content decreases in the Ni-Cr binary system [79, 80]. From this point of view, the peak shift of the matrix can be attributed to the formation of the Cr-depleted zone on the surface. However,

even though the highest oxidation rate is observed at the initial stage, the matrix peak positions of RX1000 are always similar. This result indicates that the formation of the Cr-depleted zone is slowed only in RX1000 because of the sufficient Cr supply from the high fraction of grain boundaries, as shown in Fig 3.17.
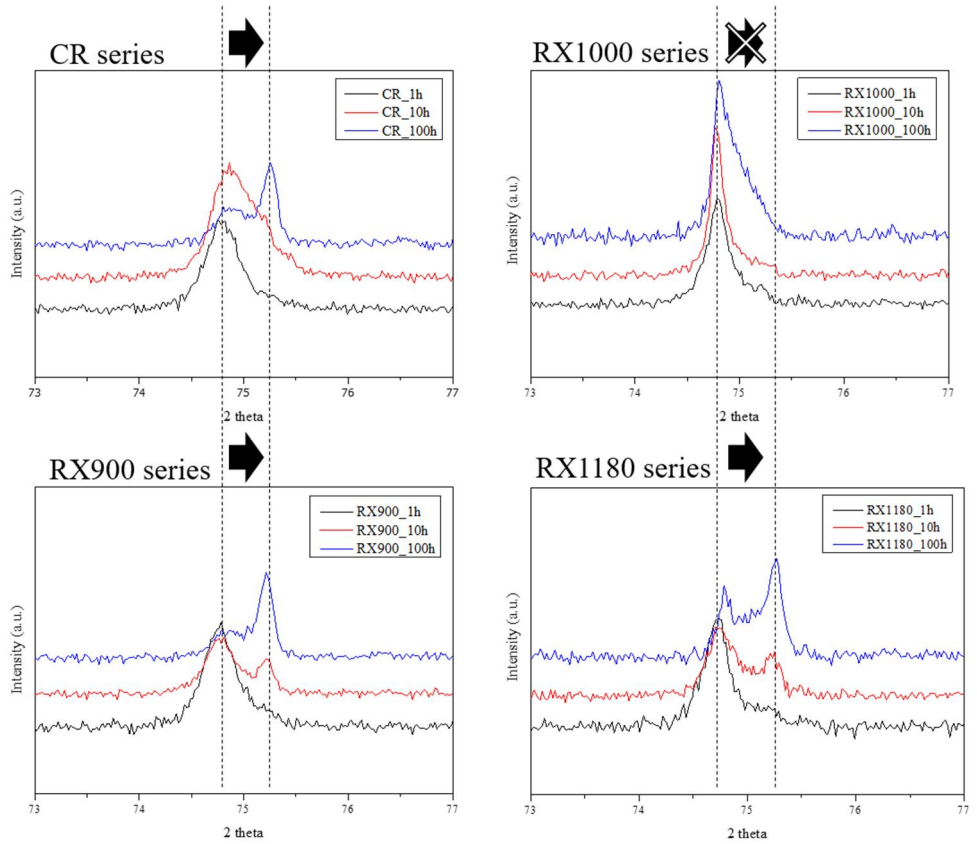
Figure3.16 XRD peak shift according to the oxidation test
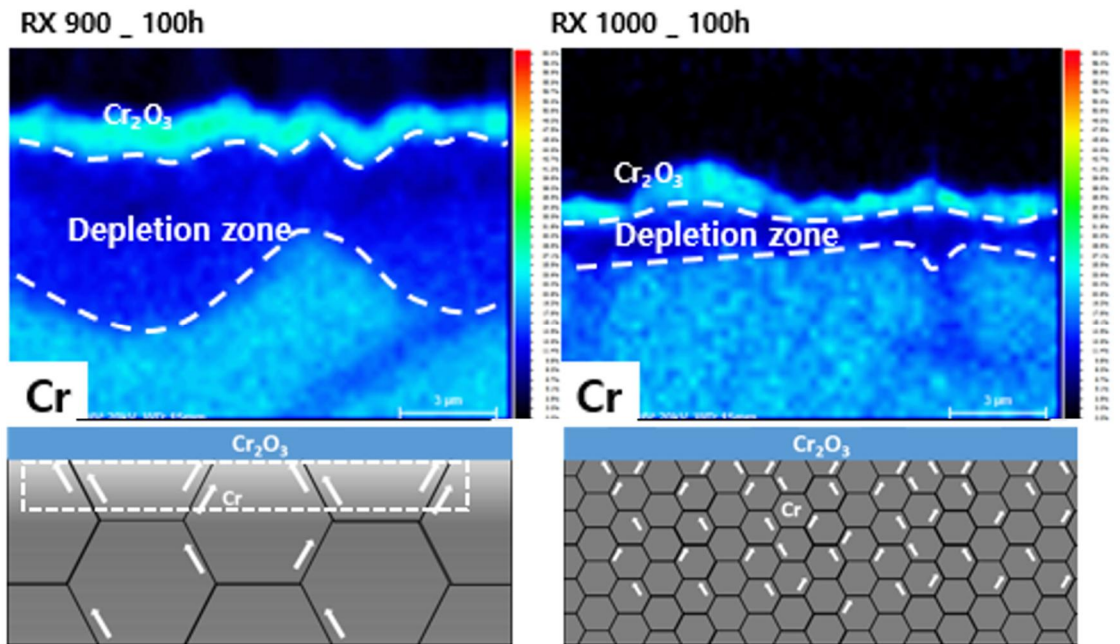
Figure 3.17 Suppression of the formation of Cr depletion zone due to the sufficient Cr supply along alloy grain boundaries

3.3.4 Effect of Ti on the oxidation kinetics

In Table 3.7, except for those of RX1000, the calculated N_{Cr}^0 values of each specimen are higher than the bulk concentration of the specimens (0.227). This observation indicates that the other alloying elements, such as Ti, can be oxidized, as illustrated in Fig. 3.18, and the high Ti content on the surface in Fig. 3.8 and the formation of TiO_2 in Fig. 3.9 support this. Ti diffusion to the oxide scale can change the oxidation kinetics; notably, the detrimental effect of Ti has been reported by various researchers. Nagai *et al.* found that the addition of Ti increased the oxidation rate of a Ni-20Cr alloy [81], and even increasing the TiO_2 fraction on the surface before the oxidation test degraded the oxidation resistance [82]. Kim *et al.* [83] and Angerman [84] insisted that intergranular attack explained the increase in mass gain results, which corresponded to the addition of Ti, and Chen *et al.* [85] suggested that the increase in mass gain results was due to the formation of TiO_2 on the surface. These tendencies match well with the smallest mass gain value of RX1000, which has the lowest Ti content on its surface. However, they cannot explain the different thicknesses of Cr_2O_3 formed on the microstructure-controlled alloys. The enhanced chromia layer growth of a Ti-doped alloy has already been reported [86], and similarly, the Cr_2O_3 layer on RX1000 is two times thinner than that on the other samples (Fig. 3.10).

An X-ray absorption spectroscopy (XAS) study by Blacklocks *et al.*

[87] can help explain this phenomenon. They found evidence from extended X-ray absorption fine structure (EXAFS) results that the dissolved Ti cations in Cr_2O_3 were located in the substitutional sites of Cr cations and found that the charge state of Ti cations was close to Ti^{4+} using X-ray absorption near edge structure (XANES) measurements. Combined with our observation, a possible mode of TiO_2 dissolution in Cr_2O_3 can be expressed as follows:

$$3TiO_2 \rightarrow 3Ti_{Cr}^{\bullet} + V_{Cr}''' + 6O_o^x \quad (3.10)$$
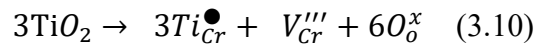
where $Ti_{Cr}^{\bullet}$ represents Ti^{4+} in the Cr^{3+} site and V_{Cr}''' represents the Cr vacancies. Equation (3.10) shows that the supplemental Ti caused by the formation of the Cr-depleted zone increases the vacancy concentrations in the oxide scale and accelerates the oxidation kinetics. Therefore, slowing the formation of the Cr-depleted zone in RX1000 restricts the Ti supply to the oxide scale and consequently suppresses the formation of Cr vacancies, which can increase the growth rate of Cr_2O_3.
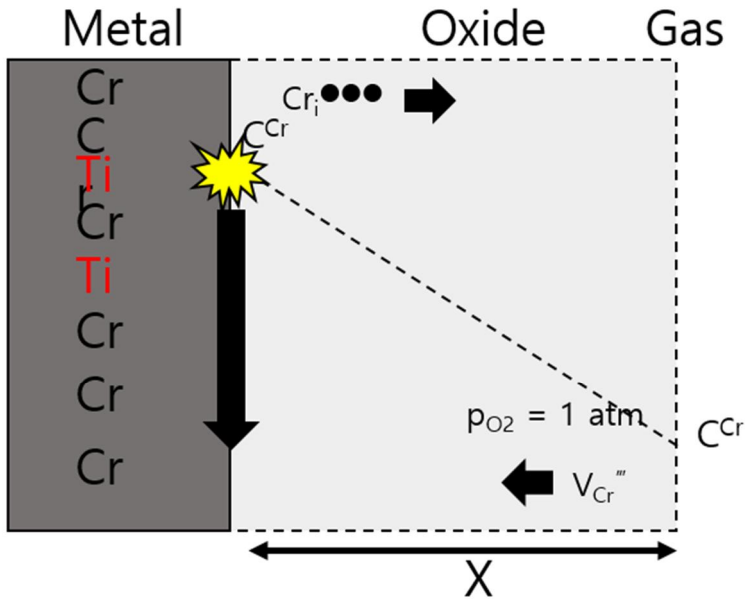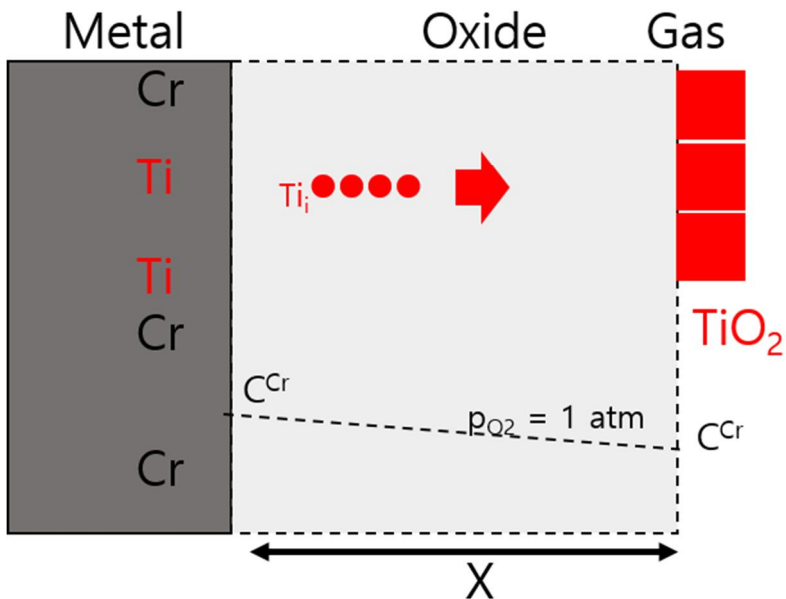
Figure 3.18 Diffusion of Ti to oxide scale after the formation of Cr depletion zone

Chapter 4. Effect of alloy/oxide interface on the Area-specific Resistance behavior of La-added alloys

4.1 Materials and Methods

Sample preparations

Ingots with various amounts of La (100 kg) were prepared from the vacuum induction melting furnace (Hankook Vacuum Metallurgy Co, Korea) and cut to 350 x 350 x 80 mm. The homogenization process was conducted at 1200 ˚C for 12 h and hot-rolled up to 78 % at 1150 ˚C. The dimension of samples from hot-rolled sheets was 10 mm x 10 mm x 2 mm and had the transverse plane on the surface. The specimens were mechanically ground using SiC papers up to 2000 grit. Before the experiments, the X-Ray Fluorescence method (XRF) was used for the composition analysis, and their results are listed in Table 4.1. Alloys with the highest La (0.479 wt %) are named as 'La-H'; 0.086 wt% La as 'La-M.' trace level as 'La-L.' The term 'Trace' indicates that the amount of La is below the XRF detection limit (~0.014 wt%), but 0.006 wt% La was detected in the previous ICP result [31].

The microstructure of the alloys before the oxidation test was carefully investigated using SEM (S-4300SE, Hitachi, Japan) equipped with an EDS detector (XFlASH, Bruker, Germany) and EBSD detector (e-Flash[HR], Bruker, Germany). Also, the depth profile of SIMS (TOFSIMS.5, ION-TOF, Germany) measurements were conducted to define dissolved La in La-added alloys. The Cs+ ion beam with 10 keV was used for the sputtering, and a high beam current sputtered the raster area of 150 μm x 150 μm. In addition, TEM analysis (Talos F-200X, FEI, USA) was also performed with an EDS system (Super-X[TM], Bruker, Germany).

Table 4.1 Chemical composition of La-added alloys (in wt.%)

wt.%	La-L	La-M	La-H
Fe	Bal.	Bal.	Bal.
Cr	23.9	23.9	23.8
Al	0.017	0.047	0.060
Mn	0.284	0.293	0.295
Ti	0.075	0.091	0.078
C	0.88	0.869	0.849
Ni	0.508	0.513	0.479
Si	0.021	0.016	0.015
La	Trace	0.086	0.479

Evaluation of the electrical performance of La-added alloys

As stated above, ASR measurements were conducted by the ex-situ method to find a direct relation between oxidation behavior and electrical performance, as shown in Figure 4.1 [38]. First, the specimens were isothermally pre-oxidized at 800 ˚C for different hours of 100, 200, 300, 400, and 500 h in the box furnace. Then, Pt paste was applied for a better electrical connection between the oxidized surface and Pt mesh. Next, two sets of Pt mesh were placed on the top and bottom of the specimen and connected with the source-measure unit (GS610, Yokogawa, Japan). Ceramic weights (380 g) were used for the constant load. Finally, the four-probe DC technique was used to evaluate the electrical resistance, as shown in Figure 4.2.
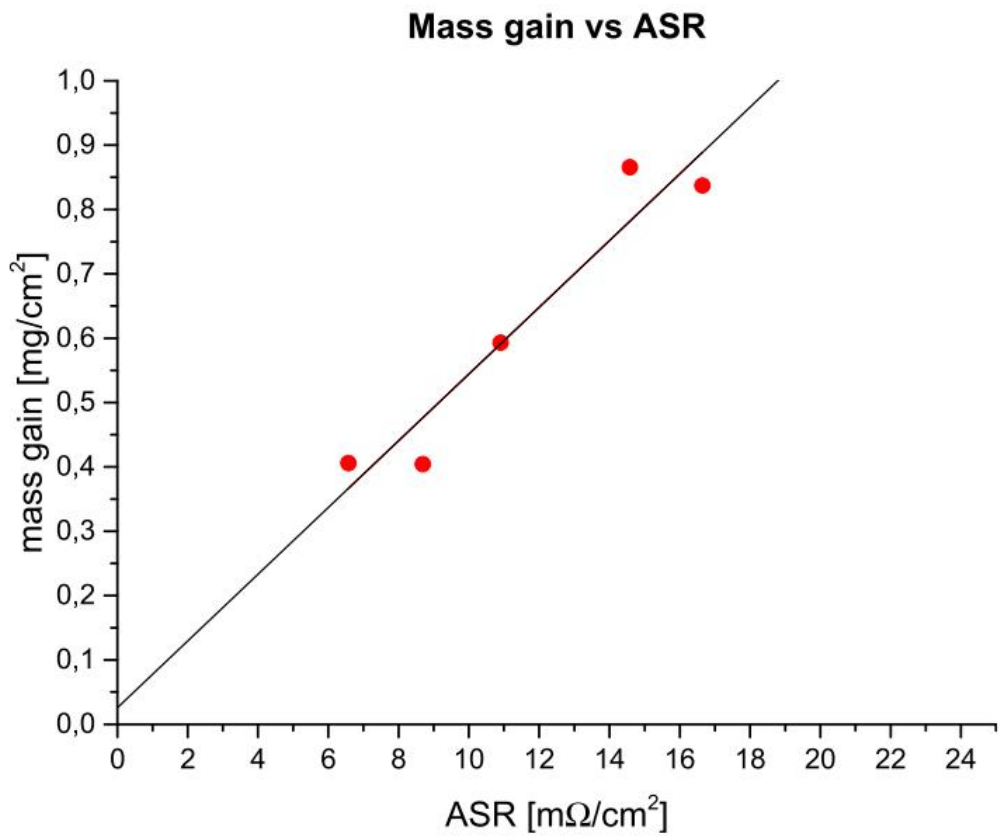
Figure 4.1 Linear relation between ex-situ results and mass gain

results
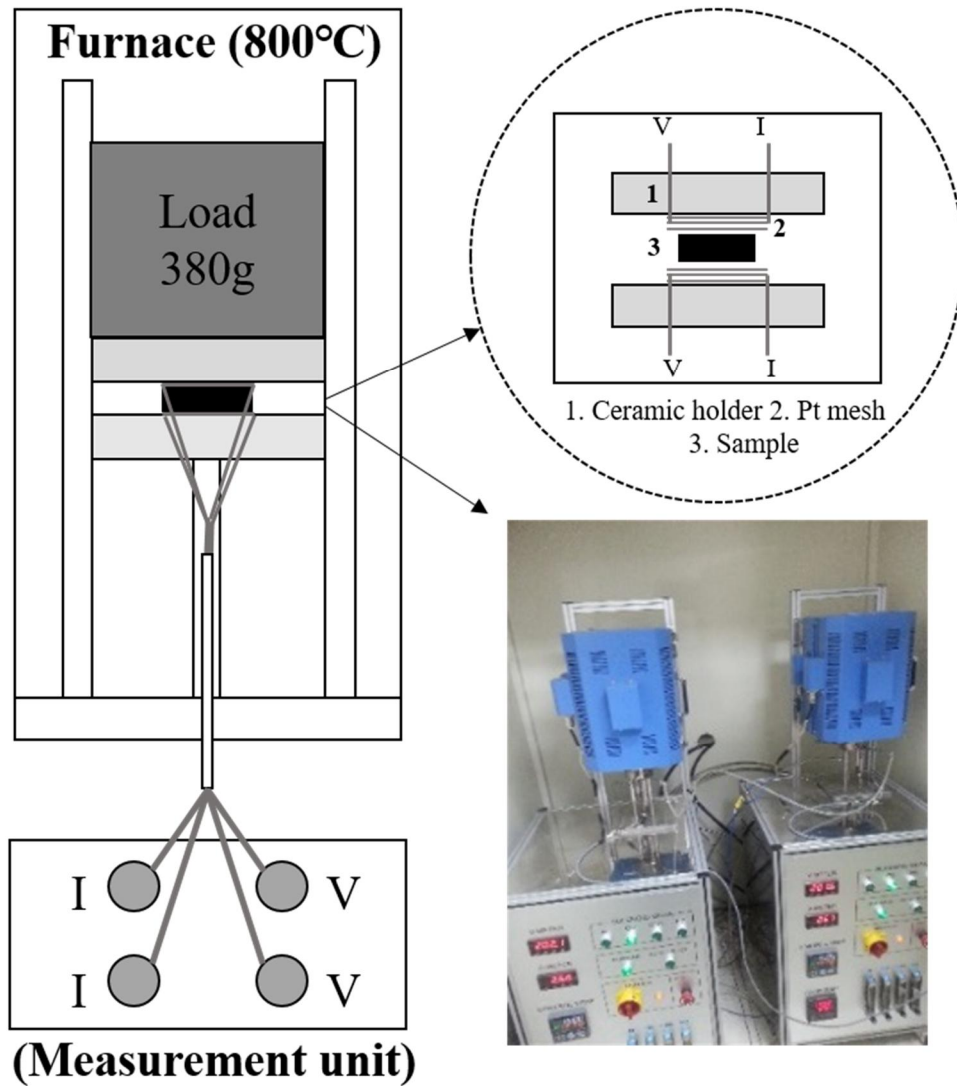
Figure 4.2 Schematic diagram of ASR measurements

Variable currents of -1 to +1 A with a step size of 0.2 A were applied. Then the voltage value was measured with a 10 min time interval. The heating rate was 200 ˚C per hour, and when the temperature reached 800 ˚C, the temperature was maintained. The results were obtained after 50 h measurements for considering the firing of Pt paste, and the linearity of the I-V curve was maintained at 1. Therefore, the electrical resistance of the thermally grown oxides was obtained from the slope of the I-V curve according to Ohm's law, and this measured resistance was multiplied by the area of the sample surface to get the ASR value. In this paper, all ASR values were divided by 2 to directly compare the thickness results of the oxide scale formed on one side of the surface. For the reliability of the ASR results, all measurements were conducted more than three times in each composition, and the average values of ASR measurements with the deviation were obtained.

Analyses of the oxidation behavior of La-added alloys

Mass gain experiments were conducted to observe the macroscopic oxidation behavior of La-added alloys. Dimensions of each sample were measured before the oxidation test. The isothermal oxidation experiments were conducted at 800 ˚C in the box furnace, and their mass changes were measured using a microbalance (MSE3.6P, Sartorius, Germany). Three specimens in each composition were used to get reliable mass gain results.

  SEM (S-4300SE, Hitachi, Japan) equipped with an EDS detector (XFlASH, Bruker, Germany) was used for cross-sectional analyses for the microscopic view of the oxidation behavior. In addition, the focused ion beam (Nova 600 NanoLab, FEI, USA) device was used to make a TEM lamellar from each 500h oxidized specimen for a more precise analysis. The average phase fractions of these specimens were determined by TKD (OPTIMUS^{TM} TKD, Bruker, Germany) method and also, and compositional analyses were conducted using the TEM (Talos F-200X, FEI, USA) equipped with an EDS system (Super-X^{TM}, Bruker, Germany).

Near Edge X-ray Absorption Fine Structure (NEXAFS) and Extended X-ray Absorption Fine Structure (EXAFS) measurements were performed to get general information on the oxides. La-added alloys with different oxidation times (100h, 300h, 500h) were prepared, and the oxides characterization was conducted using the synchrotron X-ray at the PAL-KIST beamline (Pohang Acceleration Laboratory, South Korea). NEXAFS spectra of each specimen were obtained near the La M5-edge (836eV) in the Total Electron Yield (TEY) mode at the 10D beamline, and these results were compared to the NEXAFS result of reference La_2O_3 powder (Sigma Aldrich, 99.9%). Also, EXFAS analysis was performed near the Mn K-edge (6539eV) in the Fluorescence Yield (FY) mode at 1D beamline to compare the average Mn oxidation state of the oxides.

In addition, in-situ techniques were performed to interpret the oxidation behavior at high temperatures. Especially an in-situ heating system in SEM (S-4300SE, Hitachi, Japan) observed the diffusion of the undissolved La region on the surface.

Post-processing the digital images obtained from SEM

Back-scattered electron (BSE) images from SEM were obtained to measure the precise thickness of inhomogenous formed oxides. A quick selection tool that could select similar pixels based on tone and color in the Photoshop program (Adobe Photoshop CS6, Adobe Systems, USA) was used to calculate the total counts of the pixels corresponding with the oxide layer. As the image's pixel size and width were already determined when getting a BSE image, the average thickness of the oxide layer could be determined in the BSE image, as shown in Figure 4.3. In this manner, numerous BSE images in each condition were analyzed for the thickness calculations, and the observed regions were more than 400 μm in width.
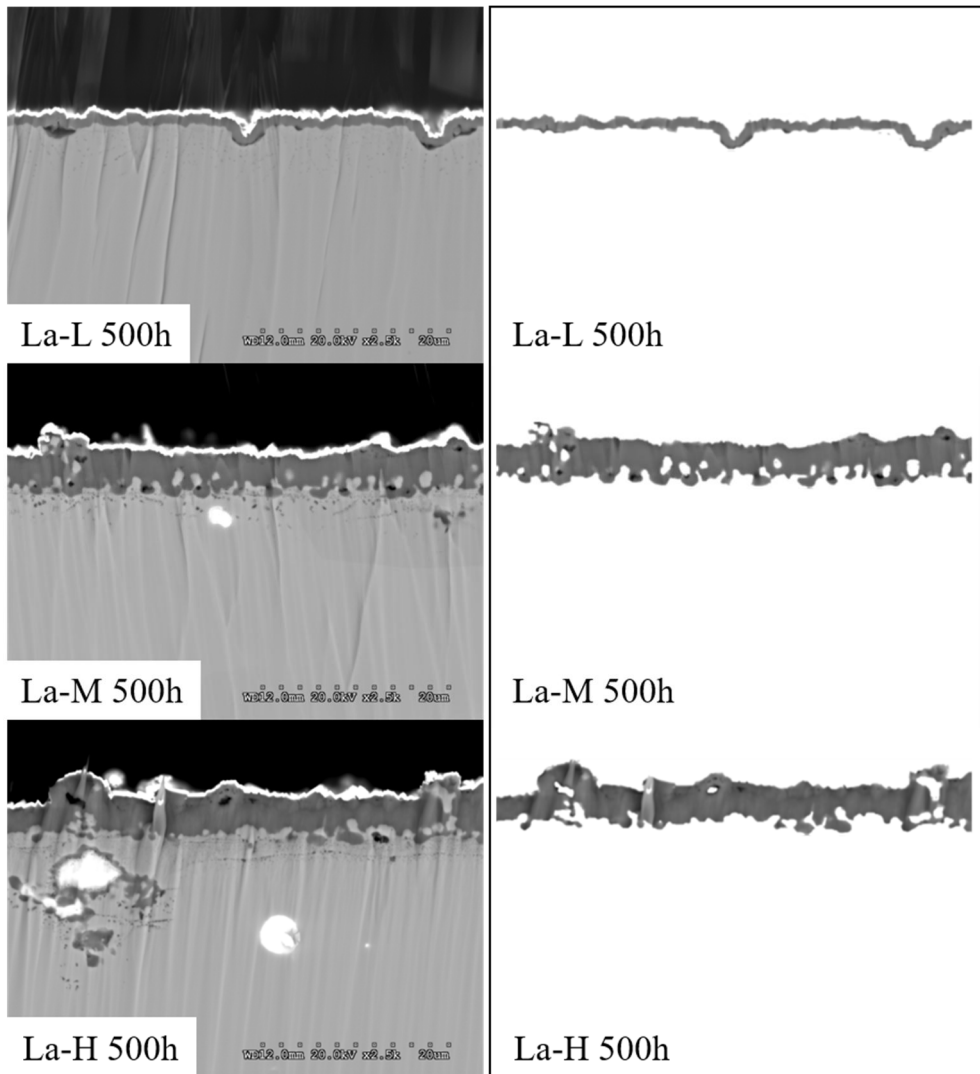
Figure 4.3 Cross-sectional BSE images of oxidized specimens (left) and the extracted oxide layer using the photoshop program (right)

Also, additional analysis was performed to quantify the voids in the oxide or the oxide/metal interface. Cross-sectional BSE images of 500h oxidized specimens were analyzed using Fiji, an open-source package for image processing [88]. For reliability, voids in numerous BSE images (more than 20 images in each specimen, and the total observed width is more than 500 μm) were characterized using the Trainable Weka Segmentation tool [89]. Using this tool, users quickly make trainable classifiers for their own needs, and the schematic diagram for the training classifier is illustrated in Figure 4.4. To find an optimum classifier, the number of trained images increased one by one, as shown in Figure 4.5. Figure 4.5 exhibits that the classified results were stabilized after seven images were applied for trainning the classifier. In this manner, seven images in each specimen were used to train each classifier and this trained machine learning tool segmented the remaining data automatically. In this manner, statistical void distribution can be obtained.
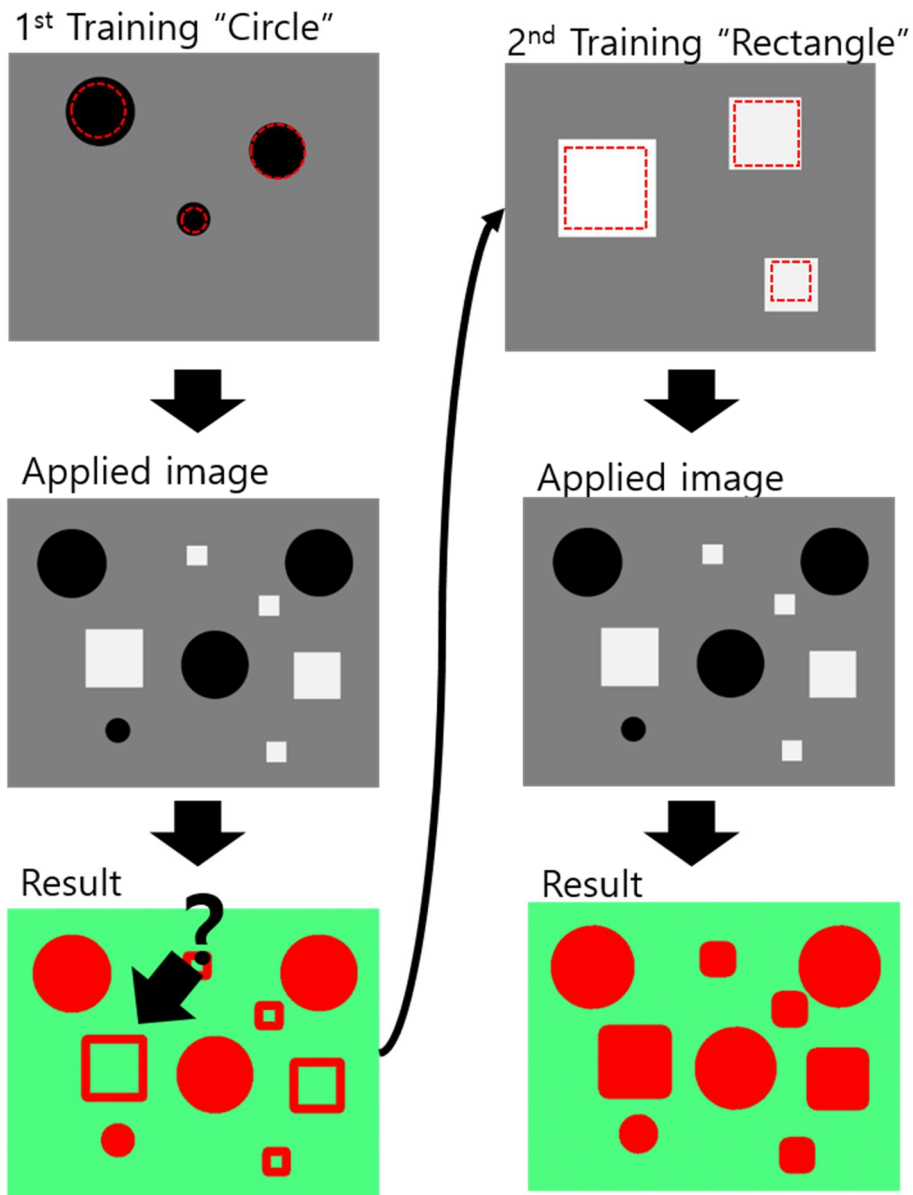
Figure 4.4 Schematic diagram of the process

of making trainable classifier
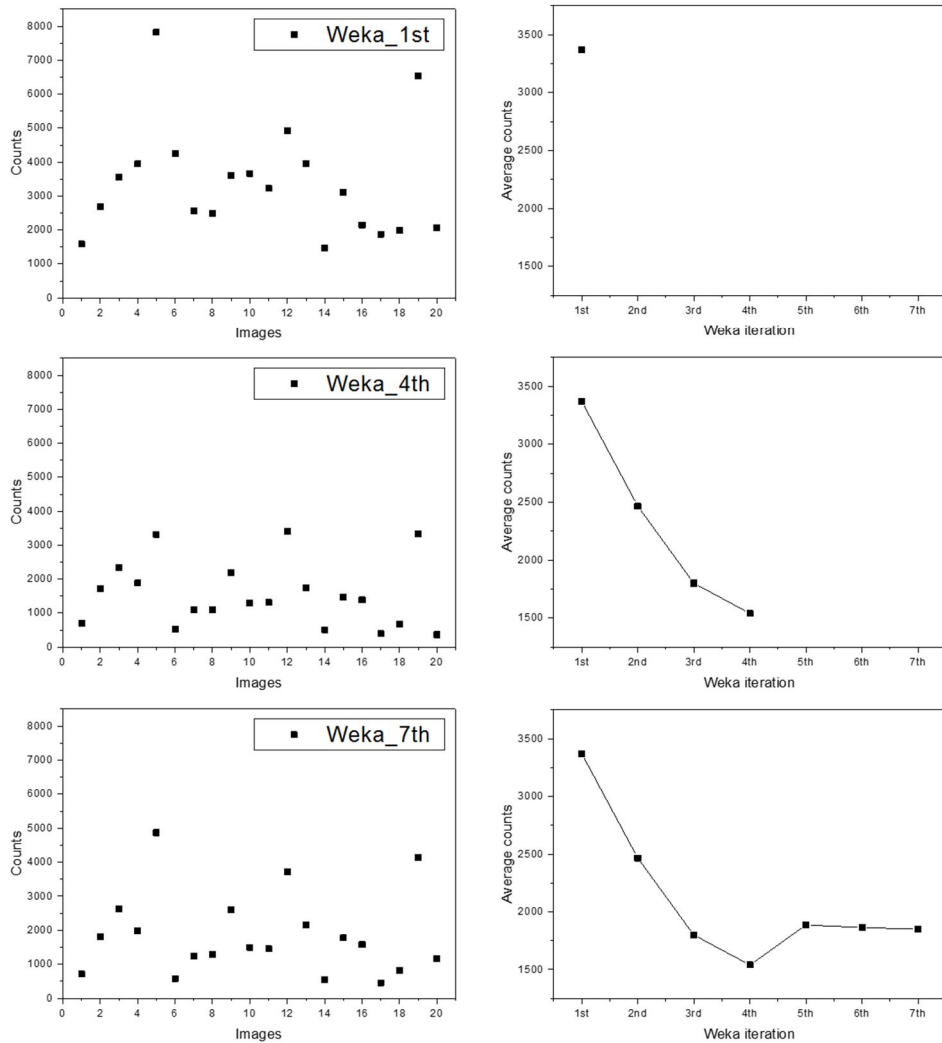
Figure 4.5 Stabilization of classified results after seven images were

applied for training classifier

4.2 Results

4.2.1 La addition effect on the initial microstructure of La added alloys

Because of the low solubility of La in ferritic stainless steels [33, 90], the undissolved La regions were observed in highly La-added alloys. Lanthanum is much heavier than the other alloying elements, so the undissolved La regions were easily classified in BSE images, as shown in Figure 4.6. These results exhibit that the maximum surface fraction of undissolved La regions is only below 2%. In addition, the undissolved La regions seem to be randomly distributed in La-added alloys, as shown in Figure 4.7. These regions were similarly observed in the grain boundaries and intra-grain regions. The detailed analysis was conducted using SEM with EDS in Figure 4.8. The complex microstructure, consisting of non-metallic inclusions (named La inclusions in this study) and La-Ni intermetallics, was observed in the undissolved La regions.
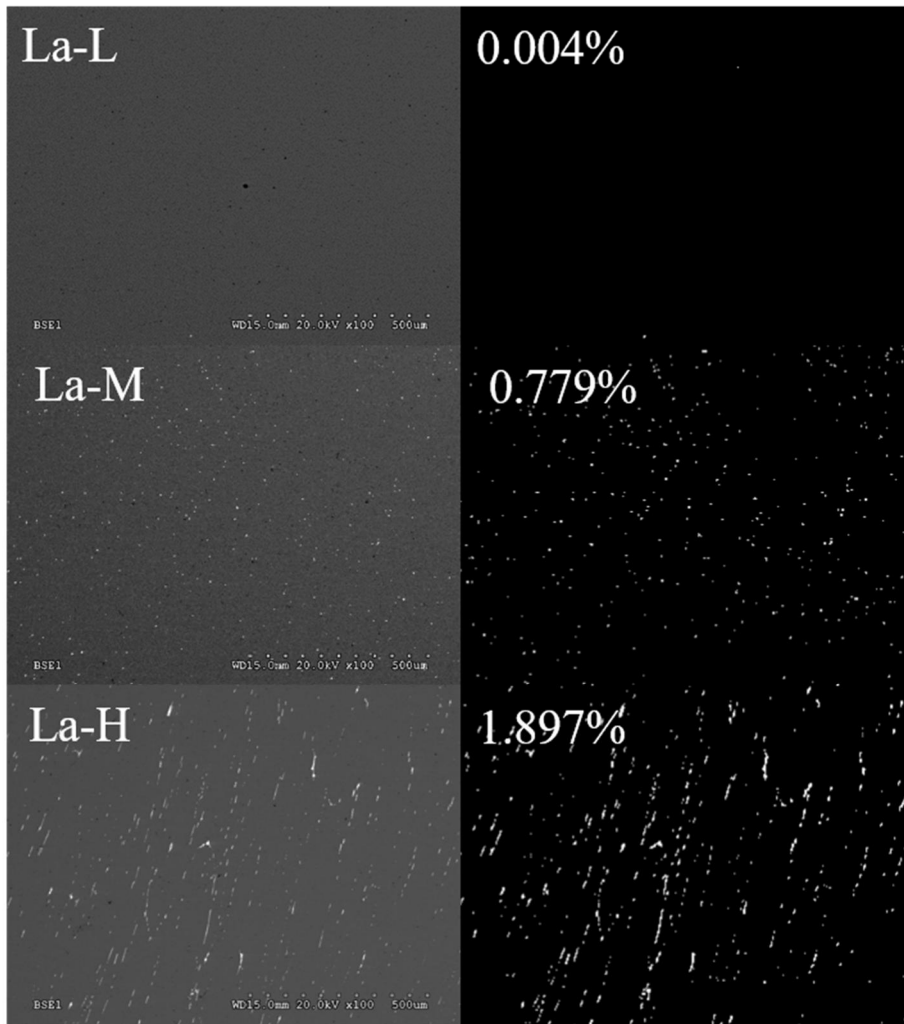
Figure 4.6 BSE images of the surface of La added alloys (left) and the classified undissolved La region using the Photoshop program (right)
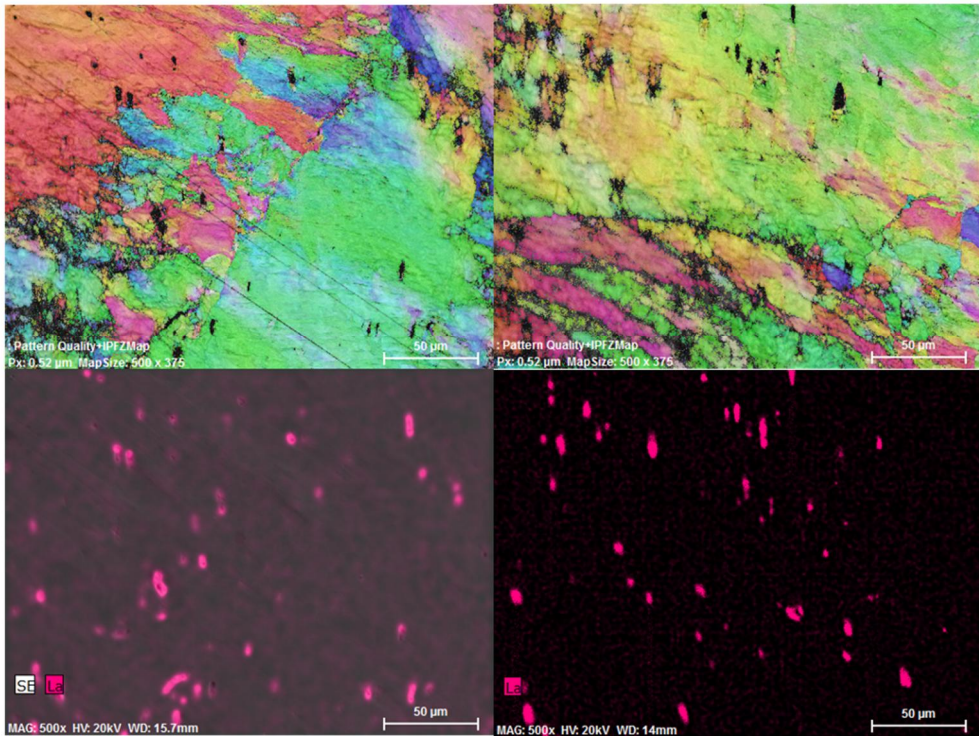
Figure 4.7 The initial distribution of undissolved La regions in La added alloy
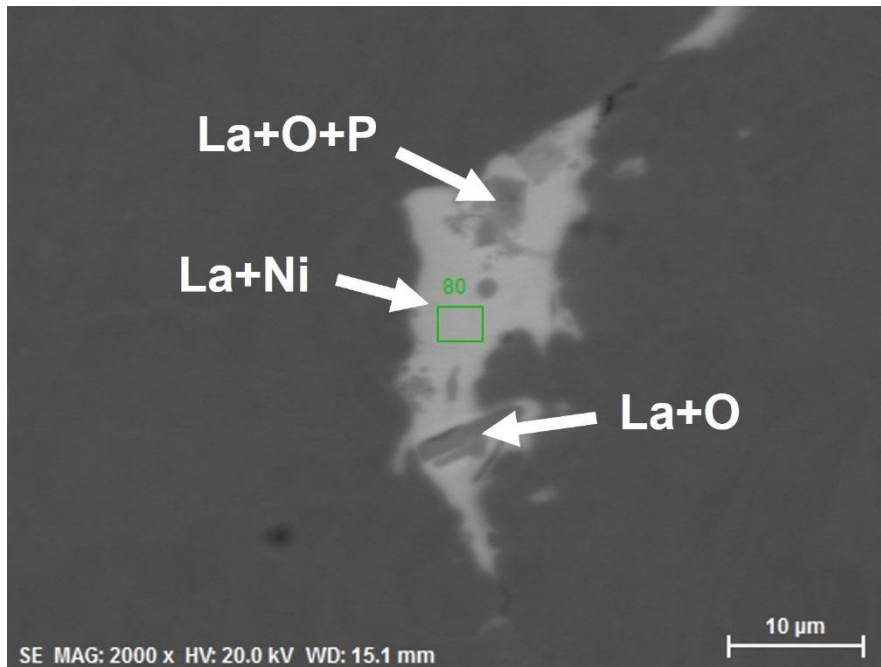
Figure 4.8 Complex microstructure of undissolved La regions measured

by SEM and EDS

The possible reaction and the Gibbs free energy of the formation are listed below:

$$3La + 1.5O_2 = La_2O_3 \rightarrow -1706077 \; J/mol \; at \; RT (4.1)$$

$$3La + Ni = La_3Ni \rightarrow -6118.2 \; J/mol \; at \; RT (4.2)$$

$$7La + 3Ni = La_7Ni_3 \rightarrow -179786 \; J/mol \; at \; RT (4.3)$$
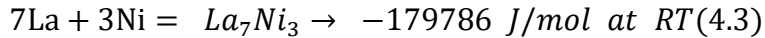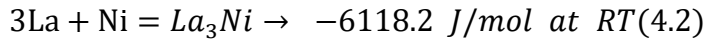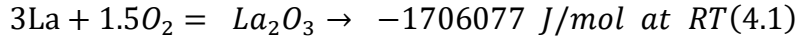
It seems that the formation of La inclusions is thermodynamically more favorable than the formation of La-Ni intermetallics. TEM results also exhibit that impurities, like S, P, or O, were favored in La inclusions, as shown in Figure 4.9. The x in the average composition of La_x(O, P, S) was approximately 0.936 from the EDS measurements, but this composition was not well matched with the single compound, as shown in the phase diagrams in Ref [91]. This result indicates that the La inclusions consisted of complex phases. Assuming that all of the impurities in the alloys react with La, we can calculate the required amount of La in the alloys, as listed in Table 4.2. It proves that even if all impurities were reacted to form La inclusions, more than 65% of La could remain unreacted in La-M and La-H.
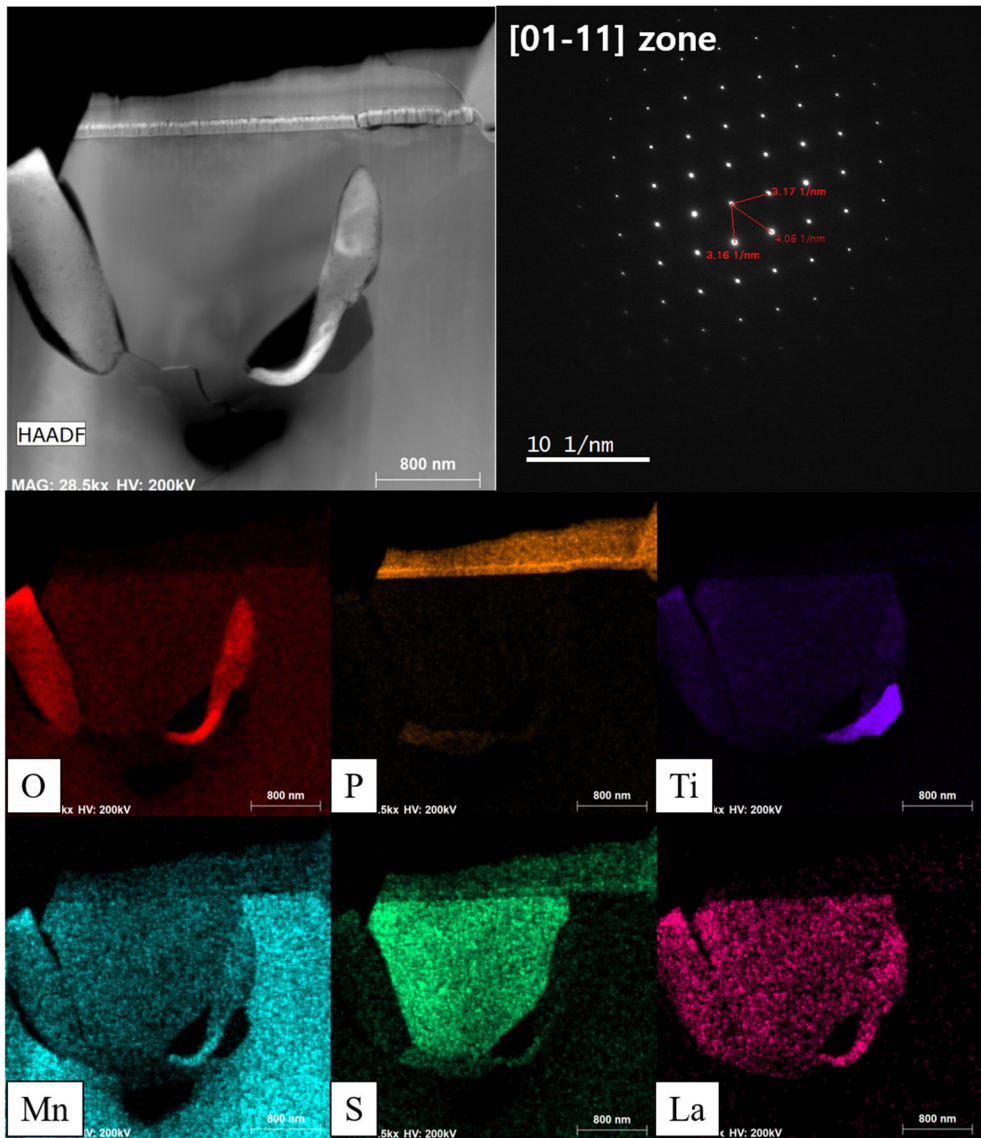
Fig 4.9 TEM results of La inclusions from as received La-M specimen
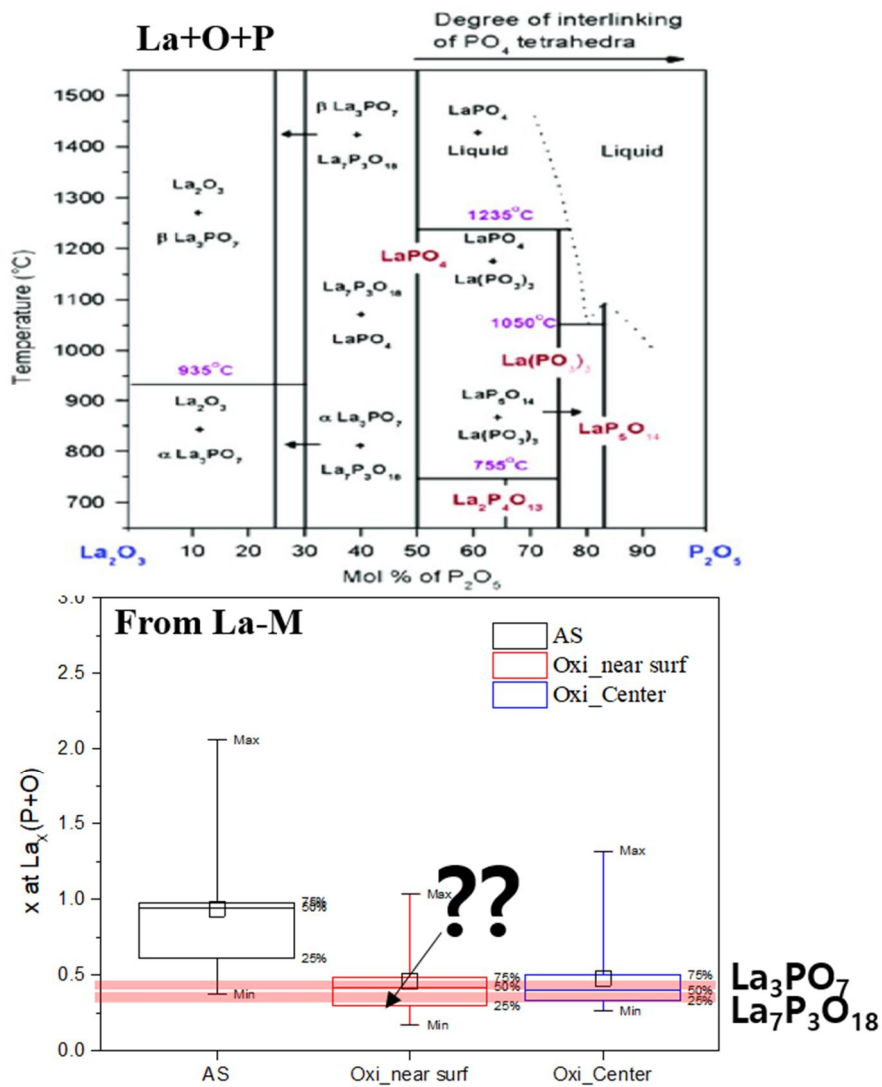
Figure 4.10 Phase estimation of La+O+P regions using a Phase diagram

[91] (top) and EDS results (bottom)

Table 4.2 Calculation of the required amount of La and Ni in the alloys to form the La inclusions and La-Ni intermetallic

At.%	La	Ni	Total O, P, S	Max. required La for La inclusion	Min. remained La in the matrix	Min. required Ni for La-Ni intermetallic
La-L	0.002	0.494	0.049	0.046	-	-
La-M	0.043	0.485	0.017	0.016	0.027	0.009
La-H	0.237	0.496	0.047	0.044	0.193	0.064

Figure 4.11 exhibits the possible La-Ni phases from the phase diagram, and EDS results suggest that the main phases of La-Ni intermetallics would be La_3Ni or La_7Ni_3. As mentioned above, unreacted La seems to remain after forming the La inclusions, and Table 4.2 indicates that a sufficient amount of Ni exists to react with the remaining La. Therefore, the undissolved La regions were understood as the La inclusions surrounded by the La-Ni intermetallics.

The amount of dissolved La in the matrix at room temperature seems negligible because most of La was consumed by the undissolved La regions. The TOF-SIMS depth profile results supported this assumption, as shown in Figure 4.12.
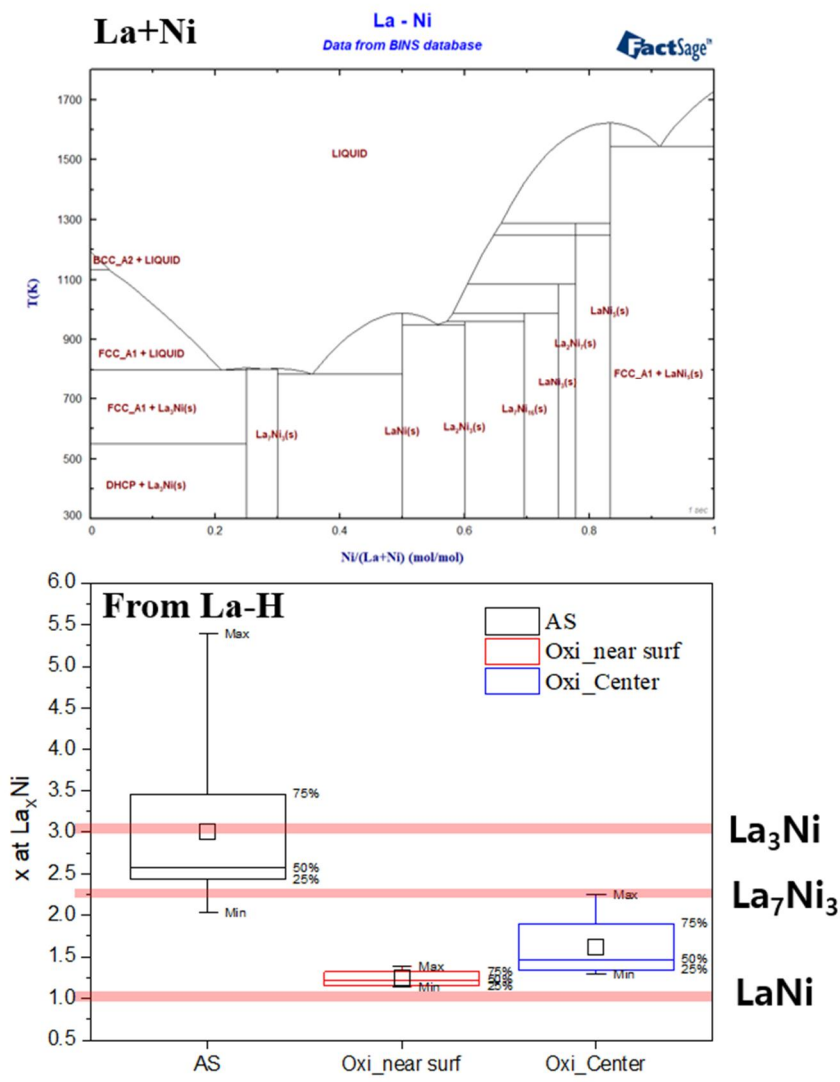
Figure 4.11 Phase estimation of La-Ni regions using a Phase diagram (top) and EDS results (bottom)
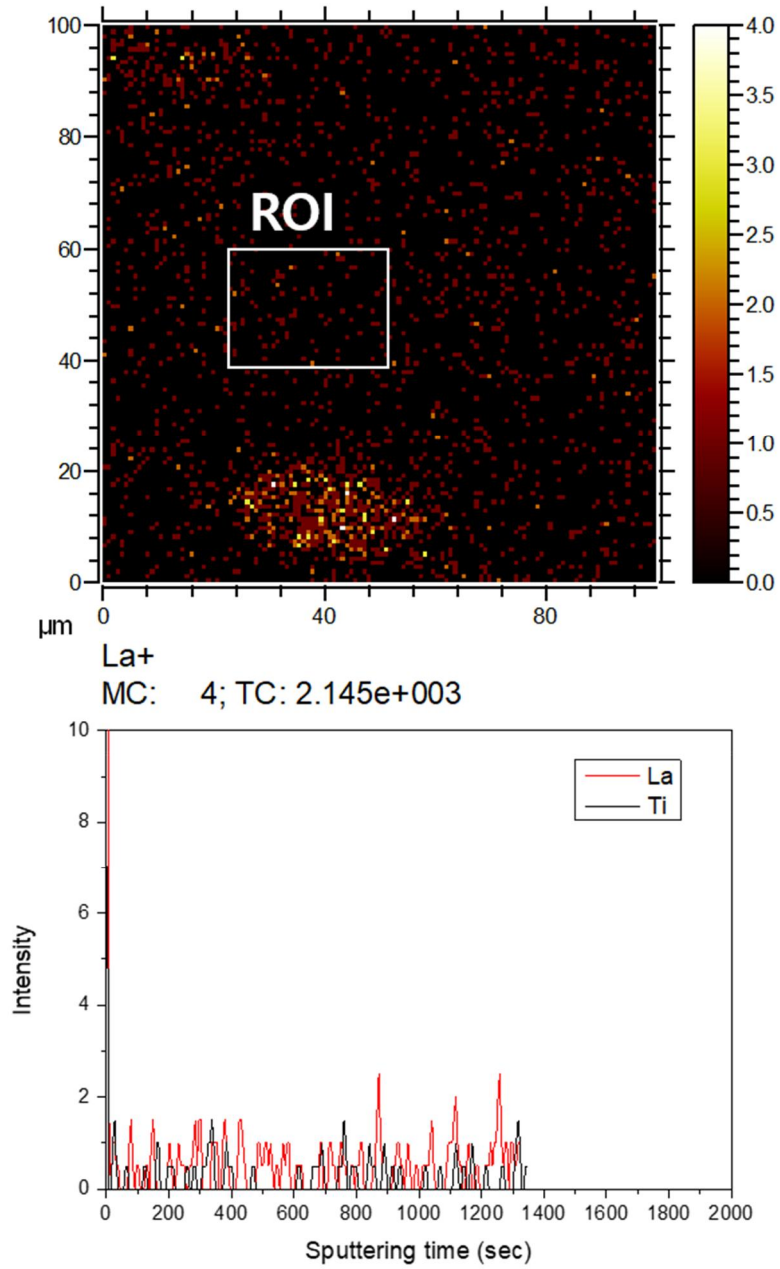
Figure 4.12 SIMS La mapping result of La-M specimen (Top) and depth

profile results of the interested region (Bottom)

4.2.2 Oxidation behavior of La added alloys

Similar to Ref[90], high La addition accelerated the oxidation kinetics, as shown in Fig 4.13. The weight gain values of La-M and La-H are remarkably higher than La-L. The weight gain results of those two specimens are similar until 300h, but La-H begins slightly higher than La-M after 300h. The thickness analysis from BSE images exhibits the same trend that the La-L always has the thinnest oxide scale compared to the higher La-added alloys, as illustrated in the upper right graph in Fig.4.14. One interesting point is that the thickness of the La-H, which shows similar weight gain results of La-M up to 300 h, is thinner than that of the La-M. As mentioned in section 4.2.1, two initial microstructures of La added alloys-undissolved La regions and the matrix region were observed on the surface. Therefore, the effect of each region on the oxidation behavior was considered comprehensively.

First, severe oxidation in undissolved La regions on the surface was observed, as shown in Figure 4.15. These regions were rapidly oxidized even after a 100h oxidation test because of the high oxygen affinity of La [28, 92]. A continuous oxide layer was formed surrounding the downside of the La oxides, and a contact layer with La oxides was close to the Mn-Cr spinel. In addition, the Cr_2O_3 layer was formed beneath the Mn-Cr spinel layer. One interesting feature is that the penetration of the oxide layer in the undissolved La regions is more severe than in the matrix regions. This finding indicates

that La oxides on the surface can act as oxygen suppliers to the surrounding regions. Despite the small fraction, the undissolved La regions on the surface appear to affect the macroscopic weight gain results, especially in the initial oxidation stage. As a result, La-H, which contains the most undissolved La regions on its surface, exhibits similar weight gain values as La-M, despite the thinner oxide scale up to 300h.

Second, TKD analysis was performed on each La-added alloy after the 500 h oxidation test for the detailed thickness comparison, as illustrated in Figure 4.16. The continuous Cr_2O_3 and Cr-Mn spinel oxide layers were formed in the matrix regions, similar to the previous research [31]. The Cr_2O_3 and Mn-Cr spinel layers consisted of several tens of nanometer-sized grains and hundreds of nanometer-sized grains, respectively. The average grain size of each specimen is obtained as listed in Table 4.3, and it exhibits that the grain size of the chromia slightly increases as the amount of La increases.

For the next step, the phase fraction of the oxides were obtained from TKD analysis. The average thickness of the total oxide layer was already measured in Figure 4.14, so the calculated thickness of each oxide is illustrated in Figure 4.16. Interestingly, the Cr_2O_3 thickness increases as the amount of La in the alloy exceeds a specific value (~0.08wt.%). The increase of Cr_2O_3 peak intensities in GI XRD results supports this tendency, as shown in Figure 4.17. On the other hand, a significant change in thickness according to the La addition is not observed in the spinel layer.
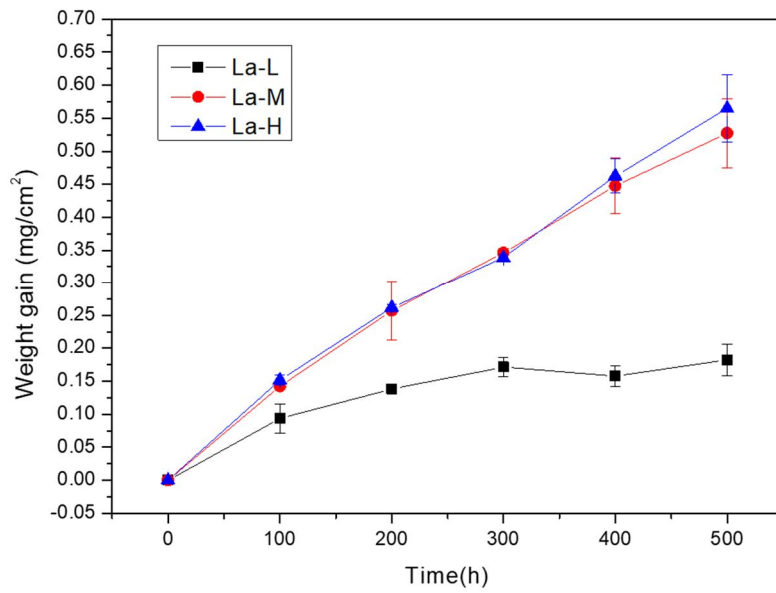
Figure 4.13 Isothermal weight gain results of La added alloys
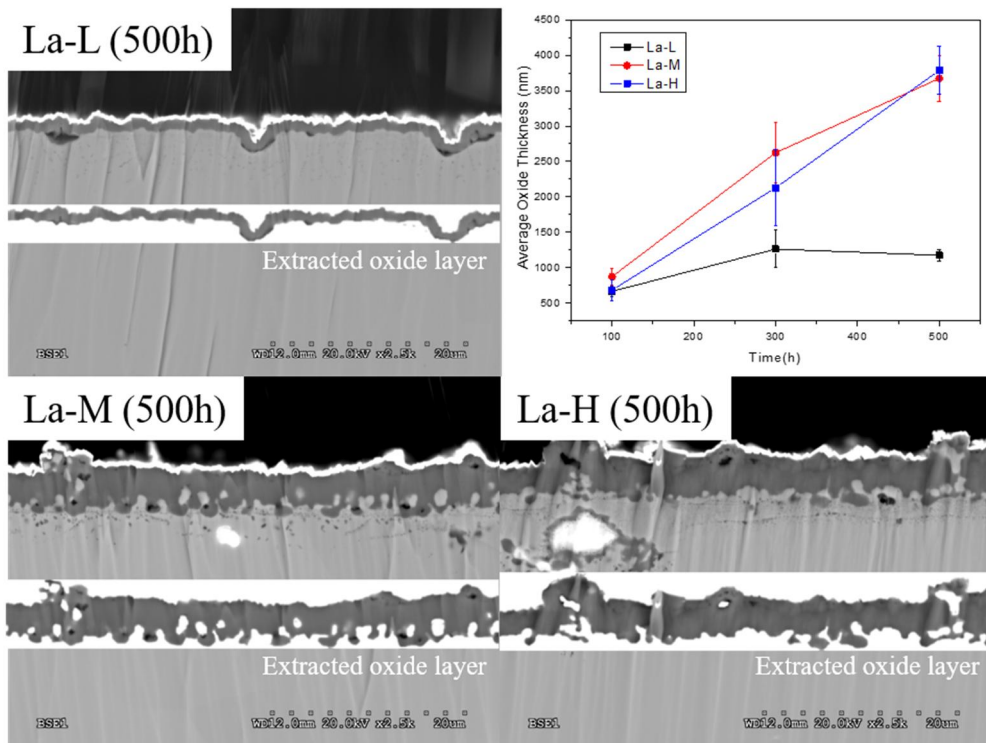
Figure 4.14 Cross-section BSE images after 500h oxidation test and the

measured average thickness of oxides formed in the matrix region
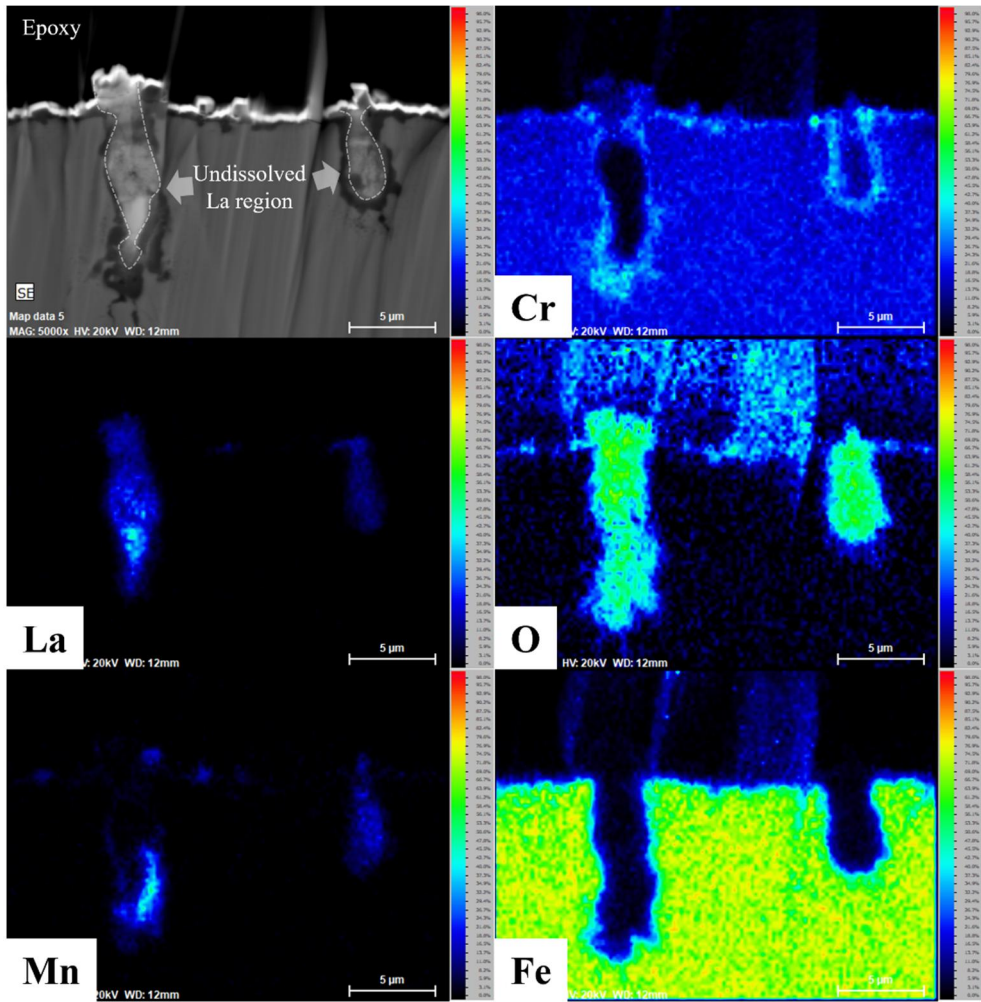
Figure 4.15 Cross-section EDS results obtained from the undissolved La regions after 500h oxidation test
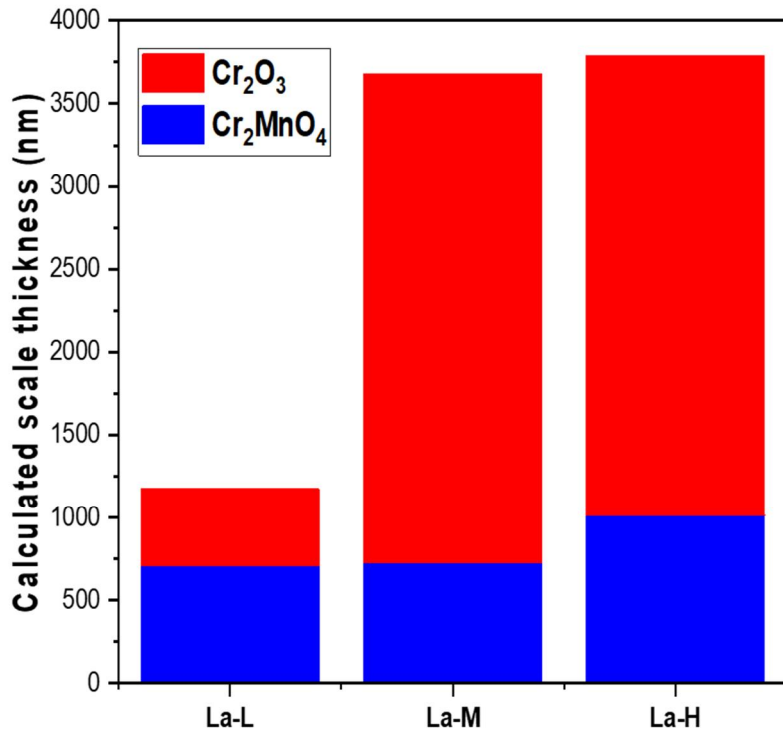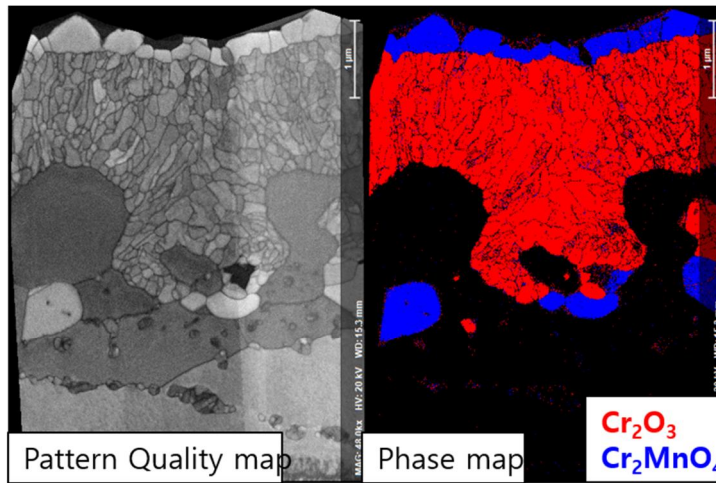
Figure 4.16 TKD results of La-M after 500h oxidation (up) and the calculated oxide scale thickness of each specimen in the matrix regions (down)

Table 4.3 Average grain size of oxides after 500h oxidation test

	Cr_2O_3	Cr_2MnO_4
La-L	177nm	530nm
La-M	220nm	486nm
La-H	236nm	1100nm
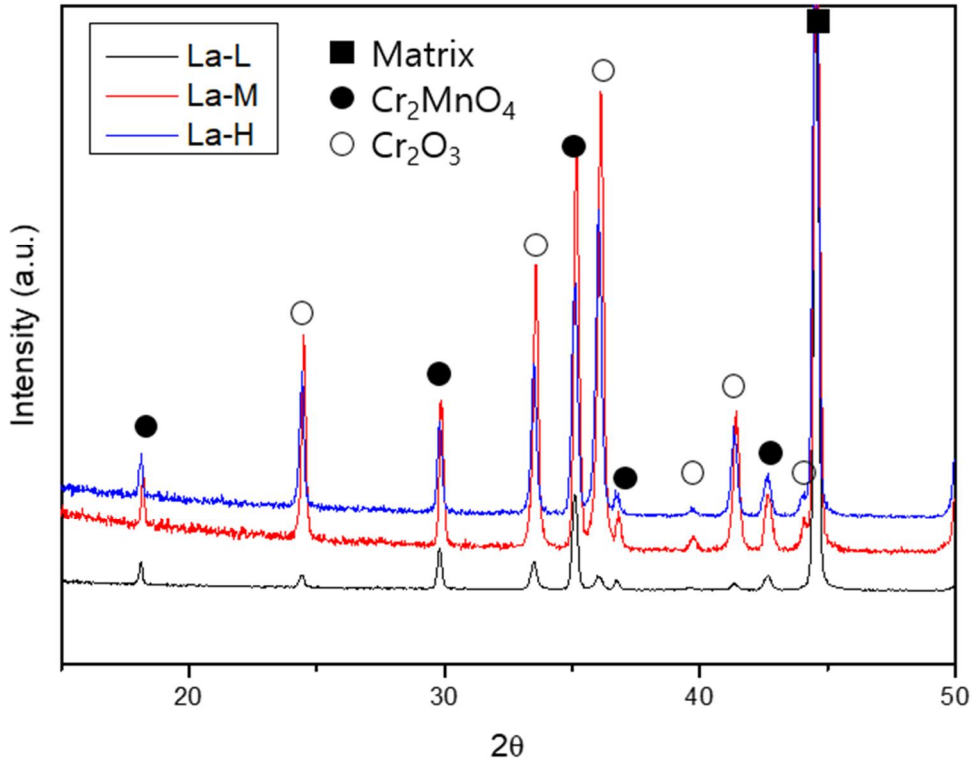
Figure 4.17 GI-XRD results of oxidized specimens after 500h oxidation test

4.2.3 Electrical property of oxide layers on La added alloys

The change in ASR results of La added alloys with time is shown in Fig.4.18. The ex-situ measurements successfully exhibit the increase of ASR over the oxidation time. Considering that ASR results were already divided by 2, ASR levels of high La added specimens (La-M and La-H) are near $0.05\Omega cm^{2,}$ and these values seem acceptable [93-95]. However, the ASR level of the La-L specimen is significantly higher than the others. Basically, the ASR value can be expressed as [38, 96]

$$ASR = \sum \rho * t \quad (4.4)$$

where ρ is the oxide resistivity, and t is the thickness of the oxide layer. It should be noted that the effect of the alloy substrate was neglected. The thickness of the metal substrate (~ 2 mm) is thicker than the oxide layer (~ 4 μm), but the electrical resistivity of Cr_2O_3 [94, 97, 98] and Mn-Cr spinel [99, 100] was much higher than that of Fe [101] at 800 ˚C, as noted in Table 4.4. As expected by Equation 4.4, ASR increased over time due to scale growth. However, La-L, which has the thinnest oxide scale in the matrix regions, exhibits the highest ASR values in the entire measurements.
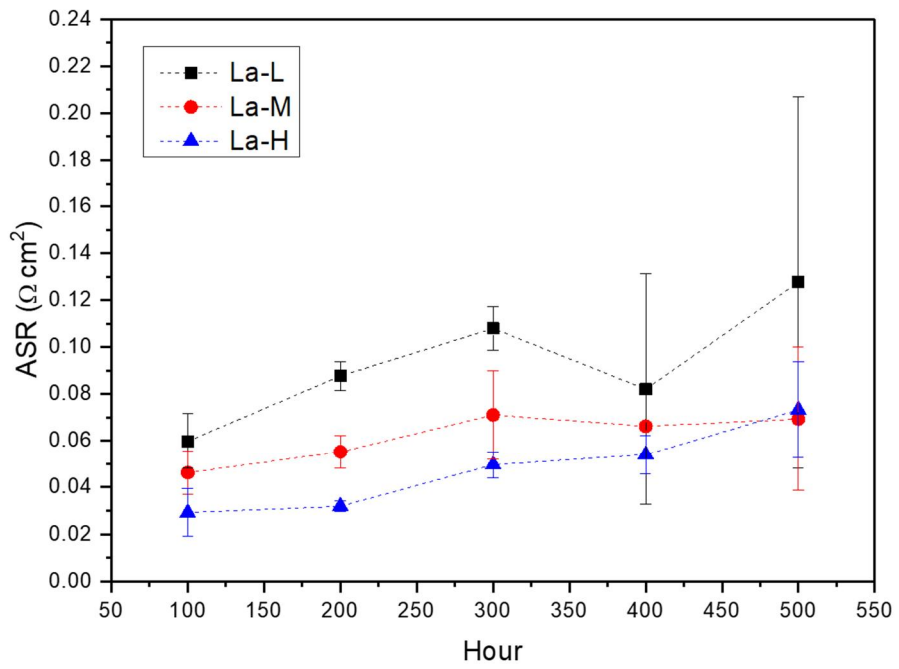
Figure 4.18 Ex-situ ASR result of La added alloys

Table 4.4 Electrical resistivity of the oxides (Ωcm)

Cr_2O_3	Cr_2MnO_4	*cf.* Fe
100 at 800 ˚C	330 at 800˚C	0.001 at 796˚C
[94,97,98]	[99,100]	[101]

Therefore, the La addition effect on oxide resistivity, another factor to affect ASR, was also investigated. (The experimental data on the resistivity of each oxide layer are not included in this study. Instead, the author only focuses on comparing each oxide layer according to the La addition.)

The change in the resistivity of Cr_2O_3 was considered first due to the extrinsic behavior below 1000 ˚C [102, 103]. A small amount of impurities like Ti^{4+}[104], Li^+[105, 106], or Mg^{2+}[107] can affect the resistiviy of Cr_2O_3. TEM EDS line mapping results in Figure 4.19 reveals that tiny amounts of Ti, Fe, and La are observed in the oxide layer, and the detailed composition results are noted in Table 4.5. Because of the overlapping problem of characteristic c X-ray lines of Ti and La [32, 108], it is difficult to determine the existence of La in the oxide scale. However, even assuming those minor elements affect the Cr_2O_3 layer, the total amount of minor elements is independent of the amount of La in alloys. Thus, this study did not account for how much the addition of La altered the resistivity of the Cr_2O_3 layer.

Second, the change in the resistivity of the spinel layer due to the La addition was estimated. Mn is known to exist as Mn^{2+} ions and to occupy the tetrahedral sites in the Mn-Cr spinel oxide when the stoichiometry of $MnCr_2O_4$ maintains. However, when the Mn content increases in the spinel, Mn ions with a higher valence state can occupy the octahedral sites, increasing the electrical conductivity [109]. From this perspective, an EXAFS analysis, which is very sensitive to changes in the local structure, has been

carried out to compare the Mn state in the spinel layer. Interestingly, noticeable changes were not found in the EXAFS spectra and their first derivative results, as illustrated in Figure 4.20. It indicates that the Mn state in the spinel layer is independent of the amount of the La addition or the increase of oxidation time. Therefore, the electrical resistance of spinel oxides can be assumed to be similar despite the different amounts of La in alloys.
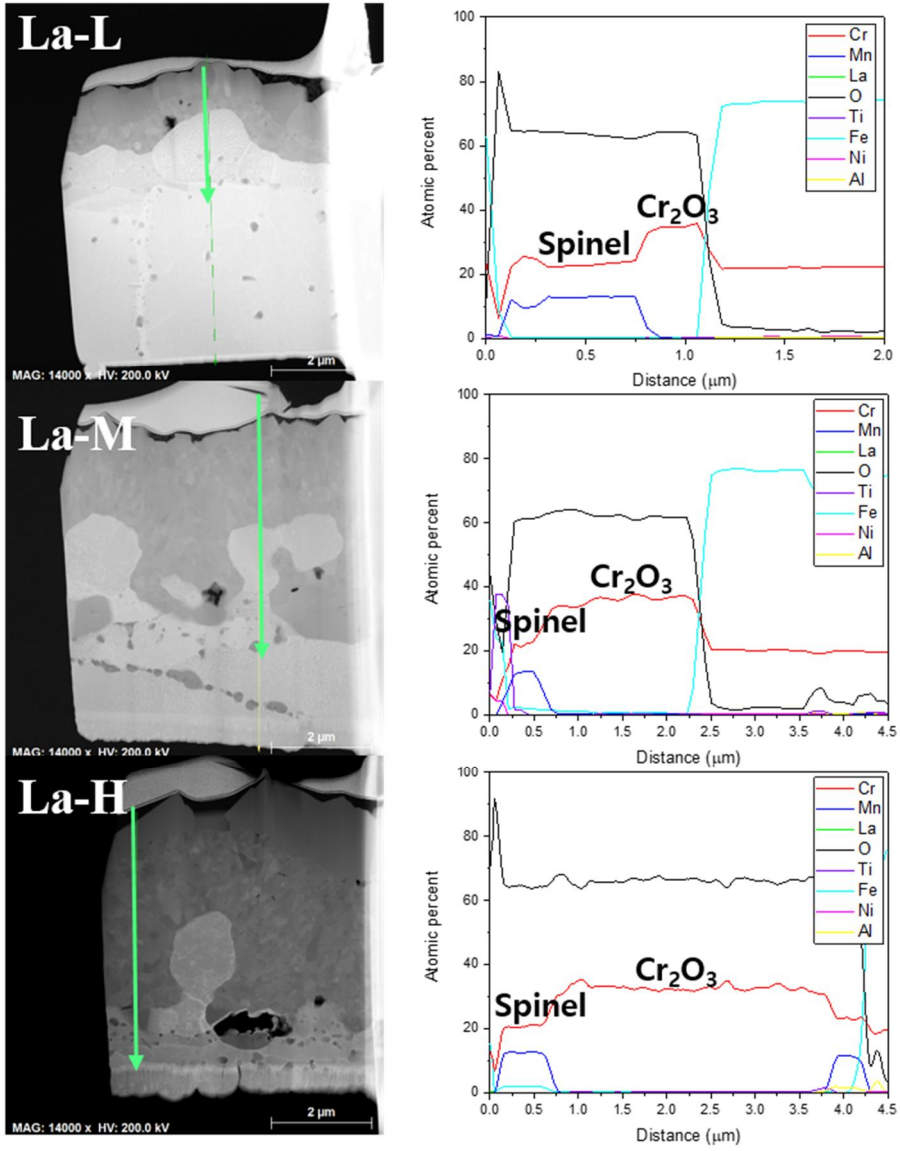
Figure 4.19 Compositional line profile of oxidized specimens using TEM

Table 4.5 Average composition table of thermally grown oxides from TEM EDS results

at.%	Cr	Mn	O	La	Ti	Fe
La-L (Cr_2O_3)	38.88	0.35	60.09	0.02	0.18	0.48
La-M (Cr_2O_3)	38.62	0.25	59.85	0.04	0.27	0.97
La-H (Cr_2O_3)	36.95	-	62.53	0.04	0.31	0.15
La-L (Spinel)	29.77	17.35	52.05			0.83
La-M (Spinel)	25.65	15.69	56.28			2.37
La-H (Spinel)	24.26	16.3	57.09			2.35
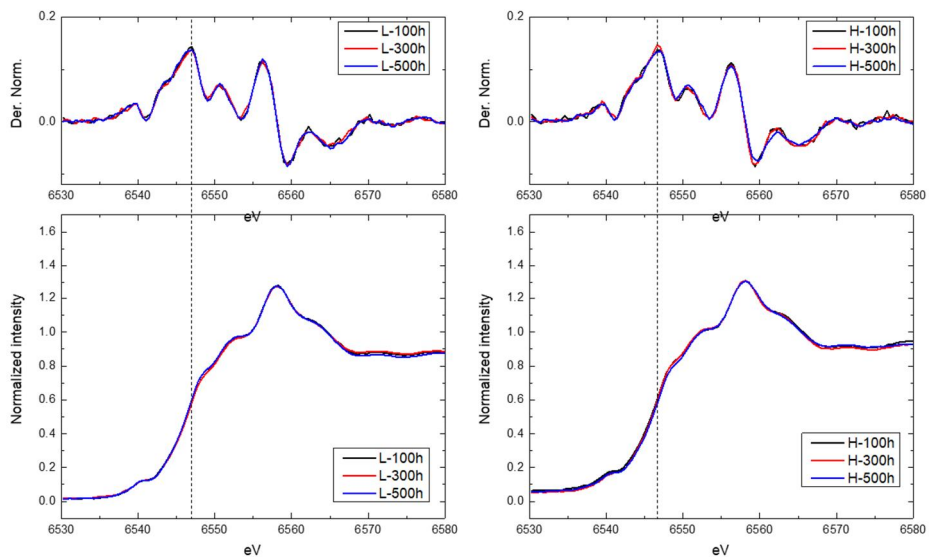
Figure 4.20 EXAFS results near the Mn K-edge (6539eV) of La-L and

La-H after oxidation test

Another interesting feature is that the measured Fe content in the spinel layer was higher in highly La-added alloys compared to the La-L specimen. Fe protrusion induced by the severe inward oxidation might be the source of Fe diffusion to the spinel, as shown in Figure 4.21. Unfortunately, to the best of the author's knowledge, none has been reported the electrical conductivity change of Fe-doped Cr_2MnO_4. Li is the only well-investigated element in Cr_2MnO_4 because Li-doped Cr_2MnO_4 is one of the desirable p-type transparent conducting oxides in the optoelectronic application field [110, 111]. Some authors reported that Fe tends to decrease the electrical performance in the $MnCo_2O_4$ [112, 113]. However, because $MnCo_2O_4$ is known as the inverse spinel and Cr_2MnO_4 is known as the normal spinel [111], the site occupancy of $MnCo_2O_4$ may differ from that of Cr_2MnO_4. It means that Fe can show different tendencies when dissolved in Cr_2MnO_4 and the effect of Fe in the spinel is still ambiguous. Thus, it should be noted that this effect will not be considered in this study to simplify the calculation of the ASR value.
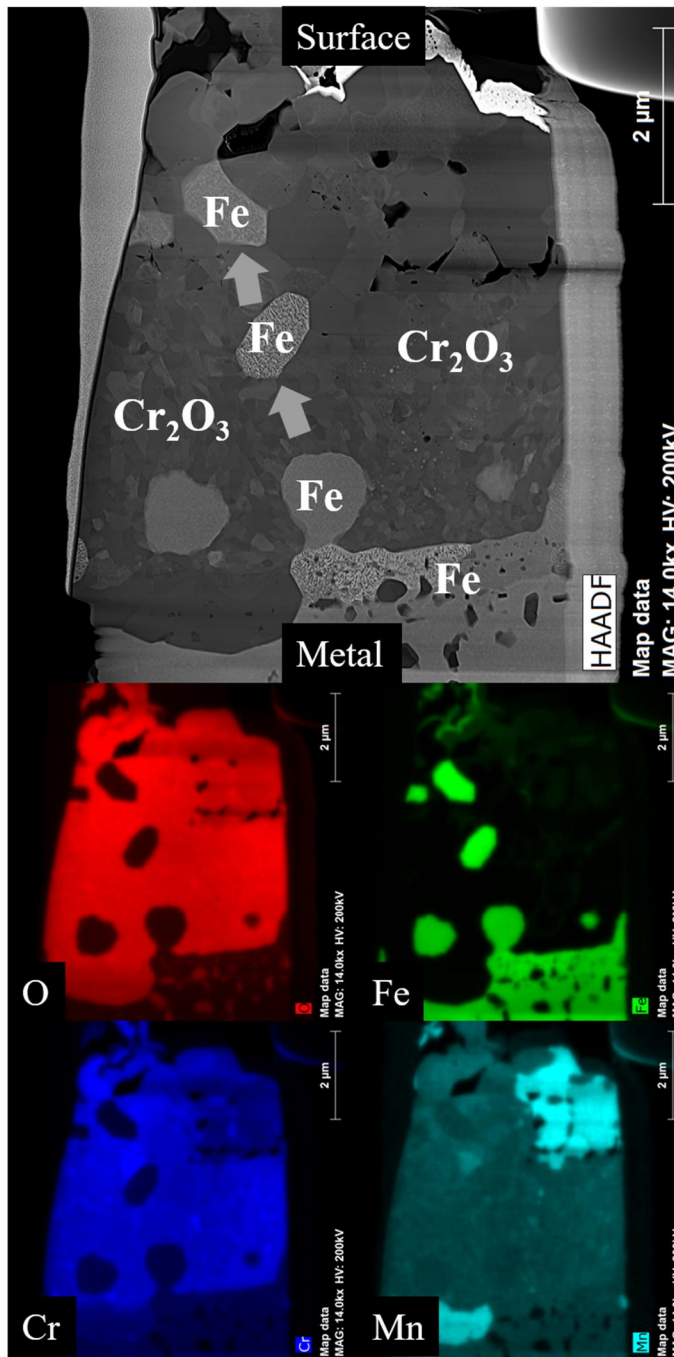
Figure 4.21 Fe protrusion to the oxide scale due to the severe inward

oxidation

4.2.4 La measurements of oxidized specimens

There have been a number of experiments to observe the effect of reactive elements (RE). For example, it was well known that inward oxidation was promoted, but outward oxidation was suppressed in reactive element-added alloys. Similarly, the growth rate of the Cr_2O_3 layer, which exhibited inward growth beneath the spinel layer from the gold marker experiments [114], was accelerated as the amount of La increased in this study. On the contrary, the growth rate of the spinel layer, known to grow outward, seems to be independent of the La addition, as shown in Figure 4.16. Therefore, La measurements of the oxidized specimens were conducted to understand the REs effect properly. It has been known that REs can be observed in three regions after oxidation; 1) Gas/oxide interface, 2) Oxide grain boundary, and 3) oxide/metal interface [28]. In addition, La can exist undissolved in the matrix, as observed in this study. Based on these assumptions, the corresponding regions were investigated sequentially.

First, the NEXAFS analysis was conducted to investigate the gas/oxide interface, as shown in Figure 4.22. All results were obtained near the La M5-edge (~836eV) over oxidation time using TEY mode, of which the sampling depth at the Si K-edge (1840 eV) was only 70 nm [115]. Small peaks of the La-H specimen after 100h oxidation are observed and well-matched with the

La$_2$O$_3$ reference powder, as illustrated in Figure 4.22. It is similar to Zhu's work [25] which detected La in the gas/oxide interface on the initial oxidation stage (Max. one hour). Probably, this result appears to indicate the oxidation of the undissolved La region. However, except for the 100 h result of the La-H specimen, any La-related peaks are not observed during the measurements. The oxide layer appears to cover the undissolved La regions on the surface over time. These findings suggest that La-rich particles are not formed or ripened near the oxide/gas interface at given experimental conditions.

Secondly, APT analysis was performed to detect La at the oxide grain boundaries. The presence of oxide grain boundaries in the APT sample was ensured using TEM, as illustrated in Figure 4.23. Interestingly, only Ti species were favored to exist at grain boundaries but not La. Considering that the analysis area of APT is too small, this result can not deny the existence or segregation of La at oxide grain boundaries. However, it should be noted that the TEM-EDS analysis also exhibited the same trend. Therefore, it seems reasonable to assume that the effect of La at oxide grain boundaries would not be manifest in this study compared to the other research in which La was clearly observed [116].

Third, the same tendency was observed in the metal/oxide interface. La at the metal/oxide interface was not observed in TEM-EDS results. Even though the highest oxygen affinity of Lanthanum, only Al and Ti internal oxides were observed in the matrix after the 500h oxidation test, as shown in Figure 4.24. Considering that only a small amount of Al and Ti existed in the matrix, as

listed in Table 4.1, the amount of dissolved La in the matrix would be negligible. Therefore, it can be assumed that most of La would be in undissolved La regions, so the high-temperature behavior of the undissolved La regions was discussed in the next section.
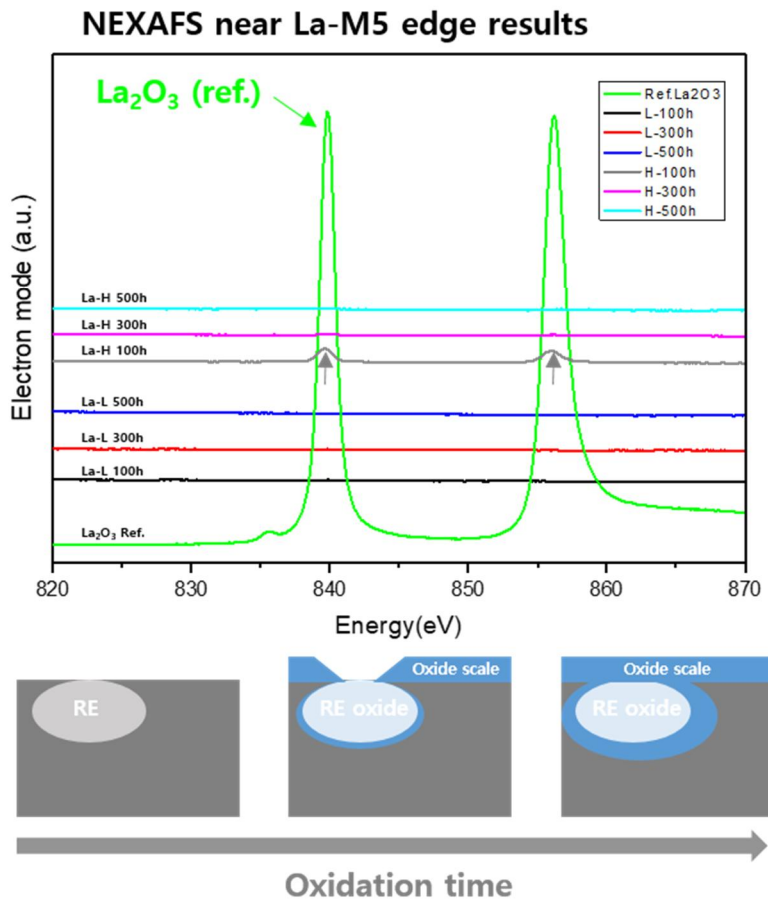
Figure 4.22 NEXAFS results near the La M5-edge (836eV)

Figure 4.23 TEM results to ensure the presence of grain boundaries in the specimen (up) and APT results
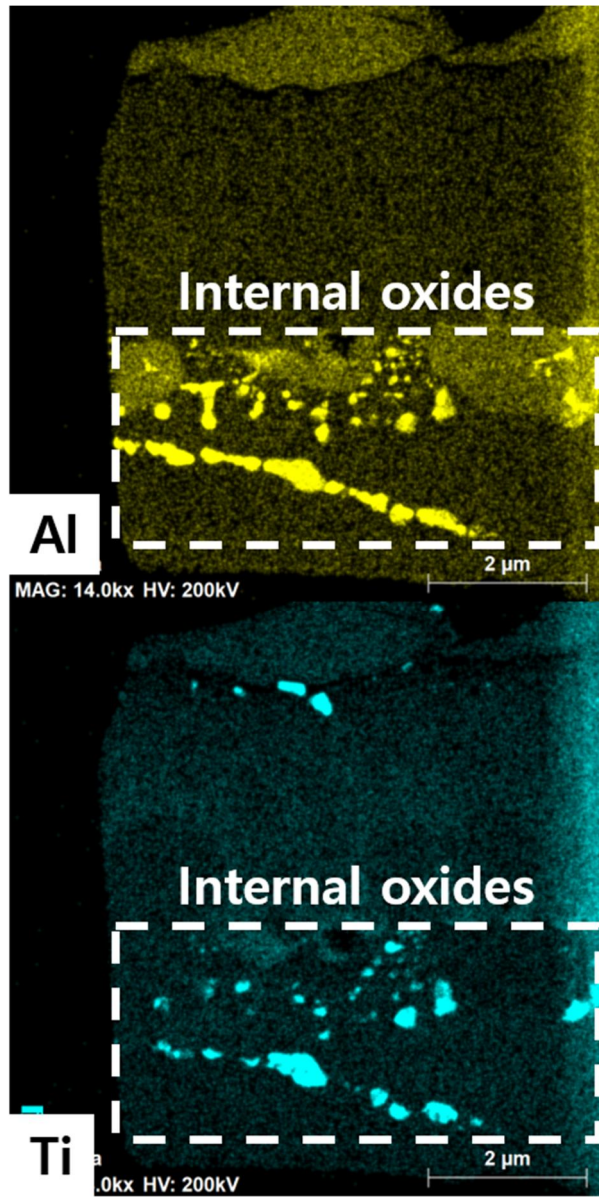
Figure 4.24 TEM EDS results of the internal oxidation zone

of 500h oxidized La-H specimen

4.3 Discussion

4.3.1 High-temperature behavior of undissolved La regions

In contrast to extensive studies on the reactive element effect, the oxidation kinetics of highly La-added alloys were accelerated, especially in the matrix regions. Similarly, J.P. Abellan et al. observed that the weight gain results of 0.71wt% La added alloy were higher than those of 0.12wt% La added alloy. They suggested that the formation of La inclusions during alloy production accelerated the oxidation kinetics of highly La-added alloys [90]. From this perspective, the high-temperature behavior of undissolved La regions was tracked using in-situ experiments under vacuum conditions in the SEM chamber.

As previously mentioned, undissolved La regions consisted of La inclusions and La-Ni intermetallics, and the high-temperature behavior of La inclusions was considered first. The left side of Figure 4.25 exhibits that the change in La inclusions at high temperatures is not apparent during the in-situ experiments. Considering that the oxidation kinetics of highly La-added alloys have already accelerated at the initial oxidation stage, La supplies from La inclusions to the matrix regions seem not to be the main reason for the change in the oxidation behavior. In addition, La diffusion from La inclusions to the Cr_2O_3 scale is expected to be too slow to affect the entire oxide layer. Zhu et al. reported the diffusion coefficients of RE from RE inclusions to

Cr_2O_3 at 800 °C as 1.42 x $10^{-17}m^2/s$ [25]. Assuming that La diffusion is similar to the reported value, the diffusion length of La in Cr_2O_3 would be less than ten micrometers even after 500 h. Therefore, La inclusions can not afford to affect the entire surface within the given oxidation time since the surface fraction of La inclusion is too tiny, as shown in Figure 4.6.

On the contrary, rapid surface diffusion was observed in La-Ni intermetallics regions, as shown on the right side of Figure 4.25. The formation of the liquid phase, predicted by the La-Ni phase diagram in Figure 4.11, seems to accelerate the La diffusion on the surface. In addition, some liquid phase appears to react with the impurity oxygen in the SEM chamber and solidify during the measurements. As a result, the dendrite structure can be observed even at 693 °C. Considering the fast liquid diffusion, the phase transformation of La-Ni intermetallics at a high temperature can be the main reason for the fast oxidation rate of highly La-added alloys.

Therefore, the thermodynamic calculations were conducted to predict the La behavior in La-added alloys at 800 °C, as shown in Figure 4.26. In Figure 4.26, La-M and La-H were simulated as 0.1La-0.5Ni and 0.5La-0.5Ni, respectively. In addition, commercial alloys, like Crofer, were simulated as 0.1La-0Ni to compare the effect of La-Ni intermetallics. Consequently, the liquid phase containing La can only exist when the La and Ni are added to the alloy, like La-M and La-H in this study. This result supports that the liquid phase containing La can accelerate the oxidation kinetics of highly La-added alloys, which will be discussed in the next section.

In contrast, the amount of La in the matrix of 0.1La-0.5Ni and 0.5La-0.5Ni is similar to that of 0.1La-0Ni. This finding suggests that the unusual oxidation behavior of highly La-added alloys compared to commercial alloys is not due to La in the matrix. As a result, the effect of La in the matrix is not considered further in this study.
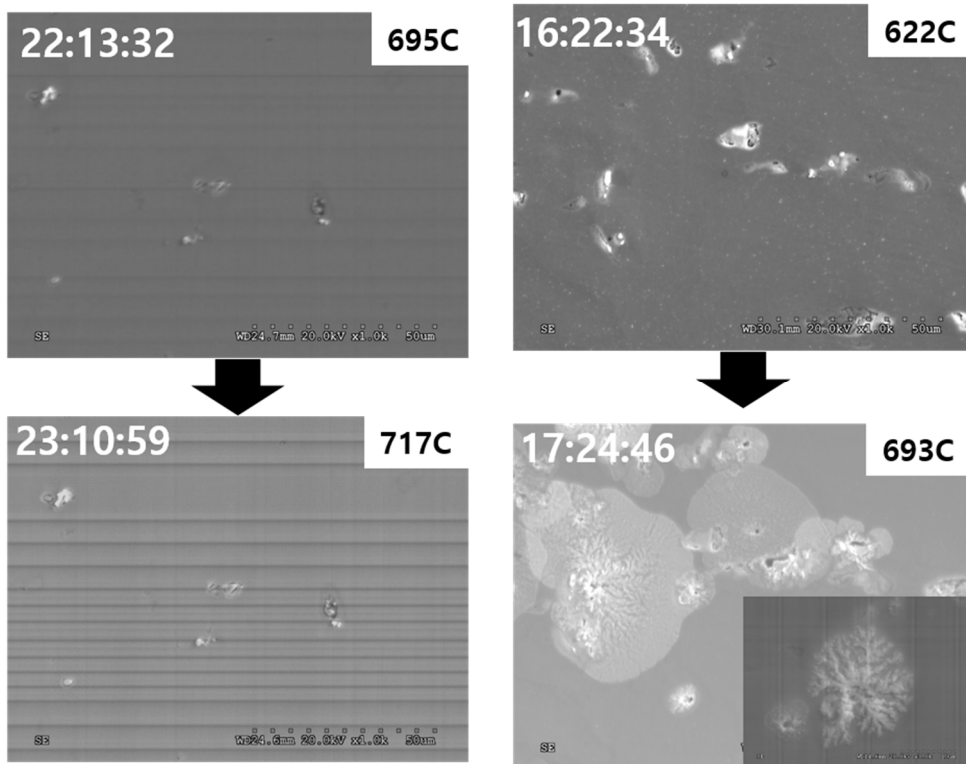
Figure 4.25 High-temperature behavior of La inclusions (left) and La-Ni intermetallics (right) in undissolved La regions
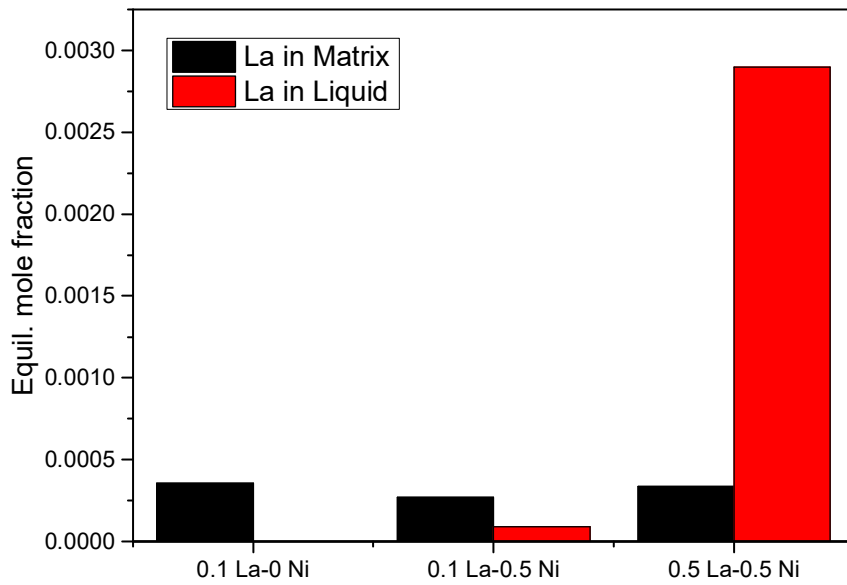
Figure 4.26 Calculated equilibrium mole fraction of La at 800 °C using

the Factsage program

4.3.2 Interface change of highly La-added alloys

The dominant inward oxidation and the convoluted metal/oxide interface were observed in La-M and La-H. However, the two phenomena are not always observed together. For example, the convoluted metal/oxide interface can be formed in Non-RE added alloys, as shown in Figure 4.27 [117]. Therefore, a detailed mechanism of the convoluted interface will be discussed in this section.

Assuming that the diffusion controls the growth of the scale in the oxide scale, the local protrusion of oxides in the matrix would be relieved because the scale thickness of protruded regions was thicker than the stable interface. Sequentially, the convolute interface would be restored to the flat interface. This assumption indicates that other factors should exist to maintain the convoluted interface during the scale growth. Therefore, two possible factors were considered in this section.

100 µm

(a) 650 °C   (b) 750 °C
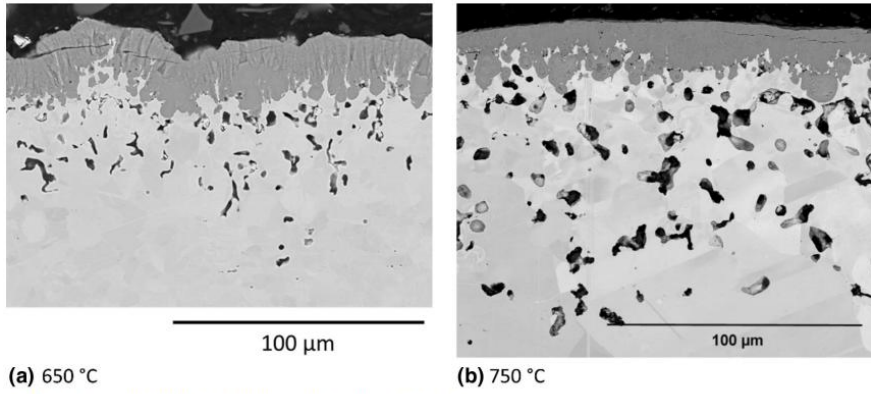
Fig. 4. HEA-2 exposed for 1100 h at (a) 650°C and (b) 750°C in laboratory air.

50 µm

(a) 650 °C   (b) 750 °C
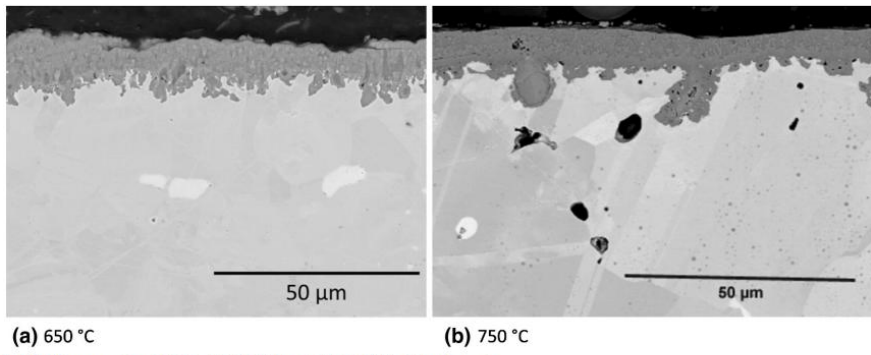
Fig. 5. HEA-3 exposed for 1100 h at (a) 650°C and (b) 750°C in laboratory air.

Figure 4.27 Convoluted interface of Non-RE added specimen (up)

compared to the RE added specimen (down) [117]

Table 4.6 Estimated Cr diffusivity of La added alloys

(m²/s)	$D_{est.}$
La-L	4.34×10^{-16}
La-M	4.54×10^{-16}
La-H	4.20×10^{-16}

First, if the alloy diffusion controls the scale growth, the convoluted interface can be maintained because the above assumptions become the opposite. Therefore, equation 3.9 was applied to the EDS depth profile results, and then the Cr diffusivity of La-added alloys was estimated to determine the La effect on the alloy diffusion. As a result, the estimated Cr diffusivity in Table 4.6 seems to be similar to the reported Cr diffusivity in ferrite [118], and the La addition in the alloy does not affect the Cr diffusion in the alloy. This finding indicates that the convoluted interface of high La-added alloys is not due to alloy diffusion.

Second, if the transport of oxidants is promoted at specific regions, like alloy grain boundaries, this can promote the local irregularity of the interface. Cross-sectional results in Figure 4.28 can support this assumption. The oxygen penetration depth along the alloy grain boundaries was approximately 20 μm which is ten times larger than the oxide thickness. Moreover, La was detected along the alloy grain boundaries of the oxidized La-H specimen, as shown in Figure 4.28. It should be emphasized that only La-M and La-H, in which the liquid La can be formed due to the low melting temperature of La-Ni intermetallics, showed these tendencies. The liquid phase containing La appears to diffuse through alloy grain boundaries and promote inward oxidation. Therefore, highly La-added specimens can have a thick oxide scale.
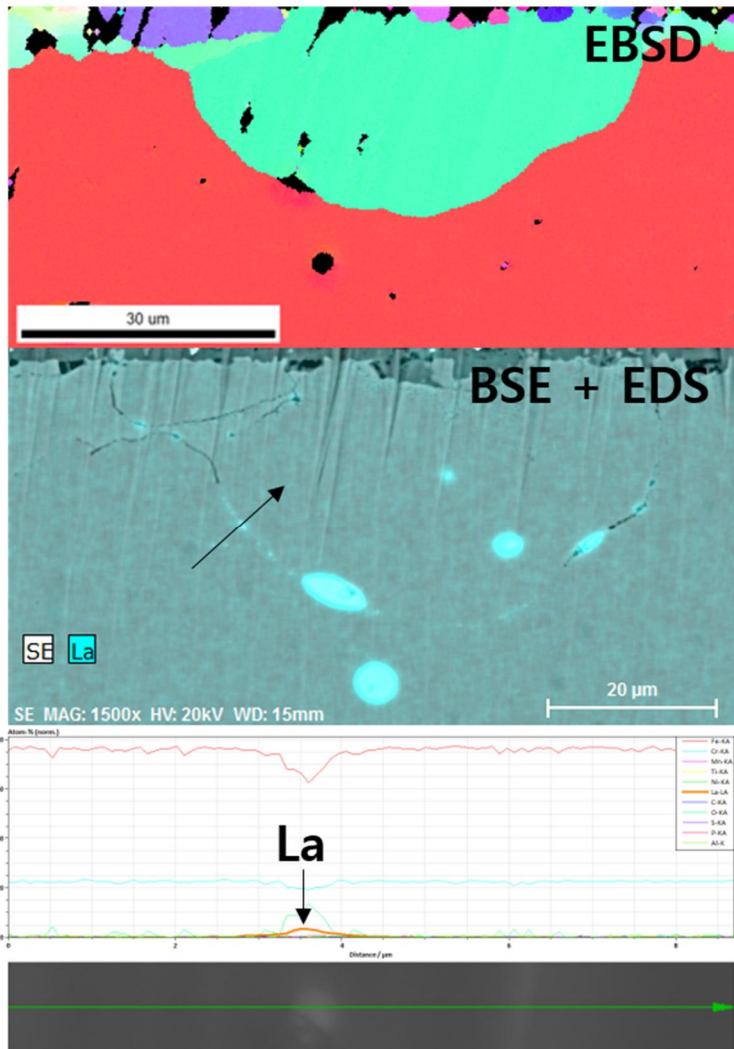
Figure 4.28 Existence of La at alloy grain boundaries combined with EDS and EBSD results

The above findings indicate that the alloy grain boundaries can promote La diffusion, which can affect the oxide/metal interface. Therefore, oxidation tests of surface-treated specimens were conducted to consider the alloy grain boundary effect, as shown in Figure 4.29. After the 400h oxidation test, similar oxidation behavior was observed between the annealed and hot-rolled La-M specimens, of which the surface was treated by mechanical polishing. This result indicates that the dislocation density of the bulk matrix can not change the interface. However, the electro-polished specimen exhibits a thin and flat surface compared to the mechanically polished specimens. Since the surface crystallization during the oxidation test, as shown in Figure 4.16, would occur only in the mechanically polished specimens, the grain boundary fractions on the surface appear to affect the interface. As the grain boundary faction increases on the surface, La diffusion along grain boundaries can be promoted, and the thick oxide scale with a convoluted interface appears to be formed.

#1 AS + Mechanical-polishing
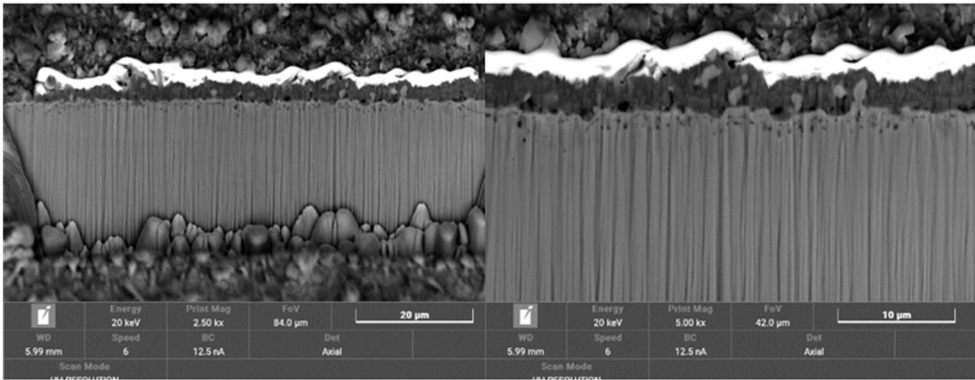
#2 AS + Electro-polishing
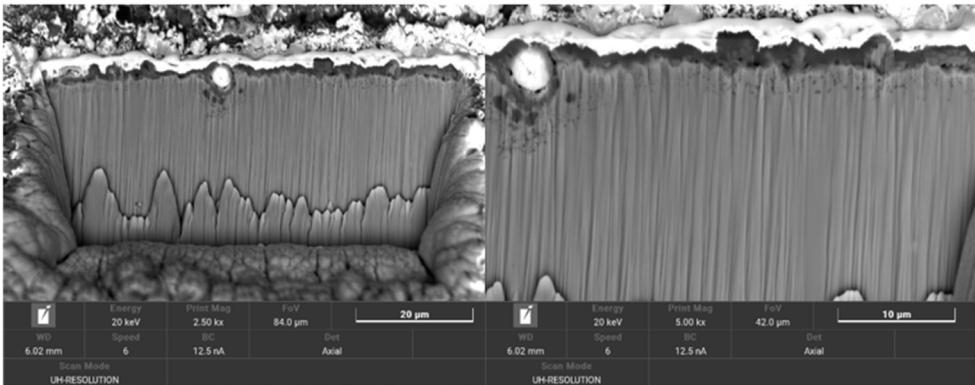
#3 300h annealing + Mechanical-polishing
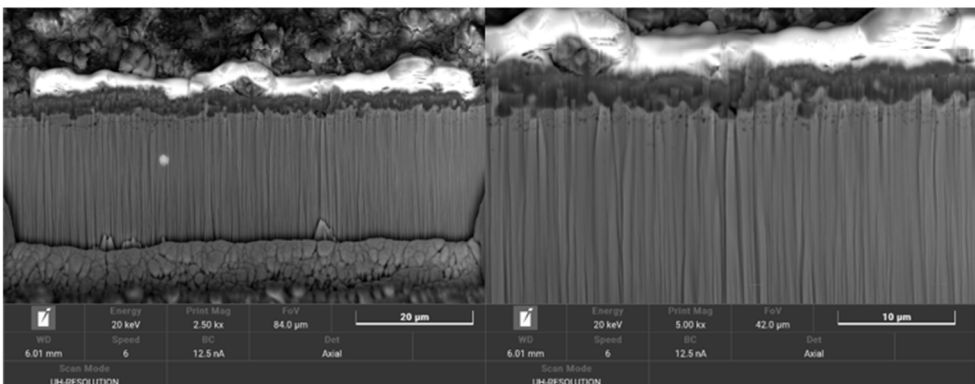
Figure 4.29 Surface-treated specimens after oxidation tests

4.3.3 Interface effect on the ASR property of La-added alloys

Numerous researchers have reported that the addition of reactive elements improves the adhesion of the oxide scale [25, 119-124]. The formation of oxide pegs due to the convoluted interface has been considered the main factor [120, 121, 124] because it can prevent crack propagation at the interface and suppress the spallation. Mass gain results in Figure 4.13 appears to support this explanation. After the 400 h oxidation test, a slight mass gain decrease was observed in the La-L specimen with a flat interface but not in the La-M or La-H with a convoluted interface. This finding indicates that the adhesion with the convoluted interface is sufficient to prevent the oxide scale detachment during the oxidation test.

Numerous cross-sectional BSE analyses revealed that the adhesion difference due to interface change appears to affect the formation of voids in La-added alloys. For statistical comparison, trainable machine learning methods were applied since conventional threshold methods had many limitations in segmenting voids because of the complexity of the images. Seven BSE images of each specimen, optimized as data set to minimize the overfitting problem of the machine learning process, were trained to make strong classifiers for the void segmentation. As a result, BSE images are successfully converted into binary images related to voids, as shown in Figure 4.30. (White indicates the formation of voids, and the background is colored

black). Figure 4.30 reveals that voids were observed at the Cr_2O_3/Cr_2MnO_4 interface for the La-M and La-H specimens, similar to the duplex chromia growth in pure chromium [125]. During the oxidation of pure chromium, the inward growth of the n-type chromia can be possible at the internal interface due to the low oxygen partial pressure, and the outward growth of p-type chromia can be dominant on the external scale. The vacancy diffusion of each case is illustrated in Figure 4.31. Therefore, oxygen and Cr vacancies can agglomerate at the interface between n-type and p-type chromia, and voids can be formed. Likewise, the void formation at the Cr_2O_3/Cr_2MnO_4 interface was considered, as illustrated in Figure 4.32. Considering the n-type growth of chromia below the $MnCr_2O_4$ layer [126], oxygen vacancies would diffuse to Cr_2O_3/Cr_2MnO_4 interface, and the outward growth of the Cr_2MnO_4 layer has already been reported. Therefore, it can be concluded that the formation of voids would be favorable at the Cr_2O_3/Cr_2MnO_4 interface, and the results of La-M and La-H appear to support it.
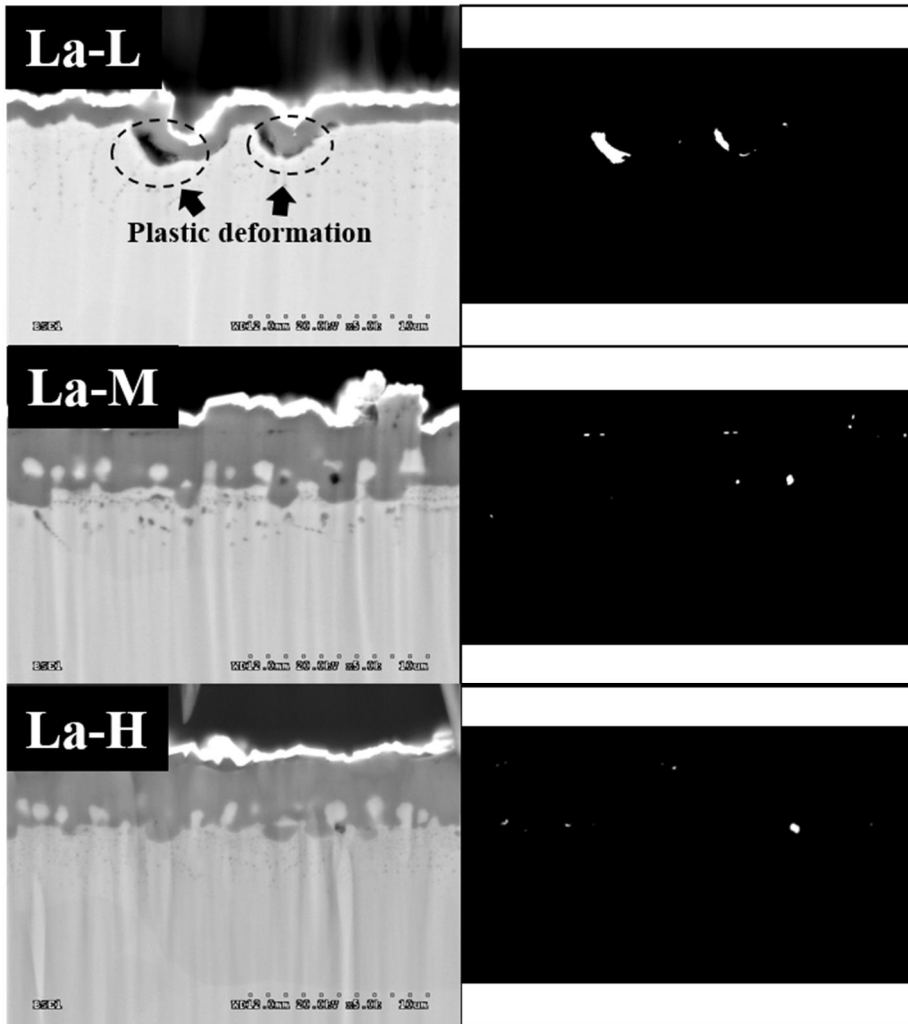
Figure 4.30 Classified voids from the cross-sectional BSE images
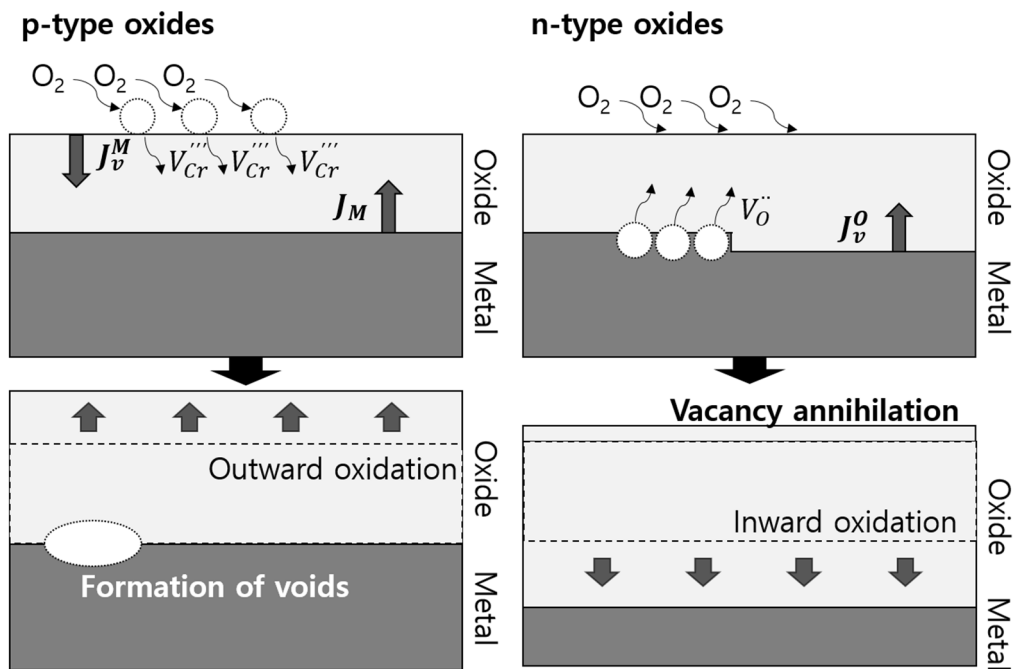
Figure 4.31 Void formation mechanism of p-type oxides (left)

and n-type oxides (right)
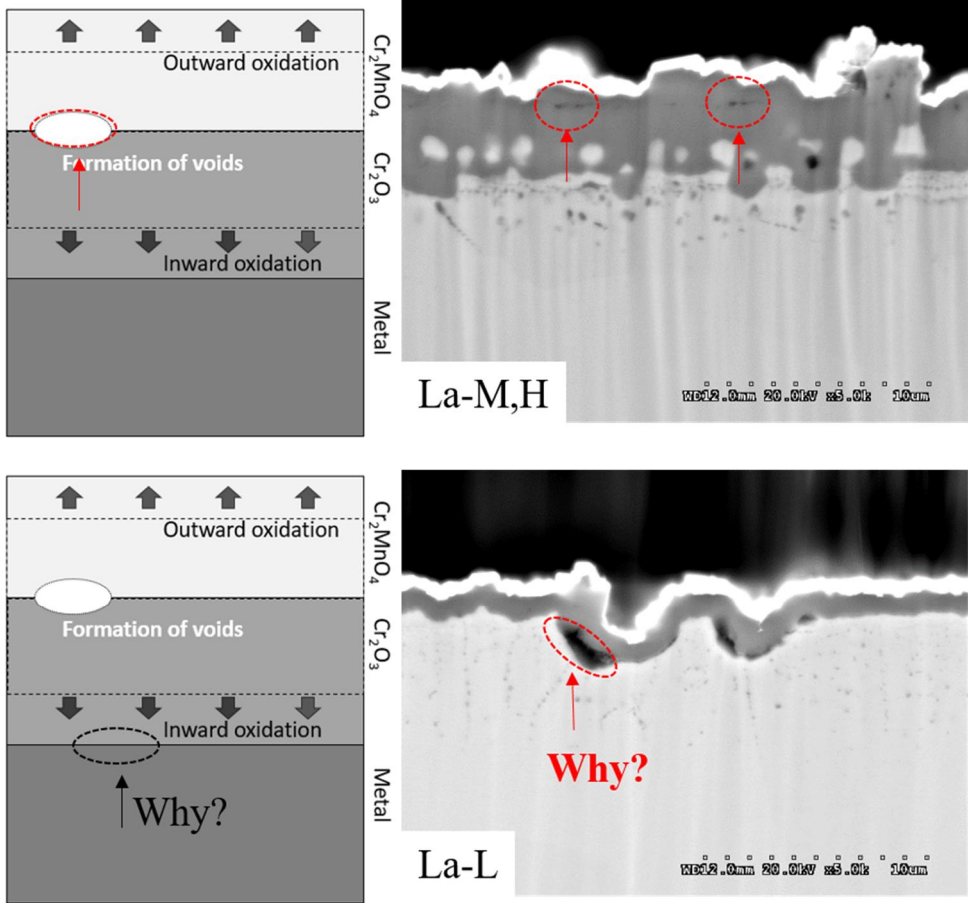
Figure 4.32 Different locations of voids of La added alloys

However, in La-L, voids were mainly observed at the oxide/metal interface. This result indicates that not the agglomeration of vacancies during the oxidation but another factor controls the void formation of La-L. Thermally-induced stress can be the reason for the void formation because of different coefficients of thermal expansion between the matrix and oxides. During the ex-situ measurements, specimens were heated in the furnace, cooled in the air, and then reheated. In the meanwhile, thermal stress was inevitably imposed on the specimens. If the stress exceeds the elastic region of the specimen, the alloy deformation appears to relieve some imposed stress, as already observed in La-L of Figure 4.30. However, La-L can not prevent the detachment of the oxide scale. Considering that the plasticity of Cr_2O_3 is not affected by the reactive element [127], La-L with a flat interface appears to have weaker adhesion than La-M and La-H with a convoluted interface.

Moreover, the void distribution result, which is obtained by the particle analysis tool in the ImageJ program, revealed that the larger voids tend to be formed in the La-L, as shown in Figure 4.33. Also, linear pixel density corresponding to voids in La-L is six times higher than that in La-M and La-H, as listed in Table 4.7. Therefore, it can be concluded that the La-L with a flat interface has larger and more voids due to the weak adhesion of the oxide/metal interface.
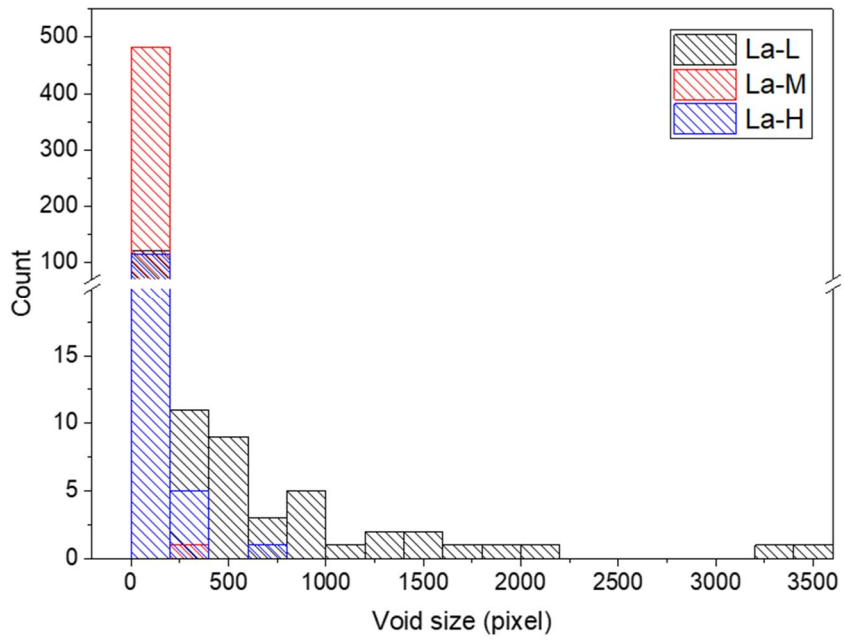
Figure 4.33 Void distribution of La added alloys

Table 4.7 Linear pixel density and average pore radius

	Linear pixel density (pixels/µm)	Average pore radius (nm)
La-L	72.862	342.47
La-M	12.854	93.34
La-H	13.452	155.29

The higher fraction of the voids in La-L, which can degrade the electrical conductivity of composites [128], appears to degrade the ASR properties. As stated above, La-L exhibits the worst ASR results despite the thinnest oxide scale. Therefore, estimated ASR results were compared with the measured ASR results to consider the effect of the void on the ASR, as shown in Figure 4.34. Although it would be a limitation to determine the exact resistivity values of each oxide, the ASR can be estimated by equation 4.4 using the resistivity of pure oxides in Table 4.4 and the calculated thickness of each layer in Figure 4.16. (For the simple calculation, the phase fraction of the oxide layer was assumed to maintain during the oxidation test.)

Interestingly, Figure 4.34 exhibits that the estimated values match well with the measured ASR of La-M and La-H but not that of La-L. The measured ASR of La-L is too high compared to the estimated values. This finding can support that the measured voids in this study can degrade the ASR results, especially in La-L. However, if a sufficient amount of La is added to the alloy containing nickel, a convoluted interface can be formed, which enhances the adhesion of the oxide scale and prevents the degradation of ASR due to voids.
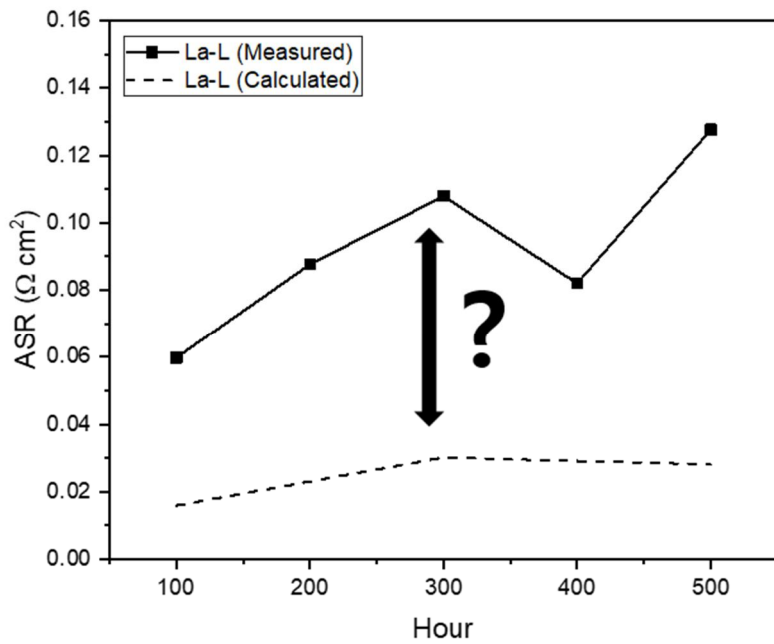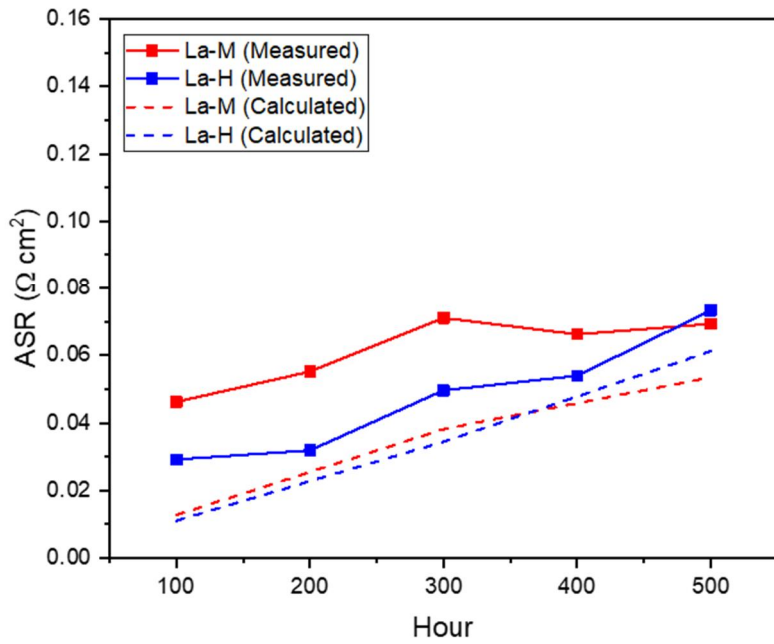
Figure 4.34 Estimated (dashed line) and measured (solid line) ASR results

Chapter 5. Summary and Conclusion

Effect of alloy grain boundary fraction on the oxidation behavior on the oxidation behavior of Nickel-based superalloy

In Haynes 282, oxy-fuel combustion conditions with an increased oxygen partial pressure accelerated the oxidation kinetics more than the air combustion conditions. A deformed microstructure or a high fraction of HAGBs in the matrix seems to provide a fast chromium diffusion path for oxidation; thus, an increase in mass gain was observed at the initial stage. However, the slowed formation of the Cr-depleted zone was only observed in the specimen with the smallest grain size. Furthermore, a sufficient chromium supply derived from the high fraction of HAGBs in the matrix suppresses Cr depletion. Therefore, Ti supply to the oxide, known to increase the concentration of Cr vacancies when dissolved in Cr_2O_3, was suppressed. Finally, a small-grained specimen exhibited superior oxidation resistance at the later oxidation stage. Thus, this study shows the possibility of improving oxidation resistance by controlling the microstructure of the alloy.

Effect of alloy/oxide interface on the Area Specific Resistance and oxidation behavior of La-added alloys

To ensure the La effects on the ASR property, ferritic stainless steels for SOFCs interconnects are prepared with various La contents. Because of the low solubility and high reactivity, undissolved La regions were observed in the initial microstructure of alloys. The oxide scale growth was accelerated as the La contents increased, and severe inward oxidation was observed in highly La-added specimens.

However, the lowest lanthanum specimen had the worst ASR property, despite the thinnest oxide scale. Using TEM and X-ray absorption fine structure spectroscopy, it has been shown that the electrical properties of oxide scales were not much affected by the La addition. Instead, the trainable machine learning method was shown that the formation of voids was more promoted in the La-L specimen. This finding indicates that the formation of voids is crucial to degrade the ASR property of SOFC interconnects. The weak adhesion due to the flat interface in the La-L specimen seems unable to relieve the imposed thermal stress. As a result, the detachment of the oxide scale was only observed in the La-L specimen, and it degraded the ASR property.

On the contrary, if the amount of La in the alloy containing nickel is

sufficient, the diffusion of the La liquid phase along alloy grain boundaries could promote a convoluted oxide/metal interface, enhancing the oxide/scale adhesion. As a result, the formation of voids in La-M and La-H is suppressed compared to in La-L and is mainly observed not at the oxide/metal interface but at Cr_2O_3/Cr_2MnO_4 interface. Consequently, high La addition in the alloy containing nickel prevents the degradation of ASR properties since the convoluted interface improves the adhesion of the oxide scale.

Original contribution

The findings in this thesis address the two important microstructure effects on the oxidation behavior of heat-resistant alloys; the effect of alloy grain boundaries and the effect of oxide/metal interface.

In the first part of this thesis, the author suggested that reducing grain size would be a reasonable strategy to improve the oxidation resistance of Haynes 282 in oxy-fuel combustion conditions. It was well known that the alloy grain boundaries promoted the selective oxidation of Cr at the initial stage, and the formation of the Cr depletion zone degraded the steady-stage growth of the Cr_2O_3 scale. However, the direct relation between the alloy grain boundaries and the formation of the Cr depletion zone, mainly in Haynes 282, was not discussed. The author revealed that the high fraction of alloy grain boundaries could supply enough Cr to the metal/oxide interface and sustain stable growth of the Cr_2O_3 scale. The sufficient Cr supply suppressed the formation of the Cr depletion zone and decreased a Ti diffusion to the oxide scale, which would degrade the oxidation resistance of alloys.

In the second part, the author found that the high La addition (0.11~0.6 wt.%) to SOFC interconnects improved the ASR properties due to the good adhesion between the oxides and La-added alloys. The commercial alloys tend to limit the amount of La addition to 0.11wt.%, so the oxidation mechanism of highly

La-added steels (0.11~0.6 wt.%) was not fully understood. The author found that the high La addition accelerated the oxidation kinetics, especially the inward oxidation of the Cr_2O_3 layer, even at the initial oxidation stage. This severe inward oxidation results in the formation of oxide pegs and improves the adhesion of the oxide scale.

However, numerous experimental results demonstrated that La did not exist in the oxide scale and oxide/gas interface. This finding indicates that the conventional dynamic segregation model can not explain the oxidation behavior of La-added alloys. Therefore, the author suggested new assumptions based on the undissolved La regions. Because of the low solubility of La in the matrix, the undissolved La regions were observed in highly La-added alloys. The author proved that the undissolved La regions consisted of La inclusions (which contain O, P, S) and La-Ni intermetallics and then demonstrated the high-temperature behavior of each region.

The in-situ heating experiments in SEM revealed that the La inclusions were not enough to affect the entire surface region because of the slow diffusion rate. In contrast, fast surface diffusion of La-Ni intermetallic was observed because of the liquid phase of La-Ni intermetallic at high temperatures. Furthermore, the alloy grain boundaries enable the promotion of this La diffusion because the surface recrystallized specimen had more oxide pegs than those of the non-recrystallized specimen. Based on these findings, the author successfully controlled the oxide/metal interface of highly La-added alloys for SOFC interconnects.

It is the early study of developing highly La-added alloys for SOFC interconnects, so further studies will be required. First, the undissolved La regions in this thesis contain only La inclusions and La-Ni intermetallics, but the various kinds of La phases can be suggested depending on the SOFC operation conditions. Second, the results of this thesis were obtained from hot-rolled specimens with a polished surface, so the effect of various surface treatments and microstructures can be considered. Third, a better understanding of the other minor element's effects (like Boron) could help to design La-added alloys with better mechanical properties.

Bibliography

[1] F. Abe, Research and development of heat-resistant materials for advanced USC power plants with steam temperatures of 700 C and above, Engineering (Beijing), 1 (2015) 211-224.

[2] Y. Yuan, Z. Zhong, Z. Yu, H. Yin, Y. Dang, X. Zhao, Z. Yang, J. Lu, J. Yan, Y. Gu, Microstructural evolution and compressive deformation of a new Ni-Fe base superalloy after long term thermal exposure at 700° C, Mater. Sci. Eng. A, 619 (2014) 364-369.

[3] M. Tabuchi, H. Hongo, F. Abe, Creep strength of dissimilar welded joints using high B-9Cr steel for advanced USC boiler, Metall Mater Trans A, 45 (2014) 5068-5075.

[4] H. Semba, H. Okada, T. Hamaguchi, S. Ishikawa, M. Yoshizawa, Development of boiler tubes and pipes for advanced USC power plants, Nippon Steel Sumitomo Metals Technical Report Is, 397 (2013) 71-77.

[5] P.S. Weitzel, Steam generator for advanced ultra supercritical power plants 700C to 760C, in: ASME 2011 Power Conference collocated with JSME ICOPE 2011, American Society of Mechanical Engineers, 2011, pp. 281-291.

[6] J. Wheeldon, Engineering and Economic Evaluation of 1300 F Series Ultra-Supercritical Pulverized Coal Power Plants: Phase 1, EPRI, Palo Alto, CA, 1015699 (2008).

[7] M. Igarashi, H. Semba, M. Yonemura, T. Hamaguchi, H. Okada, M. Yoshizawa, A. Iseda, Advanced in materials technology for A-USC power plant boilers, in: Igarashi, H. Semba, M. Yonemura, T. Hamaguchi, H. Okada, M. Yoshizawa, A. Iseda//Advances in Materials Technology for Fossil Power Plants: Proceedings from the 6th International Conference.–Santa Fe, USA, 2011, pp. 72-85.

[8] R. Stanger, T. Wall, R. Spörl, M. Paneru, S. Grathwohl, M. Weidmann, G. Scheffknecht, D. McDonald, K. Myöhänen, J. Ritvanen, S. Rahiala, T. Hyppänen, J. Mletzko, A. Kather, S. Santos, Oxyfuel combustion for CO2 capture in power plants, International Journal of Greenhouse Gas Control, 40 (2015) 55-125.

[9] F. Sun, Y. Gu, J. Yan, Z. Zhong, M. Yuyama, Phenomenological and microstructural analysis of intermediate temperatures creep in a Ni-Fe-based alloy for advanced ultra-supercritical fossil power plants, Acta Materialia, 102 (2016) 70-78.

[10] A. Jena, M. Chaturvedi, The role of alloying elements in the design of nickel-base superalloys, J MATER SCI, 19 (1984) 3121-3139.

[11] C. Joseph, C. Persson, M.H. Colliander, Influence of heat treatment on the microstructure and tensile properties of Ni-base superalloy Haynes 282, Mater. Sci. Eng. A, 679 (2017) 520-530.

[12] P.D. Jablonski, J.A. Hawk, C.J. Cowen, P.J. Maziasz, Processing of advanced cast alloys for A-USC steam turbine applications, JOM, 64 (2012)

271-279.

[13] M. Pandey, D. Satyanarayana, Effect of gamma prime depletion on creep behaviour of a nickel base superalloy (Inconel alloy X-750), Bulletin of Materials Science, 19 (1996) 1009-1015.

[14] X. Yang, S. Li, H. Qi, Effect of high-temperature hot corrosion on the low cycle fatigue behavior of a directionally solidified nickel-base superalloy, Int J Fatigue, 70 (2015) 106-113.

[15] V. Vasantasree, M. Hocking, Hot corrosion of Ni☐ Cr alloys in SO2+ O2 atmospheres—I. Corrosion kinetics, Corros Sci, 16 (1976) 261-277.

[16] J.-H. Kim, D.-I. Kim, S. Suwas, E. Fleury, K.-W. Yi, Grain-Size Effects on the High-Temperature Oxidation of Modified 304 Austenitic Stainless Steel, Oxid. Met., 79 (2012) 239-247.

[17] J.-H. Kim, B.K. Kim, D.-I. Kim, P.-P. Choi, D. Raabe, K.-W. Yi, The role of grain boundaries in the initial oxidation behavior of austenitic stainless steel containing alloyed Cu at 700℃ for advanced thermal power plant applications, Corros. Sci., 96 (2015) 52-66.

[18] Z. Liang, P.M. Singh, Q. Zhao, Y. Wang, High Temperature Oxidation of Newly Developed Alloy 282 in the Flowing-Air and Steam Condition at 900-1100 °C, Oxid. Met., 84 (2015) 291-305.

[19] F. Pérez-González, N. Garza-Montes-de Oca, R. Colás, High temperature oxidation of the Haynes 282© nickel-based superalloy, Oxid. Met., 82 (2014) 145-161.

[20] Z. Yang, Recent advances in metallic interconnects for solid oxide fuel cells, Int. Mater. Rev., 53 (2008) 39-54.

[21] L. Chen, Z. Yang, B. Jha, G. Xia, J.W. Stevenson, Clad metals, roll bonding and their applications for SOFC interconnects, Journal of Power Sources, 152 (2005) 40-45.

[22] J.W. Fergus, Metallic interconnects for solid oxide fuel cells, Materials Science and Engineering: A, 397 (2005) 271-283.

[23] N.Q. Minh, T. Takahashi, Science and technology of ceramic fuel cells, Elsevier, 1995.

[24] D. Bastidas, High temperature corrosion of metallic interconnects in solid oxide fuel cells, Revista de metalurgia, 42 (2006) 425-443.

[25] J. Zhu, L.M. Fernández Díaz, G.R. Holcomb, P.D. Jablonski, C.J. Cowen, D.E. Alman, D.E. Laughlin, S. Sridhar, An Electron Microscopy Investigation of the Transient Stage Oxidation Products in an Fe-22Cr Alloy with Ce and La Additions Exposed to Dry Air at 1073 K (800 °C), Metallurgical and Materials Transactions A, 42 (2010) 121-137.

[26] G.J. Yurek, K. Przybylski, A. Garratt-Reed, Segregation of Y to Grain Boundaries in Cr2 O 3 and NiO Scales Formed on an ODS Alloy, Journal of the Electrochemical Society, 134 (1987) 2643-2644.

[27] K. Przybylski, A. Garratt-Reed, G.J. Yurek, Grain boundary segregation of yttrium in chromia scales, Journal of the Electrochemical Society, 135 (1988) 509-517.

[28] B. Pint, Experimental observations in support of the dynamic-segregation theory to explain the reactive-element effect, Oxid. Met., 45 (1996) 1-37.

[29] J. Froitzheim, G.H. Meier, L. Niewolak, P.J. Ennis, H. Hattendorf, L.

Singheiser, W.J. Quadakkers, Development of high strength ferritic steel for interconnect application in SOFCs, Journal of Power Sources, 178 (2008) 163-173.

[30] R. Sachitanand, M. Sattari, J.-E. Svensson, J. Froitzheim, Evaluation of the oxidation and Cr evaporation properties of selected FeCr alloys used as SOFC interconnects, international journal of hydrogen energy, 38 (2013) 15328-15334.

[31] S. Swaminathan, Y.-S. Lee, D.-I. Kim, Long term high temperature oxidation characteristics of La and Cu alloyed ferritic stainless steels for solid oxide fuel cell interconnects, Journal of Power Sources, 327 (2016) 104-118.

[32] S. Swaminathan, Y.S. Lee, D.-I. Kim, Effects of alloyed La, Cu and B on the oxidation of Fe-22Cr ferritic stainless steels under simulated cathode side atmosphere of solid oxide fuel cell interconnects, Corros. Sci., 133 (2018) 150-164.

[33] S. Swaminathan, Y.S. Ko, Y.-S. Lee, D.-I. Kim, Oxidation behavior and area specific resistance of La, Cu and B alloyed Fe-22Cr ferritic steels for solid oxide fuel cell interconnects, Journal of Power Sources, 369 (2017) 13-26.

[34] M.R. Ardigo, I. Popa, S. Chevalier, V. Parry, A. Galerie, P. Girardon, F. Perry, R. Laucournet, A. Brevet, E. Rigal, Coated interconnects development for high temperature water vapour electrolysis: Study in anode atmosphere, International Journal of Hydrogen Energy, 38 (2013) 15910-15916.

[35] K.O. Hoyt, P.E. Gannon, P. White, R. Tortop, B.J. Ellingwood, H. Khoshuei, Oxidation behavior of (Co,Mn)3O4 coatings on preoxidized stainless steel for solid oxide fuel cell interconnects, International Journal of Hydrogen Energy, 37 (2012) 518-529.

[36] Z. Yang, G.-G. Xia, C.-M. Wang, Z. Nie, J. Templeton, J.W. Stevenson, P. Singh, Investigation of iron–chromium–niobium–titanium ferritic stainless steel for solid oxide fuel cell interconnect applications, Journal of Power Sources, 183 (2008) 660-667.

[37] P. Huczkowski, L. Singheiser, Effect of geometry and composition of Cr steels on oxide scale properties relevant for interconnector applications in Solid Oxide Fuel Cells (SOFCs), in, Aachen, Publikationsserver der RWTH Aachen University, 2005.

[38] J.G. Grolig, J. Froitzheim, J.-E. Svensson, Coated stainless steel 441 as interconnect material for solid oxide fuel cells: Evolution of electrical properties, Journal of Power Sources, 284 (2015) 321-327.

[39] Q. Jiang, D. Lu, C. Liu, N. Liu, B. Hou, The Pilling-Bedworth ratio of oxides formed from the precipitated phases in magnesium alloys, Frontiers in Materials, (2021) 457.

[40] D.J. Young, High temperature oxidation and corrosion of metals, Elsevier, 2008.

[41] X. Liu, C. Bonifacio, J.C. Yang, P. Ercius, B. Gleeson, Effect of environmental sulfur on the structure of alumina scales formed on Ni-base alloys, Acta Mater, 97 (2015) 41-49.

[42] J. Lu, Z. Yang, Y. Li, J. Huang, Y. Zhou, X. Zhao, Y. Yuan, Fireside Corrosion Behaviors of Super304H and HR3C in Coal Ash/Gas Environment with Different SO 2 Contents at 650° C, J Mater Eng Perform, 27 (2018) 2855-

2862.

[43] N. Tsuji, Y. Ito, Y. Saito, Y. Minamino, Strength and ductility of ultrafine grained aluminum and iron produced by ARB and annealing, Scr. Mater., 47 (2002) 893-899.

[44] H. Li, E. Hsu, J. Szpunar, H. Utsunomiya, T. Sakai, Deformation mechanism and texture and microstructure evolution during high-speed rolling of AZ31B Mg sheets, J MATER SCI, 43 (2008) 7148-7156.

[45] L. Saraf, Kernel average misorientation confidence index correlation from FIB sliced Ni-Fe-Cr alloy surface, Microsc. Microanal., 17 (2011) 424-425.

[46] M. Calcagnotto, D. Ponge, E. Demir, D. Raabe, Orientation gradients and geometrically necessary dislocations in ultrafine grained dual-phase steels studied by 2D and 3D EBSD, Mater. Sci. Eng. A, 527 (2010) 2738-2746.

[47] A. Ramazani, S. Bruehl, T. Gerber, W. Bleck, U. Prahl, Quantification of bake hardening effect in DP600 and TRIP700 steels, Mater Des, 57 (2014) 479-486.

[48] S. Liu, X. Li, H. Guo, C. Shang, R. Misra, Isolating contribution of individual phases during deformation of high strength-high toughness multi-phase pipeline steel, Mater. Sci. Eng. A, 639 (2015) 131-135.

[49] M. Phaniraj, D.-I. Kim, Y.W. Cho, Effect of grain boundary characteristics on the oxidation behavior of ferritic stainless steel, Corros Sci, 53 (2011) 4124-4130.

[50] P. Kofstad, High temperature oxidation of metals, 1966.

[51] F. Abe, H. Araki, H. Yoshida, M. Okada, The role of aluminum and titanium on the oxidation process of a nickel-base superalloy in steam at 800° C, Oxid. Met., 27 (1987) 21-36.

[52] M. Abbasi, D.-I. Kim, J.-H. Shim, W.-S. Jung, Effects of alloyed aluminum and titanium on the oxidation behavior of INCONEL 740 superalloy, J Alloys Compd, 658 (2016) 210-221.

[53] S. Chen, L. Rong, Roles of Mn in the High-Temperature Air Oxidation of 9Cr Ferritic-Martensitic Steel After Severe Plastic Deformation, Oxid. Met., 89 (2018) 415-428.

[54] L. Cooper, S. Benhaddad, A. Wood, D. Ivey, The effect of surface treatment on the oxidation of ferritic stainless steels used for solid oxide fuel cell interconnects, J Power Sources, 184 (2008) 220-228.

[55] H.J. Grabke, Z. Tökei, C. Ostwald, Initial Oxidation of a 9% CrMo-and a 12% CrMoV-Steel, Steel Res. Int., 75 (2004) 38-46.

[56] L. Xingeng, H. Jiawen, Effect of shot blasting on oxidation behavior of TP304H steel at 610-770° C in water vapor, Mater. Lett., 60 (2006) 339-344.

[57] J. Yuan, X. Wu, W. Wang, S. Zhu, F. Wang, The effect of surface finish on the scaling behavior of stainless steel in steam and supercritical water, Oxid. Met., 79 (2013) 541-551.

[58] Y. Zengwu, F. Min, W. Xuegang, L. Xingeng, Effect of shot peening on the oxidation resistance of TP304H and HR3C steels in water vapor, Oxid. Met., 77 (2012) 17-26.

[59] J. Langevoort, T. Fransen, P. Gellings, On the influence of cold work on the oxidation of some stainless steels, Werkst Korros, 34 (1983) 500-504.

[60] C. Ostwald, H.J. Grabke, Initial oxidation and chromium diffusion. I.

Effects of surface working on 9-20% Cr steels, Corros Sci, 46 (2004) 1113-1127.

[61] M. Abbasi, B.-K. Kim, D.-I. Kim, W.-S. Jung, Effects of surface deformation on the oxidation behavior of INCONEL 740 superalloy in humid air, J Alloys Compd, 683 (2016) 212-220.

[62] Y. Wang, Q. Zhao, Z. Liang, H. Ma, H. Chen, W. Jiang, Analysis on high-temperature corrosion characteristic of 0Cr18Ni9NbCu3BN steel, Mater. Res. Innov, 19 (2015) S1-104-S101-108.

[63] N. Otsuka, Fireside corrosion of austenitic tube materials for advanced USC boilers, in: Mater. Sci. Forum, Trans Tech Publ, 2011, pp. 206-211.

[64] P. Kofstad, G. Åkesson, Sulfate-induced high-temperature corrosion of nickel, Oxid. Met., 14 (1980) 301-323.

[65] K.P. Lillerud, P. Kofstad, Sulfate-induced hot corrosion of nickel, Oxid. Met., 21 (1984) 233-270.

[66] X. Liu, Effects of trace SO2 and Na2SO4 deposit on the reaction behavior of Al2O3-scale forming alloys, in, University of Pittsburgh, 2014.

[67] E. Schmucker, C. Petitjean, L. Martinelli, P.-J. Panteix, S. Ben Lagha, M. Vilasi, Oxidation of Ni-Cr alloy at intermediate oxygen pressures. I. Diffusion mechanisms through the oxide layer, Corros Sci, 111 (2016) 474-485.

[68] S. Tsai, A.a. Huntz, C. Dolin, Diffusion of 18 O in massive Cr 2 O 3 and in Cr 2 O 3 scales at 900° C and its relation to the oxidation kinetics of chromia forming alloys, Oxid. Met., 43 (1995) 581-596.

[69] S.C. Tsai, A.M. Huntz, C. Dolin, Growth mechanism of Cr2O3 scales: oxygen and chromium diffusion, oxidation kinetics and effect of yttrium, Mater. Sci. Eng. A, 212 (1996) 6-13.

[70] D. Caplan, G. Sproule, Effect of oxide grain structure on the high-temperature oxidation of Cr, Oxid. Met., 9 (1975) 459-472.

[71] A. Col, V. Parry, C. Pascal, Oxidation of a Fe-18Cr-8Ni austenitic stainless steel at 850° C in O2: Microstructure evolution during breakaway oxidation, Corros Sci, 114 (2017) 17-27.

[72] C. Wagner, Theoretical analysis of the diffusion processes determining the oxidation rate of alloys, J Electrochem Soc, 99 (1952) 369.

[73] Y. Xie, J. Zhang, D.J. Young, Temperature effect on oxidation behavior of Ni-Cr alloys in CO2 gas atmosphere, J Electrochem Soc, 164 (2017) C285-C293.

[74] T. Gheno, F. Jomard, C. Desgranges, L. Martinelli, Tracer diffusion of Cr in Ni and Ni-22Cr studied by SIMS, Materialia, 3 (2018) 145-152.

[75] H. Evans, R. Lobb, Alloy depletion profiles during non-protective oxidation, Corros Sci, 24 (1984) 223-233.

[76] J. Čermák, Grain boundary self-diffusion of 51Cr and 59Fe in austenitic Ni□ Fe□ Cr alloys, Mater. Sci. Eng. A, 148 (1991) 279-287.

[77] T. Gheno, F. Jomard, C. Desgranges, L. Martinelli, Grain boundary diffusion of chromium in polycrystalline nickel studied by SIMS, Materialia, 6 (2019) 100283.

[78] T.-F. Chen, G.P. Tiwari, Y. Iijima, K. Yamauchi, Volume and grain boundary diffusion of chromium in Ni-base Ni-Cr-Fe alloys, Mater. Trans., 44 (2003) 40-46.

[79] P. Nash, The Cr— Ni (Chromium-Nickel) system, Bulletin of Alloy Phase

Diagrams, 7 (1986) 466-476.

[80] J. Chen, D. Farkas, W. Reynolds Jr, Atomistic simulation of an fcc/bcc interface in Ni□ Cr alloys, Acta Mater, 45 (1997) 4415-4421.

[81] H. Nagai, M. Okabayashi, Deleterious Effect of Ti Addition on the Oxidation Resistance of Ni-20Cr Alloy, Trans. Jpn. Inst. Met., 22 (1981) 691-698.

[82] H. Nagai, M. Okabayashi, T. Murakami, High Temperature Oxidation of Ni-20Cr-xTiO2 Alloys, Trans. Jpn. Inst. Met., 23 (1982) 473-479.

[83] T.-H. Kim, D.-H. Lee, D. Kim, C. Jang, J.-I. Yun, Analysis of oxidation behavior of Ni-base superalloys by laser-induced breakdown spectroscopy, J Anal At Spectrom, 27 (2012) 1525-1531.

[84] C. Angerman, Long-term oxidation of superalloys, Oxid. Met., 5 (1972) 149-167.

[85] J. Chen, P. Rogers, J. Little, Oxidation behavior of several chromia-forming commercial nickel-base superalloys, Oxid. Met., 47 (1997) 381-410.

[86] S. Cruchley, H. Evans, M. Taylor, M. Hardy, S. Stekovic, Chromia layer growth on a Ni-based superalloy: sub-parabolic kinetics and the role of titanium, Corros Sci, 75 (2013) 58-66.

[87] A.N. Blacklocks, A. Atkinson, R.J. Packer, S.L.P. Savin, A.V. Chadwick, An XAS study of the defect structure of Ti-doped α-Cr2O3, Solid State Ion., 177 (2006) 2939-2944.

[88] J. Schindelin, I. Arganda-Carreras, E. Frise, V. Kaynig, M. Longair, T. Pietzsch, S. Preibisch, C. Rueden, S. Saalfeld, B. Schmid, Fiji: an open-source platform for biological-image analysis, Nature methods, 9 (2012) 676.

[89] I. Arganda-Carreras, V. Kaynig, C. Rueden, K.W. Eliceiri, J. Schindelin, A. Cardona, H. Sebastian Seung, Trainable Weka Segmentation: a machine learning tool for microscopy pixel classification, Bioinformatics, 33 (2017) 2424-2426.

[90] J.P. Abellán, W. Quadakkers, Development of ferritic steels for application as interconnect materials for intermediate temperature solid oxide fuel cells (SOFCs), Forschungszentrum Jülich in der Helmholz-Gemeinschaft, Zentralbibliothek, 2005.

[91] S.R. Phadke, J.C. Nino, Conductivity enhancement in lanthanum phosphates, J Am Ceram Soc, 94 (2011) 1817-1823.

[92] N. Shaigan, D.G. Ivey, W. Chen, Oxidation and electrical behavior of nickel/lanthanum chromite-coated stainless steel interconnects, Journal of power sources, 183 (2008) 651-659.

[93] W.Z. Zhu, S. Deevi, Opportunity of metallic interconnects for solid oxide fuel cells: a status on contact resistance, Materials Research Bulletin, 38 (2003) 957-972.

[94] S. Fontana, R. Amendola, S. Chevalier, P. Piccardo, G. Caboche, M. Viviani, R. Molins, M. Sennour, Metallic interconnects for SOFC: Characterisation of corrosion resistance and conductivity evaluation at operating temperature of differently coated alloys, Journal of Power Sources, 171 (2007) 652-662.

[95] P. Piccardo, P. Gannon, S. Chevalier, M. Viviani, A. Barbucci, G. Caboche, R. Amendola, S. Fontana, ASR evaluation of different kinds of coatings on a ferritic stainless steel as SOFC interconnects, Surface and Coatings

Technology, 202 (2007) 1221-1225.

[96] W.Z. Zhu, S.C. Deevi, Opportunity of metallic interconnects for solid oxide fuel cells: a status on contact resistance, Materials Research Bulletin, 38 (2003) 957-972.

[97] W.Z. Zhu, S. Deevi, Development of interconnect materials for solid oxide fuel cells, Materials Science and Engineering: A, 348 (2003) 227-243.

[98] G.V. Samsonov, The oxide handbook, Springer Science & Business Media, 2013.

[99] A. Petric, H. Ling, Electrical Conductivity and Thermal Expansion of Spinels at Elevated Temperatures, J Am Ceram Soc, 90 (2007) 1515-1520.

[100] X. Chen, P.Y. Hou, C.P. Jacobson, S.J. Visco, L.C. De Jonghe, Protective coating on stainless steel interconnect for SOFCs: oxidation kinetics and electrical properties, Solid State Ion., 176 (2005) 425-433.

[101] L.C. Weiner, Premo; and Wilhelm, H. A., "Temperature dependence of electrical resistivity of metals" (1952). Ames, L.I.T.R. 58., http://lib.dr.iastate.edu/ameslab_iscreports/58, Temperature dependence of electrical resistivity of metals.

[102] P. Kofstad, K. Lillerud, On high temperature oxidation of chromium II. Properties of and the oxidation mechanism of chromium, Journal of the electrochemical society, 127 (1980) 2410-2419.

[103] A. Holt, P. Kofstad, Electrical conductivity and defect structure of Cr2O3. II. Reduced temperatures ($<\sim$ 1000° C), Solid State Ion., 69 (1994) 137-143.

[104] A. Atkinson, M.R. Levy, S. Roche, R.A. Rudkin, Defect properties of Ti-doped Cr2O3, Solid State Ion., 177 (2006) 1767-1770.

[105] W. Hagel, Electrical Conductivity of Li-Substituted Cr2O3, Journal of Applied Physics, 36 (1965) 2586-2587.

[106] R. Huang, A.K. Agarwal, H.U. Anderson, Oxygen Activity Dependence of the Electrical Conductivity of Li-Doped Cr2O3, Journal of the American Ceramic Society, 67 (1984) 146-150.

[107] J.S. Park, H.G. Kim, Electrical Conductivity and Defect Models of MgO-Doped Cr2O3, Journal of the American Ceramic Society, 71 (1988) 173-176.

[108] D. Houivet, J. El Fallah, J.M. Haussonne, Phases in La2O3 and NiO doped (Zr,Sn)TiO4 microwave dielectric ceramics, Journal of the European Ceramic Society, 19 (1999) 1095-1099.

[109] Z. Lu, J. Zhu, E. Andrew Payzant, M.P. Paranthaman, Electrical Conductivity of the Manganese Chromite Spinel Solid Solution, Journal of the American Ceramic Society, 88 (2005) 1050-1053.

[110] H. Peng, A. Zakutayev, S. Lany, T.R. Paudel, M. d'Avezac, P.F. Ndione, J.D. Perkins, D.S. Ginley, A.R. Nagaraja, N.H. Perry, Li-Doped Cr2MnO4: A New p-Type Transparent Conducting Oxide by Computational Materials Design, Adv. Funct. Mater., 23 (2013) 5267-5276.

[111] A.R. Nagaraja, K.H. Stone, M.F. Toney, H. Peng, S. Lany, T.O. Mason, Experimental characterization of a theoretically designed candidate p-type transparent conducting oxide: Li-doped Cr2MnO4, Chem. Mater., 26 (2014) 4598-4604.

[112] D. Szymczewska, S. Molin, P. Hendriksen, P. Jasiński, Microstructure and electrical properties of Fe, Cu substituted (Co, Mn) 3O4 thin films,

Crystals, 7 (2017) 185.

[113] B. Talic, S. Molin, K. Wiik, P.V. Hendriksen, H.L. Lein, Comparison of iron and copper doped manganese cobalt spinel oxides as protective coatings for solid oxide fuel cell interconnects, Journal of Power Sources, 372 (2017) 145-156.

[114] X. Ledoux, S. Mathieu, M. Vilasi, Y. Wouters, P. Del-Gallo, M. Wagner, Oxide growth characterization during short-time oxidation of a commercially available chromia-forming alloy (HR-120) in air at 1,050° C, Oxid. Met., 80 (2013) 25-35.

[115] M. Kasrai, W. Lennard, R. Brunner, G. Bancroft, J. Bardwell, K. Tan, Sampling depth of total electron and fluorescence measurements in Si L-and K-edge absorption spectroscopy, Applied Surface Science, 99 (1996) 303-312.

[116] K.A. Unocic, Y. Chen, D. Shin, B.A. Pint, E.A. Marquis, STEM and APT characterization of scale formation on a La, Hf, Ti-doped NiCrAl model alloy, Micron, 109 (2018) 41-52.

[117] G.R. Holcomb, J. Tylczak, C. Carney, Oxidation of CoCrFeMnNi high entropy alloys, JOM, 67 (2015) 2326-2339.

[118] A.M. dit Clément, K. Hoummada, J. Drillet, V. Hébert, P. Maugis, Effects of cementite size and chemistry on the kinetics of austenite formation during heating of a high-formability steel, Computational Materials Science, 182 (2020) 109786.

[119] H.T. Michels, The effect of dispersed reactive metal oxides on the oxidation resistance of nickel-20 Wt pct chromium alloys, Metallurgical and Materials Transactions A, 7 (1976) 379-388.

[120] C. Giggins, B. Kear, F. Pettit, J. Tien, Factors affecting adhesion of oxide scales on alloys, Metallurgical Transactions, 5 (1974) 1685-1688.

[121] D. Whittle, J. Stringer, Improvements in high temperature oxidation resistance by additions of reactive elements or oxide dispersions, Philosophical Transactions of the Royal Society of London A: Mathematical, Physical and Engineering Sciences, 295 (1980) 309-329.

[122] H. Hindam, D. Whittle, Microstructure, adhesion and growth kinetics of protective scales on metals and alloys, Oxid. Met., 18 (1982) 245-284.

[123] P. Hou, J. Stringer, The effect of reactive element additions on the selective oxidation, growth and adhesion of chromia scales, Materials Science and Engineering: A, 202 (1995) 1-10.

[124] B.A. Pint, Optimization of reactive-element additions to improve oxidation performance of alumina-forming alloys, Journal of the American Ceramic Society, 86 (2003) 686-695.

[125] L. Latu-Romain, Y. Parsa, S. Mathieu, M. Vilasi, M. Ollivier, A. Galerie, Y. Wouters, Duplex n-and p-type chromia grown on pure chromium: a photoelectrochemical and microscopic study, Oxidation of Metals, 86 (2016) 497-509.

[126] X. Ledoux, S. Mathieu, M. Vilasi, Y. Wouters, P. Del-Gallo, M. Wagner, Oxide Growth Characterization During Short-Time Oxidation of a Commercially Available Chromia-Forming Alloy (HR-120) in Air at 1,050 °C, Oxid. Met., 80 (2013) 25-35.

[127] W.E. King, J.-H. Park, J. Routbort, K. Goretta, Effect of Y 2 O 3

additions on the plasticity of sintered Cr 2 O 3, Oxid. Met., 29 (1988) 217-223.

[128] A. Faes, J.-M. Fuerbringer, D. Mohamedi, A. Hessler-Wyser, G. Caboche, Design of experiment approach applied to reducing and oxidizing tolerance of anode supported solid oxide fuel cell. Part I: Microstructure optimization, Journal of Power Sources, 196 (2011) 7058-7069.

국문 초록

    최근 열기관에 사용되는 내열강은 발전 효율의 향상을 위해 보다 높은 온도의 환경에 놓이게 되었으며 이에 따라 내열강의 내산화성에 대한 연구가 주목받고 있다. 내열강의 내산화성이 충분하지 않을 경우 산화층의 박리로 인한 문제가 발생할 수 있으며 구조 재료로서 중요한 크리프 물성 등 기계적 물성 역시 저하될 수 있다, 또한 고체산화물연료전지(Solid Oxide Fuel Cell) 분야에서는 내열강의 표면에 형성되는 산화층에 의해 연료전지의 수명 및 발전 효율이 저하된다고 알려져 있다.

    앞서 언급한 문제들을 해결하기 위해서는 내열강의 고온 산화 거동에 대한 이해가 전제되어야 한다. 산화 현상을 단순히 풀이하면 금속과 산소의 반응일 뿐이지만, 내열강의 복잡한 조성 및 미세구조와 사용 환경에 따른 다양한 가스 조성은 내열강의 고온 산화 거동에 대한 이해를 어렵게 한다. 이로 인해 단순히 내열강의 결정립 크기만을 작게 변화시키더라도 내열강의 조성 및 산화 환경에 따라 내산화성은 개선될 수도 혹은 저하될 수도 있다. 따라서 어떠한 미세조직 효과가 내열강의 고온 산화 거동에 주된 영향을 미치는 인자인지를 결정하는 것은 매우 중요하다.

    본 연구에서는 합금 입계에 의한 영향과 합금/산화층 계면의 영향을 각각의 챕터에서 다루었다. 첫번째 챕터에서는 미세조직이 제어된 니켈기 초합금에서 합금의 입계에 의한 고온 산화 거동의 변화를 관찰하였다. 순산소 발전 방식을 모사한 760도, O_2 + 100ppm SO_2 조건에서 100시간 동안 산화 실험을 진행한 결과 결정립 크기가 가장 작은 시편이 다른 시편들보다 우수한 내산화성을 보이는 것을 확인하였다. 결정립 크기가 작은 시편의 경우 높은 입계 분율로 인해 충분한 크롬이 합금의 입계를 따라 금속/산화층 계면으로 공급되었고 안정적인 Cr_2O_3 산화층이 성장하는 것을 관찰하였다. 충분한 크롬이 계면에 공급되지 못한 다른 시편들의 경우 합금의 표면 크롬 조성이 감소했고 크롬 공핍 영역의 형성이 결정립 크기가 작은 시편에 비해 명확하게 관찰되었다. 이로 인해 크롬의 선택적 산화뿐만 아니라 타이타늄이 산화층으로 확산되었고 타이타늄으로 인한 내열강의 내산화성 저하됨을 확인하였다. 따라서 본 연구에서는 니켈기 초합금이 순산소 조건에서도 우수한 내산화성을 확보하기 위해서는 합금의 입계를 통한 빠른 크롬 공급이 중요한 요인인 것을 입증하였다.

두번째 챕터에서는 고체산화물 연료전지의 분리판을 목표로 설계된 내열강에 란타늄을 첨가하여 란타늄의 조성에 따른 고온 산화 거동의 변화를 관찰하였다. 800도에서 합금의 내산화성을 평가하였으며 분리판 면저항 측정을 통해 합금 표면에 형성된 산화층의 전기적 물성을 평가하였다. 란타늄이 첨가될 경우 산화층의 성장이 가속화되어 산화층의 평균 두께는 증가하였다. 하지만 란타늄과 니켈 동시 첨가 시 기존에 관찰되었던 평평한 합금/산화층 계면과 달리 매우 불균일한 계면이 형성되었으며 입계를 통한 액상 란타늄의 확산이 그 원인으로 추정된다. 계면 변화로 인해 란타늄 첨가 합금의 금속/산화층 계면의 접합력은 개선된 것으로 보이며 산화층 내 공공 형성 또한 억제되었다. 따라서 본 연구에서 연구된 란타늄 첨가 합금은 비교적 두꺼운 산화층을 갖음에도 란타늄이 첨가되지 않은 합금에 비해 전기적 물성이 개선되었다.

주요어: 고온 산화, 전기적 물성, 합금 입계 효과, 합금/산화층 계면 효과, 니켈기 초합금, 페라이트계 스테인리스강